National Renewable Energy Laboratory
Innovation for Our Energy Future
A national laboratory of the U.S. Department of Energy
Office of Energy Efficiency & Renewable Energy

Innovative Characterization of Amorphous and Thin-Film Silicon for Improved Module Performance

28 April 2005 – 15 September 2008

J.D. Cohen
University of Oregon
Eugene, Oregon

Subcontract Report
NREL/SR-520-47195
December 2009

NREL is operated for DOE by the Alliance for Sustainable Energy, LLC
Contract No. DE-AC36-08-GO28308

Innovative Characterization of Amorphous and Thin-Film Silicon for Improved Module Performance

28 April 2005 – 15 September 2008

J.D. Cohen
University of Oregon
Eugene, Oregon

NREL Technical Monitor: Bolko von Roedern
Prepared under Subcontract No. ZXL-5-44205-11

Subcontract Report
NREL/SR-520-47195
December 2009

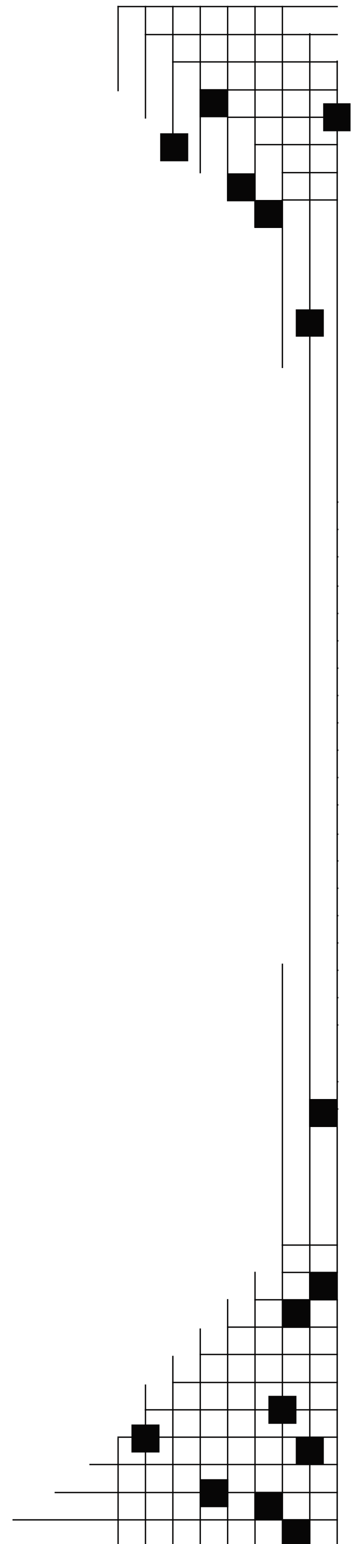

National Renewable Energy Laboratory
1617 Cole Boulevard, Golden, Colorado 80401-3393
303-275-3000 • www.nrel.gov

NREL is a national laboratory of the U.S. Department of Energy
Office of Energy Efficiency and Renewable Energy
Operated by the Alliance for Sustainable Energy, LLC

Contract No. DE-AC36-08-GO28308

This publication was reproduced from the best available copy submitted by the subcontractor and received no editorial review at NREL

NOTICE

This report was prepared as an account of work sponsored by an agency of the United States government. Neither the United States government nor any agency thereof, nor any of their employees, makes any warranty, express or implied, or assumes any legal liability or responsibility for the accuracy, completeness, or usefulness of any information, apparatus, product, or process disclosed, or represents that its use would not infringe privately owned rights. Reference herein to any specific commercial product, process, or service by trade name, trademark, manufacturer, or otherwise does not necessarily constitute or imply its endorsement, recommendation, or favoring by the United States government or any agency thereof. The views and opinions of authors expressed herein do not necessarily state or reflect those of the United States government or any agency thereof.

Available electronically at http://www.osti.gov/bridge

Available for a processing fee to U.S. Department of Energy and its contractors, in paper, from:

U.S. Department of Energy
Office of Scientific and Technical Information
P.O. Box 62
Oak Ridge, TN 37831-0062
phone: 865.576.8401
fax: 865.576.5728
email: mailto:reports@adonis.osti.gov

Available for sale to the public, in paper, from:

U.S. Department of Commerce
National Technical Information Service
5285 Port Royal Road
Springfield, VA 22161
phone: 800.553.6847
fax: 703.605.6900
email: orders@ntis.fedworld.gov
online ordering: http://www.ntis.gov/ordering.htm

Printed on paper containing at least 50% wastepaper, including 20% postconsumer waste

PREFACE

This Annual Technical Progress Report covers the work performed at the University of Oregon for the period 28 April 2005 – 15 September 2008 under NREL Subcontract Number ZXL-5-44205-11. The following personnel participated in this research program:

NAME	TITLE	WORK PERFORMED
J. David Cohen	Principal Investigator	Program Manager
Shouvik Datta	Research Associate	Properties of NREL HWCVD a-Si,Ge:H alloys
JinWoo Lee (part time)	Research Associate	Studies of $Cu(InGa)Se_2$ photovoltaic devices.
Peter Hugger	Research Assistant	Properties of United Solar nc-Si:H materials
Pete Erslev (part time)	Research Assistant	Studies of $Cu(InGa)Se_2$ photovoltaic devices.

TABLE OF CONTENTS

Page

LIST OF ILLUSTRATIONS v

LIST OF TABLES viii

EXECUTIVE SUMMARY ix

1.0 INTRODUCTION 1

2.0 SAMPLES

2.1 UNITED SOLAR NANOCRYSTALLINE SILICON 2
2.2 NREL HOT-WIRE CVD AMORPHOUS SILICON-GERMANIUM ALLOYS 6
2.3 Cu(InGa)Se_2 (CIGS) PHOTOVOLTAIC DEVICES 8

3.0 EXPERIMENTAL CHARACTERIZATION METHODS

3.1 ADMITTANCE SPECTROSCOPY 13
3.2 DRIVE-LEVEL CAPACITANCE PROFILING 13
3.3 TRANSIENT PHOTOCAPACITANCE AND PHOTOCURRENT 14

4.0 PROPERTIES OF UNITED SOLAR NANOCRYSTALLINE SILICON

4.1 DRIVE-LEVEL CAPACITANCE PROFILES *vs.* HYDROGEN PROFILES 16
4.2 SUB-BAND-GAP PHOTOCAPACITANCE AND PHOTOCURRENT SPECTROSCOPY 19
4.3 LIGHT-INDUCED DEGRADATION IN NANOCRYSTALLINE SILICON 23

5.0 NREL HOT-WIRE AMORPHOUS SILICON-GERMANIUM ALLOYS

5.1 REVIEW OF PREVIOUS WORK 25
5.2 AN OXYGEN RELATED DEFECT IN HWCVD a-Si,Ge:H 27
5.3 DETAILED DYNAMICAL PROPERTIES OF THE OXYGEN RELATED TRANSITION 32

6.0 COPPER INDIUM-GALLIUM DISELENIDE SOLAR CELLS

6.1 BACKGROUND 37
6.2 RESULTS ON NREL CIGS CELLS FROM ADMITTANCE 39
6.3 RESULTS ON NREL CIGS CELLS FROM CAPACITANCE PROFILING 40
6.4 STUDY OF NREL CIGS CELLS WITH VARYING COMPOSITIONAL PROFILING 43
6.5 THE ROLE OF SODIUM IN CIGS SOLAR CELLS 47

7.0 SUMMARY AND CONCLUSIONS 56

8.0 SUBCONTRACT SUPPORTED PUBLICATIONS 61

9.0 REFERENCES 62

LIST OF ILLUSTRATIONS

Page

FIG. 1 Layout of USOC nc-Si:H devices on substrate indicating the variation of the amorphous/crystallinity fractions with position 3

FIG. 2 Raman spectra obtained at 785nm for two nc-Si:H devices from the same deposition but at different positions on the substrate 4

FIG. 3 Open-circuit voltage in nc-Si:H *vs.* crystalline fraction... 5

FIG. 4. Oxygen content for one series of the NREL HWCVD a-Si,Ge:H films and their relative fractions of Ge with respect to Si as measured by SIMS............................ 8

FIG. 5. Open circuit voltage *vs.* short circuit current for the eight NREL CIGS devices..... 9

FIG. 6. Relationship of V_{OC}-J_{SC} products and Fill Factors to overall CIGS device efficiencies.. 9

FIG. 7 SIMS determined spatial profiles of the Ga-to-In ratios for representative NREL CIGS sample devices from each of the three depositions 10

FIG. 8 Grading profiles for the three CIGS sample devices with non-uniform Ga/(Ga+In) spatial profiles as determined from SIMS.. 11

FIG. 9 SIMS depth profiles of a matched pair of higher and lower sodium $Cu(InGa)Se_2$ sample devices.. 12

FIG. 10. Schematic of four different types of sub-bandgap optical transitions 15

FIG. 11. Raman spectra and drive-level profiles for the least and most crystalline nc-Si:H samples from deposition 15125 before and after light-soaking............................... 17

FIG. 12. Raman spectrum and State B drive-level profiles for deposition 15125 in a region with a crystalline fraction that is intermediate between those displayed in Fig. 6 ... 18

FIG. 13. TPI spectra for nc-Si:H samples deposited on specular and textured substrates...... 19

FIG. 14. Transient photocapacitance and transient photocurrent spectra for a device with X_c=0.72 and a device with X_c=0.53 at different temperatures................................. 20

FIG. 15. Variation of TPC signal with temperature at an optical energy of 1.5eV................. 21

FIG. 16. Open circuit voltage and cell efficiency *vs.* minority carrier collection for four nc-Si:H devices deposited on Ag/ZnO textured substrates............................. 21

FIG. 17. Photocapacitance spectra for nc-Si:H sample device 2B10514 in its light degraded state 22

FIG. 18. Comparison of the 295K TPC spectra for nc-Si:H sample 13993 before and after light-soaking 24

FIG. 19. Schematic of a possible model to explain light-induced changes observed in the drive-level profiles and the photocapacitance spectra of nc-Si:H 24

FIG. 20. Comparison of TPC spectra on two 29at.% Ge films with the later film exhibiting poorer electronic properties 25

FIG. 21. Comparison of TPC spectra on two 47at.% Ge films with the later film exhibiting poorer electronic properties 25

FIG. 22 Spatial profiles of HWCVD a-$Si_{0.70}Ge_{0.30}$:H deep defect densities with different oxygen levels in an annealed and light-soaked state 26

FIG. 23. TPC spectra for HWCVD a-$Si_{0.70}Ge_{0.30}$:H films with different oxygen levels deposited onto stainless steel substrates and onto p^+ c-Si substrates 27

FIG. 24. TPC and TPI spectra before and after light-soaking for the a-$Si_{0.70}Ge_{0.30}$:H film deposited without any intentional air leak 28

FIG. 25. TPC and TPI spectra before and after light-soaking for the a-$Si_{0.70}Ge_{0.30}$:H film deposited with an intentional 0.06sccm air leak 28

FIG. 26. Photocapacitance spectra for three a-$Si_{0.7}Ge_{0.3}$:H samples with different oxygen levels 30

FIG. 27. TPC spectra of the highest oxygen a-$Si_{0.7}Ge_{0.3}$:H sample at 3 temperatures 30

FIG. 28. Photocapacitance (TPC) spectra for a 15at.% Ge sample using an intentional 0.2sccm air-leak 31

FIG. 29. Detailed temperature dependence of the photocapacitance signals near 1.2eV for the highest oxygen contaminated a-Si,Ge:H samples with 15at.% and 30at.% Ge .. 31

FIG. 30. Photocapacitance signal *vs.* energy at 370K for the 30at.% Ge sample with the 0.2sccm oxygen contamination level at different light intensities 32

FIG. 31 Capacitance difference signal *vs.* time during and after excitation using a 1.2eV light pulse at different intensities 33

FIG. 32. Transients for the 30at.% Ge sample following a 1s duration 1.2eV light pulse for six different temperatures 33

FIG. 33. The early part of the temperature dependence of capacitance recovery following the 1.2eV light exposure for the a-$Si_{0.7}Ge_{0.3}$:H alloy 34

FIG. 34. The second part of the transient recovery following the 1.2eV optical excitation at 370K on a semi log plot ... 35

FIG. 35. Capacitance recovery transients for different values of applied bias at 370K following the 1 second 1.2eV light pulse ... 36

FIG. 36. Dark capacitance recovery after light exposure for 1 second for both the 15at.% and 30at.% Ge highest oxygen samples ... 36

FIG. 37 Capacitance *vs.* temperature at 6 measurement frequencies for an IEC CIGS device at zero bias. ... 37

FIG. 38 Drive-level capacitance profiles taken for one IEC CIGS device near 165K at 5 measurement frequencies ... 38

FIG. 39 Capacitance *vs.* frequency at zero bias for one device from each of the three NREL sample depositions ... 39

FIG. 40 Drive-level capacitance profiles (DLCP) and CV profiles for representative NREL devices over a broad range of temperatures ... 41

FIG. 41 Correlation of NREL device efficiencies with the DLCP determined densities ... 42

FIG. 42 Transient photocurrent and transient photocapacitance spectra obtained for the CIGS sample device with uniform compositional grading ... 44

FIG. 43 Transient photocurrent and transient photocapacitance spectra obtained for the CIGS sample device with a gallium fraction increasing away from the junction ... 45

FIG. 44 TPI and TPC spectra for the sample device with a “V-shaped” Ga grading profile ... 45

FIG. 45 Drive-level capacitance profiles for CIGS sample devices with three different types of Ga compositional profiling ... 47

FIG. 46 DLC Profiles for normal Na containing CIGS cells, a reduced Na sample, and a Na free cell resulting from deposition onto a Ti foil substrate ... 48

FIG. 47 TPC Spectra of the two CIGS samples from IEC deposition A with normal and reduced Na. ... 49

FIG. 48 Admittance spectra under 0 volt applied bias for the Na containing samples, and the reduced Na samples ... 50

FIG. 49 Admittance spectra for various temperatures under 0.3 volt forward bias for the CIGS sample from deposition A with normal Na and reduced Na levels ... 51

FIG. 50 Admittance spectra at 220K for various values of applied voltage for the normal Na level and the reduced Na sample ... 51

FIG. 51 Simulated fits to the DLCP and CV profiles taken at 310K for the Na free sample from deposition B along with the defect distributions used to simulate the data 49

FIG. 52 Comparison of admittance spectra for Na free sample (deposition B) before and after light soaking... 54

FIG. 53 During light soaking the Na-free sample exhibited a much larger increase in deep acceptors compared to the increase in the free carrier density than the sample containing sodium 55

FIG. 54 For the sample with Na, the activation energy of the deep acceptor varies with light soaking in a manner that is consistent with the Meyer-Neldel rule................. 56

FIG. 55 For the companion samples with or without Na, the metastable deep acceptor densities annealed at the exactly the same rate states for each pair of samples........ 56

LIST OF TABLES

TABLE I. May 2005 United Solar nc-Si:H sample device series.. 2

TABLE II. January 2006 United Solar nc-Si:H sample series 3

TABLE III. January 2007 set of USOC nc-Si:H samples to investigate detailed effects of hydrogen profiling methods on devices with different degrees of crystallinity... 3

TABLE IV. Summary of Raman spectral analysis for 2007 United Solar nc-Si:H samples... 5

TABLE V. Growth parameters for two pairs of intrinsic a-Si,Ge:H layers deposited by HWCVD containing lower and higher levels of oxygen 7

TABLE VI. Full set of HWCVD a-Si,Ge:H samples obtained from NREL in early 2006 to examine effects of intentional oxygen contamination... 7

TABLE VII. NREL CIGS devices from 3 depositions chosen for detailed characterization using our experimental methods 8

TABLE VIII. Cell performance parameters for devices fabricated at NREL with different Ga/(Ga+In) grading profiles 10

TABLE IX. Device performance parameters of the matched $Cu(InGa)Se_2$ devices simultaneously deposited on substrates to yield different Na levels 11

EXECUTIVE SUMMARY

Our work under NREL Subcontract ZXL-5-44205-11 has focused on three areas of study. In the first area, the study of nc-Si:H materials, we focused on a set of actual working n-i-p solar cell devices which were deposited on specular stainless-steel under four different types of hydrogen profiling and with widely varying crystalline fractions. Our results suggest that the degree of crystallinity in these nc-Si:H samples, rather than the hydrogen profiling function itself, was the strongest factor determining the defect response in our junction capacitance measurements. Surprisingly, from our DLCP measurements, the samples with estimated crystalline fractions above 60vol.% exhibited a much greater increase of deep defects after light soaking compared to samples with higher amorphous fractions. The minority carrier collection fraction determined by a comparison of the transient photocapacitance and photocurrent (TPC and TPI) appeared to be reasonably well correlated to the device performance. All of the sample devices exhibited a decrease in performance after light soaking with 610nm filtered ELH light. Our TPC and TPI analysis indicated a large decrease in the minority carrier collection after prolonged light exposure. To account for this we put forward a model that hypothesizes a light-induced increase in an energetic barrier between the crystalline and amorphous components.

The second area of study involves sets of HWCVD a-Si,Ge:H alloys deposited at NREL by Yueqin Xu. We initially determined that such samples exhibited some of the narrowest bandtails (as low as 43meV) for a-Si,Ge:H alloys deposited at 2 to 3Å/s rates. Due to indications that higher oxygen levels in these materials significantly decreased their electronic quality, we examined a series of samples in which controlled levels of oxygen impurities were introduced, ranging from below 10^{19}cm^{-3} to roughly 5×10^{20}cm^{-3}. We determined that the oxygen gave rise to a distinct deep defect, with an optical transition lying roughly 1.3 to 1.4 eV above the valence band, but only resulted in a very modest increase in Urbach energy. However, our TPC and TPI studies indicated a very high degree of hole collection for these samples which did not decrease after prolonged light-soaking.

The oxygen related defect transition was found to be easily observable at oxygen levels as low as 10^{20} cm^{-3}, and in samples with Ge fractions of both 15at.% and 30at.%. Because of the long electron trapping times we inferred that there must exist a large barrier to their subsequent thermal emission into the conduction band. This oxygen related center also exhibited very usual electron thermal emission behavior after the electrons were optically inserted into it from the valence band; namely, a two-step thermal emission process in which the first electron was released in a thermally activated manner, while the second was released in a temperature independent manner with a characteristic time constant of 2.2 seconds. This unusual behavior was only observed for higher intensity light tuned to the defect transition. It has not yet been satisfactorily explained.

In our third area of study, we applied our junction capacitance methods to study CIGS thin film solar cells. By extending our drive-level capacitance profiles slightly into forward bias we could examine the region of the absorber closer to the barrier junction. We first examined a set of NREL CIGS devices of varying efficiencies (14.4% to 17.2%) and, indeed, found a good correlation between the DLCP defect density in the region closer to the junction interface while observing virtually no correlation with the defect density farther into the absorber. Next, we examined NREL samples with four different types of profiling using DLCP, TPC and TPI

measurements. Comparing the TPC and TPI spectra in the photon energy regime above the bandgap for photon energies up to 2eV, we found that the compositionally profiled samples indicated an enhanced TPI/TPC ratio for photon energies near 1.2eV, thus implying an enhanced minority carrier collection in this regime. This supports the idea that the compositional grading does indeed increase the collection of electrons generated at longer wavelengths in the absorber region beyond the edge of the depletion region.

We also carried out measurements to address the beneficial role of sodium incorporation in CIGS devices which, in the 2 pairs of matched IEC samples with normal and reduced levels of Na, led to a reduction of V_{OC} by 130mV in the latter case. Our measurements revealed that, in contrast to the samples with normal levels of sodium, the sample devices with reduced or no Na exhibited a substantially lower free carrier density and the lack of the deep acceptor feature. The sub-band-gap TPC spectra showed a broader defect band and a steeper Urbach energy with the addition of Na which implied an increase in the carrier mobilities. Under forward bias our admittance measurements revealed the existence of a large defect density at the CdS/CIGS heterojunction for the lower Na samples. Through detailed numerical modeling, we then demonstrated that the difference in DLCP *vs.* CV profiles could be reproduced by introducing a large density of defects near the barrier junction (roughly 10^{17} cm^{-3}) lying close to mid-gap, and exponentially decreasing with distance away from the junction. Such a distribution of deep defects near the barrier interface readily explains the loss in V_{OC} in the sample with reduced Na. Thus, it appears that it is the passivation of these interfacial defects that primarily accounts for the beneficial effects of Na with respect to the higher values of V_{OC}.

We also examined the effects of Na on CIGS by comparing the metastable properties on the matched sets of samples following light exposure. These observations were made: (1) Following light exposure the samples without sodium developed a significant deep acceptor density throughout the bulk region of the absorber that had been absent in the fully annealed samples; (2) Whereas the standard Na-level CIGS samples exhibited a nearly 1-to-1 metastable increase in both the free carrier density and deep acceptor density with increasing light exposure, the samples without Na showed a substantial increase in deep acceptors with a much smaller relative increase in free carriers; and (3) The activation energy revealed by admittance for the deep acceptors varied with light soaking (from 275meV to roughly 60meV) for the standard sample with variations in the thermal emission prefactor obeying a Meyer-Neldel rule while, for the Na-free samples, this activation energy and prefactor remained nearly constant (close to 350meV and 10^{12} s^{-1}). While the last observation might indicate that the deep acceptor response in the two types of samples are fundamentally different, the annealing behavior with increasing temperature appears identical indicating that the deep acceptor in the two types of samples has the same origin. Since the 1-to-1 increase in deep acceptor and free carrier density has been taken as strong evidence for a model of metastable behavior in CIGS materials involving the (V_{Se}-V_{Cu}) complex as proposed by Lany and Zunger, the lack of such a 1-to-1 correspondence in the samples without Na may have important consequences. That is, for samples without Na, it appears that light soaking simply results in an energy shift of the defect in the gap without any change in its electronic occupation (in the neutral bulk region).

1.0 INTRODUCTION

The work carried out under NREL Subcontract ZXL-5-44205-11 has focused primarily on three subject areas. First, we worked to evaluate the nanocrystalline Si material under development at United Solar Ovonics Corporation (USOC) which will be denoted in this report as nc-Si:H. It is hoped that such materials may ultimately be able to replace one of a-Si,Ge:H layers in an amorphous silicon triple junction device. Our most productive activity came from evaluating an extensive series of United Solar sample devices deposited on specular stainless substrates using four types of hydrogen profiling and, by virtue of a spatially varying rf field intensity across the substrate, different crystalline fractions. Almost all of the nc-Si:H samples studied were finished n-i-p devices. Of particular interest were the observed differences in the light induced deep defect creation behavior depending on the sample crystalline fractions.

Our second major focus has been in the evaluation of amorphous silicon-germanium alloys produced by the hot-wire CVD growth process by Yueqin Xu at NREL. After characterizing the basic electronic properties of these materials, we focused on studying the effects of oxygen at varying levels introduced intentionally using a controlled air leak-valve. This led to the discovery of optical transition at a energy near 1.3eV between the valence band and an empty oxygen related defect level in the mobility gap. Through a study of temperature dependence of this feature we have concluded that there must exist a large barrier to the subsequent thermal emission of the electron into the conduction band. We hypothesize that the observed oxygen impurity related defect state may be associated with a positively charged oxygen donor level, possibly the previously suggested three fold coordinated oxygen center (O_3^+).

Finally, we characterized the electronic properties of several series of copper indium-gallium diselenide (CIGS) materials. These CIGS related studies have accounted for roughly 30% of our work under our Thin-Film Partnership Subcontract. The goal of this work was to try to identify some reasons for the vastly different performance levels of laboratory based devices compared to CIGS devices produced by growth processes more suitable to large scale manufacturing. Our studies in this regard have been threefold: (1) Identifying differences in the electronic properties that can be correlated to cell efficiency; (2) Exploring how Ga grading techniques leads to increases in cell efficiency; and (3) Attempt to identify the beneficial effects of Na impurities on CIGS photovoltaic devices. Sample devices for studies in the first two areas were produced by Miguel Contreras at NREL; the samples for the last area of study were obtained through a collaboration with Bill Shafarman at IEC.

Following a detailed description of the sample devices utilized, and a brief discussion of our experimental methods, our results for each of these three subject areas will be presented. Following this we will provide a summary of our results, and some general conclusions.

2.0 SAMPLES

2.1 UNITED SOLAR NANOCRYSTALLINE SILICON

Three sets of nc-Si:H sample devices were obtained from United Solar (B. Yan) during the first two years of our Subcontract period. The first was a series of six nc-Si:H devices which we received in May 2005, shortly after the beginning of our new Subcontract. Three of these were deposited by MVHF at a rate of 6Å/s, and the other 3 were deposited by the RF process at a somewhat lower rate. The MVHF samples were all n-i-p devices deposited onto SS coated with a textured Ag/ZnO back reflector and were finished with $0.05cm^2$ ITO top contacts. Two of these devices exhibited relatively high levels of degradation (about 15%) while the third exhibited very little degradation. The three RF nc-Si:H samples were fabricated in three different device structures: One was a n-i-p device with a Ag/ZnO textured back reflector, one was a n-i-p device on bare stainless steel, and one was a sandwich device: SS/a-Si:H/nc-Si:H/a-Si:H, in which the a-Si:H capping layers were 0.21μm thick. For all 6 devices the nc-Si:H layer was just under 1μm thick. The characteristics of these samples are summarized in Table I. The goal for this series of samples was to find out whether we could distinguish different electronic properties for the high degradation and low degradation films, and whether we could obtain consistent results on the RF samples independent of their different device structures.

A second series of five nc-Si:H samples was received from United Solar in January 2006. All of these were n-i-p devices. Two of these were deposited on specular stainless steel (SS) substrates, and three employed textured Ag/ZnO substrates. All the nc-Si:H intrinsic layers for this sample series were deposited using a modified VHF glow discharge process with a thickness roughly 1.5 μm. For all samples, ITO dots with an area of 0.05 cm^2 or 0.25 cm^2 were deposited

Table I. May 2005 United Solar nc-Si:H sample device series. The crystalline volume fractions, X_C, were estimated from Raman spectra, as described below.

Sample Number	Substrate	Structure	Crystalline Vol. Fraction X_C (%)	Comment
2B 10505	SS/Ag/ZnO	n-i-p, all nc-Si:H	41	Low Degradation
2B 10514	SS/Ag/ZnO	n-i-p, all nc-Si:H	61	High Degradation
2B 10521	SS/Ag/ZnO	n-i-p, all nc-Si:H	73	High Degradation
RF 13512	SS/Ag/ZnO	n-i-p, all nc-Si:H	68	Low Degradation
RF 13510	Specular SS	n-i-p, all nc-Si:H	33	Same as 13512
RF 13511	Specular SS	a-Si:H/nc-Si:H/a-Si:H	44	Same as 13512

Table II. January 2006 United Solar nc-Si:H sample series. All were n-i-p devices with roughly 1.5μm thick I-layers. The cell performance parameters are listed.

Sample No	Substrate	J_{SC} (mA/cm^2)	V_{OC} (volts)	FF	Eff (%)	Cryst. Vol. Fractions (%)	H_2 Dilution
14027	Ag/ZnO	26.5	0.469	0.581	7.22	63	Profiling
14036	SS	17.38	0.448	0.568	4.42	72	Profiling
14037	Ag/ZnO	25.99	0.429	0.512	5.71	68	Constant
14038	SS	17.36	0.451	0.531	4.16	80	Constant
13993	Ag/ZnO	24.39	0.548	0.641	8.57	53	Profiling

on the p layer as top contacts. In addition, three of the samples were grown using a H_2 dilution profiling process to control crystalline size and volume fraction distribution. The other two samples were grown using a constant H_2 dilution process for comparison. The structures that were deposited on textured substrates were nearly identical to actual end-product devices and so constituted material tested in its optimized geometry. Indeed, as can be seen from the cell performance parameters are listed in Table II, this sample set included one sample with an efficiency that exceeded 8.5%.

An extensive third set of nc-Si:H sample devices was received early in 2007. These were produced from 4 separate depositions with different types of hydrogen concentration variations

Table III. January 2007 set of USOC nc-Si:H samples to investigate detailed effects of hydrogen profiling methods on devices with different degrees of crystallinity.

Run	Profiling	Cell	Pmax	J_{SC}	V_{OC}	Fill Factr
15125	constant	94	3.51	11.86	0.597	0.496
15125	constant	75	4.31	15.57	0.53	0.522
15125	constant	74	3.95	14.89	0.501	0.529
15123	t^1/2	94	4.77	15.67	0.609	0.499
15123	t^1/2	75	4.94	16.12	0.534	0.575
15123	t^1/2	74	4.99	16.62	0.51	0.589
15117	linear	94	4.38	14.46	0.747	0.406
15117	linear	75	4.95	16	0.54	0.572
15117	linear	74	4.96	16.53	0.509	0.59
15121	t^2	94	3.96	11.57	0.859	0.399
15121	t^2	75	3.69	15.38	0.541	0.444
15121	t^2	74	4.06	15.68	0.496	0.521

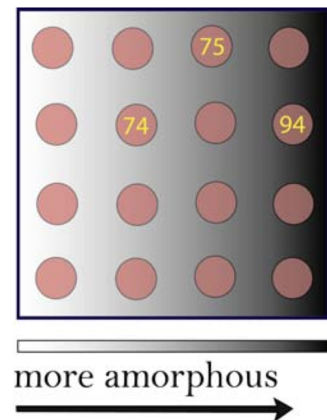

FIG. 1. Layout of USOC nc-Si:H devices on substrate indicating the variation of the amorphous/crystallinity fractions with position.

in each deposition; specifically, constant in time, square root in time, linear in time, and quadratic in time. Each substrate was processed to yield more than 30 devices, and the properties of these were different because the plasma varied over the diameter of the substrate. This meant that the devices near the center of the substrate were more crystalline, while those near the edge were more amorphous. Table III lists the sample devices we received for study and their performance parameters. In each deposition "Cell 74" was close to the center and thus had the highest crystalline fraction, "Cell 94" had the highest amorphous fraction, and "Cell 75" was an intermediate case. This is also indicated in the schematic of the cell positions shown in Fig. 1.

We employed Raman spectroscopy at 785nm to quantify the crystalline and amorphous fractions for this set of samples. An example for the 15125 (constant H dilution) sample set is shown in Fig. 2. Here we compare the Raman spectra for the most crystalline (74) and most amorphous (94) sample device. Each of these spectra has been analyzed by separation into 2 Gaussian components centered at 480 cm^{-1} (I_A) and 510 cm^{-1} (I_{GB}), and one Gaussian/Lorentzian mixed component at 520 cm^{-1} (I_C) as indicated by the green curves in Fig. 2. For our crystalline volume fraction (X_C) estimates we used the expression: $X_C = (I_C+I_{GB})/(I_C+I_{GB}+\xi\ I_A)$ taking $\xi = 1$.

Based upon such analyses of the Raman spectra we have estimated the crystalline fraction for each of the nc-Si:H samples studied. The details of this analysis for the samples in Table III are tabulated in Table IV. The estimates of X_C for the samples listed in Tables I and II were carried out in the same manner.

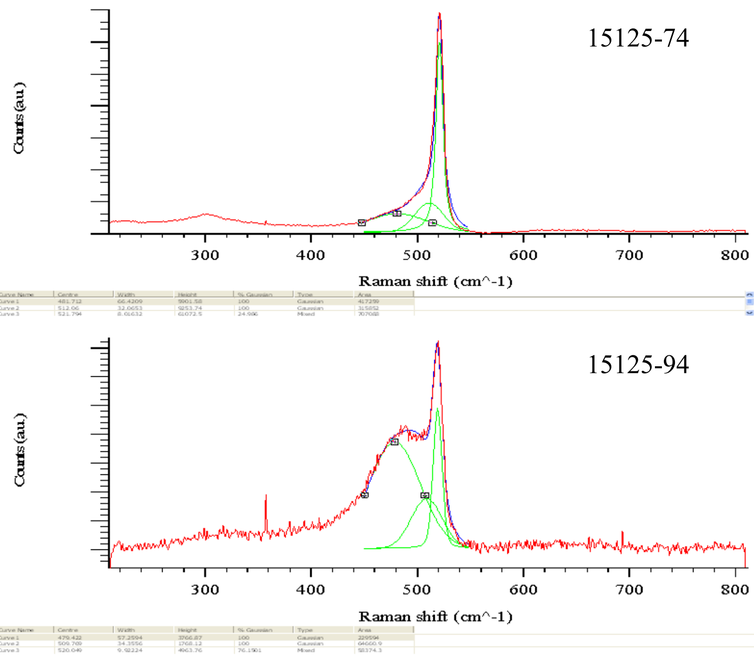

FIG. 2. Raman spectra obtained at 785nm for two nc-Si:H devices from the same deposition but at different positions on the substrate. The top spectrum was taken for a device near the middle of the substrate, and it contains a much higher crystalline fraction, than that of a device near the edge of the substrate, shown at the bottom. The thin green lines indicate a decomposition of each of these spectra into 3 components to enable an estimate of the crystalline fractions to be made. These estimates are listed in Table IV.

Table IV. Summary of Raman spectral analysis for United Solar nc-Si:H samples. These spectra have been separated into 3 components centered at 480, 510, and 520 cm^{-1} as illustrated in Fig. 2 which allows the crystallite fractions to be estimated [1,2].

Run	Cell	Profiling	I(~480cm^{-1})	I(~510 cm^{-1})	I(~520 cm^{-1})	Xc
15125	94	constant	229594	64661	58374	0.36
15125	75	constant	831052	327430	826590	0.59
15125	74	constant	417259	315852	707088	0.72
15123	94	t^1/2	2.24E+06	271741	303997	0.21
15123	75	t^1/2	1.04E+06	355527	1.41E+06	0.64
15123	74	t^1/2	329199	157610	537355	0.69
15117	94	linear	3.09E+06	867597	1.55E+06	0.45
15117	75	linear	3.14E+06	1.54E+06	2.59E+06	0.58
15117	74	linear	2.66E+06	896825	2.51E+06	0.67
15121	94	t^2	894569	389640	805516	0.59
15121	75	t^2	348128	69828	268511	0.51
15121	74	t^2	91146	49666	146672	0.69

In Figure 3 we plot the open circuit voltage of this last series of nc-Si:H devices *vs.* the crystalline volume fractions we obtained from our Raman measurements. Except for a couple samples there appears to be a good correlation indicating that the samples with the lower crystalline volume fractions have higher voltages. The two samples that are the exceptions were both from the regions that were the most amorphous for those two depositions. Since the amorphous fraction undoubtedly also varies with thickness it may be that these two samples had much higher amorphous fractions in the p-i junction regions than indicated from the Raman measurements.

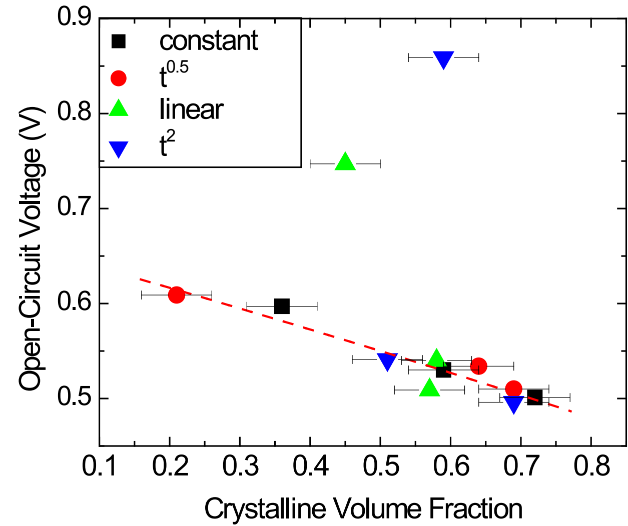

FIG 3. The open-circuit voltage in nc-Si:H generally increases with decreasing crystalline fraction. However, the most disordered cells grown under linear and t^2 H_2 dilution deviated significantly from this trend.

2.2 NREL HOT-WIRE CVD AMORPHOUS SILICON-GERMANIUM ALLOYS

For a couple years prior to this Subcontract period we had been examining the electronic properties of HWCVD a-Si,Ge:H alloys deposited at NREL using a lower filament temperature process. For a long time the hot-wire CVD method was generally unsuccessful for the a-Si,Ge:H alloys, resulting in materials with anomalously large deep defect densities and broad band tails.[3] However, by employing tantalum filaments held at somewhat lower temperature (1800°C), we had found that the electronic properties for these a-Si,Ge:H alloys were usually quite good. A subsequent series of films deposited in early 2005 appeared to have considerably poorer electronic properties and it had seemed plausible that the problem might be due to higher oxygen levels. We received a couple of these higher oxygen a-Si,Ge:H samples with Ge fractions of 29 and 47at.% and we were asked to compare their properties with the samples of the same Ge fractions (L1306 and L1307) that we had characterized previously. The growth characteristics of these samples (L1306, L1307, L1430, and L1431) are listed in Table V. All of the above samples were deposited onto specular stainless steel substrates, and a semi-transparent Pd contact was thermally evaporated on top of the intrinsic layer to provide a Schottky junction for our capacitance based measurements.

After the source of the contamination was finally discovered and eliminated in the Fall, 2005 it then seemed important to specifically investigate the effects of oxygen contamination on the electronic properties these HWCVD deposited a-Si,Ge:H films in more detail. In early 2006 an extensive series of a-Si,Ge:H alloy samples were deposited using a controlled leak valve to introduce a systematic variation in oxygen level during the HWCVD process. Sets of samples with roughly 30at.% Ge, 15at.% Ge, and no Ge were prepared by Yueqin Xu at NREL. Films were deposited both on specular stainless steel (SS) substrates again coated with thin layers n^+ PECVD a-Si:H and simultaneously on heavily doped p^+ crystalline Si substrates. Typically a 1:1 hydrogen dilution level [i.e., $H_2/(SiH_4 + GeH_4) = 1$] was maintained during the depositions. Growth rates typically varied between 1.5 to 2Å/s. The substrate temperatures were always set to 204°C at the beginning of film growth, but the final temperatures were higher (~280°C) due to filament heating. A semi-transparent Pd contact was again deposited on the top surface all samples to provide a top Schottky barrier for our junction-capacitance based measurements. However, in case of the samples deposited onto p^+ crystalline Si, we utilized the substrate barrier junction for our measurements. Detailed growth parameters for these HWCVD a-Si,Ge:H films are listed in Table VI. SIMS measurements were carried out and indeed revealed a systematic increase of oxygen contamination as the air leak was gradually increased to 0.2sccm. Figure 4 shows the relative content of oxygen in the samples and germanium fraction with respect to Si

Table V. Growth parameters for two pairs of intrinsic a-Si,Ge:H layers deposited by HWCVD containing lower levels of oxygen (L1306 and L1307) and higher levels of oxygen (L1430 and L1431). One additional sample (L1549) with a higher level of oxygen but deposited onto a crystalline Si substrate was also included for study.

Sample Number	Ge Fraction (at.%)	Substrate	i-layer Thickness (μm)	Gas Ratio $\frac{GeH_4}{(GeH_4+SiH_4)}$	Final Substrate Temperature	Growth Rate (Å/s)	E_{04} (eV)	E_{Tauc} (eV)
L1306	29	Stainless steel	1.60	12%	293°C	1.78	1.66	1.50
L1430	29	Stainless steel	1.73	12%	305°C	2.4	1.64	1.50
L1549	29	p^+ c-Si (100)	1.47	12%	295°C	1.63	1.65	1.50
L1307	47	Stainless Steel	1.44	25%	292°C	2.00	1.47	1.32
L1431	47	Stainless Steel	2.27	25%	305°C	3.15	1.46	1.32

Table VI. Full set of HWCVD a-Si,Ge:H samples obtained from NREL in early 2006 to examine effects of intentional oxygen contamination. All of these depositions were carried out simultaneously on specular stainless steel as well as heavily doped p^+ crystalline Si substrates.

n Samples' ID	Ts_starting °C	Ts_ending °C	Deposition Time(min)	Used Gases: SiH4	GeH4*	H2	air-leaking sccm
L1628	204	289	150	26.4	6.3	30	no
L1629	204	284	130	26.4	6.3	30	0.06
L1630	204	289	140	26.4	6.3	30	0.02
L1631	204	275	130	26.4	6.3	30	0.2

All above are a-SiGe:H alloys with Ge_% about ~29-32%

Samples' ID	Ts_starting °C	Ts_ending °C	Deposition Time(min)	SiH4	GeH4*	H2	air-leaking sccm
L1632	204	315	150	30		0	no
L1633	204	295	165	26.4		26.4	no
L1634	205	315	150	30		0	0.06

All above are a-Si:H films with no Ge

Samples' ID	Ts_starting °C	Ts_ending °C	Deposition Time(min)	SiH4	GeH4*	H2	air-leaking sccm
L1636	205	289	200	26.6	2.7	28	no
L1637	205	292	180	26.6	2.7	28	0.02
L1640	205	292	180	26.6	2.7	28	0.06
L1641	205	288	150	26.6	2.7	28	0.2

All above are a-SiGe:H alloys with Ge_% about ~15%

for the nominally 30at.% Ge alloy series. At the same time, these SIMS measurements indicated that the N content ($<4 \times 10^{16}$ cm^{-3}) remained nearly constant.

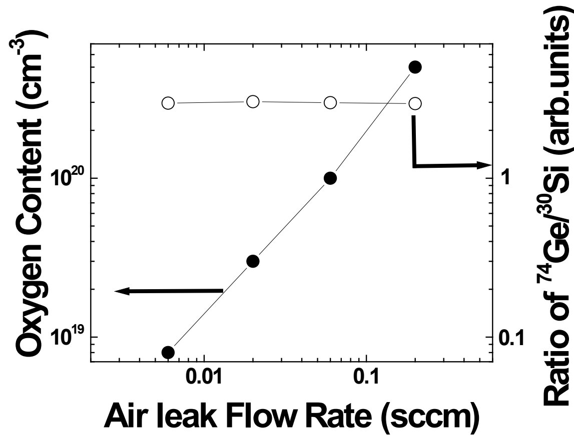

FIG. 4. Oxygen content for the above series of the NREL HWCVD a-Si,Ge:H films containing roughly 30at.% Ge. Note the systematic increase in the oxygen level in the film with increase air leak flow rate as well as the nearly constant fraction of Ge (roughly 30at.%) in this series of samples. Data corresponding to 'no intentional air leak' was plotted against an imaginary flow rate of 0.006 sccm. Also note that the relative fraction of Ge with respect to Si as measured by SIMS remained essentially constant..

2.3 Cu(InGa)Se_2 (CIGS) PHOTOVOLTAIC DEVICES

2.3.1 NREL CIGS HIGH EFFICIENCY SAMPLE DEVICES

For the current Subcontract under the Thin-Film Partnership program, our Statement of Work indicated that, while concentrating the majority of our effort to silicon-based thin-film devices, we would also devote roughly a third of our effort to the study of Cu(InGa)Se_2 (CIGS) thin-film photovoltaics. Our stated goal in our CIGS work is to apply our measurement techniques to try to understand differences between the best laboratory cells, and those fabricated using processes better suited for manufacturing. We began by examining laboratory CIGS devices produced by Miguel Contreras at NREL.

The first set of such samples we received in July 2005. Rather than characterizing only the best NREL CIGS devices, we thought it would be much more interesting to compare the results of our measurements on NREL devices with varying levels of performance. In that manner, we

Table VII. NREL CIGS devices from 3 depositions chosen for detailed characterization using our experimental methods. The area of each sample device was 0.406 cm^2.

Device Number	V_{OC} (volts)	J_{SC} (mA/cm^2)	Fill Factor (%)	Efficiency (%)
C1919-11 Cell 3	0.630	32.95	71.43	14.833
C1919-11 Cell 4	0.642	32.51	68.99	14.393
C1813-21 Cell 3	0.657	33.26	76.08	16.613
C1813-21 Cell 4	0.664	32.67	77.82	16.888
C1813-21 Cell 6	0.667	33.19	77.52	17.168
C1924-1 Cell 4	0.724	30.82	78.19	17.449
C1924-1 Cell 5	0.717	30.81	77.44	17.118
C1924-1 Cell 6	0.714	30.95	77.07	17.039

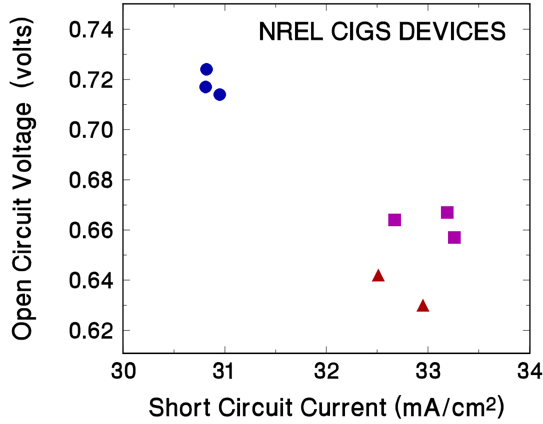

FIG. 5. Open circuit voltage *vs.* short circuit current for the eight NREL CIGS devices listed in Table VII: ▲ for the C1919 devices, ■ for the C1813 devices, and ● for the C1924 devices.

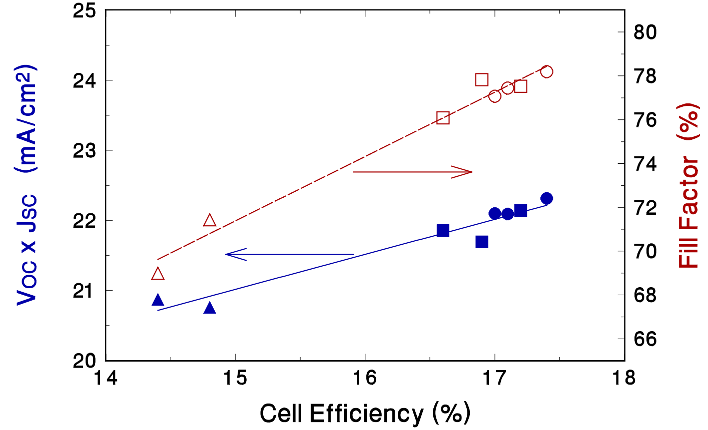

FIG. 6. Relationship of V_{OC}-J_{SC} products and Fill Factors to overall CIGS device efficiencies. This seems to indicate a dominant role for the Fill Factors in the overall device performance. The symbols shapes are used in the same manner as in Fig. 5.

might be able to identify differences that might be correlated with those variations in performance. We therefore obtained three samples, each containing 6 devices, with average efficiencies in the 14-15% range (C1919-11), in the 16-17% range (C1818-21), and in the 17-18% range (C1924-1). Among the total of 18 devices, 4 or 5 seemed anomalous (primarily because of low shunt resistances) and we selected 8 of the remaining devices for detailed study that seemed to represent a good range of performance parameters. The performance parameters of the 8 devices we chose to characterize in detail, using admittance, DLCP profiling, and CV profiling (see Section 6.2), are listed in Table VII.

Some useful insight into the performance parameters of these 8 samples is obtained by examining the plots of Fig. 5 and 6. In Figure 5 we examine the relationship between the open circuit voltage and short circuit current, while in Figure 6 we examine the relation between the device efficiency and both the Fill Factor and the V_{OC}-J_{SC} product. Figure 5 indicates that the 3 devices from sample C1924-1 are somehow distinctly different from the other 5 devices in that they have significantly higher values of V_{OC} and lower values of J_{SC}. One contributing factor is the fact that the absorber in C1924-1 contains on average a slightly higher fraction of Ga than did samples C1813-21 or C1919-11. This is revealed in SIMS measurements used to deduce the Ga-to-In profiles that are displayed in Fig. 7.

Figure 6 indicates that the variation in efficiencies for these 8 devices is correlates most strongly with Fill Factor, but that the V_{OC}-J_{SC} product increases monotonically with device efficiency as well. There were no obvious correlations between device efficiencies and either the open-circuit voltage or short-circuit currents for this set of samples.

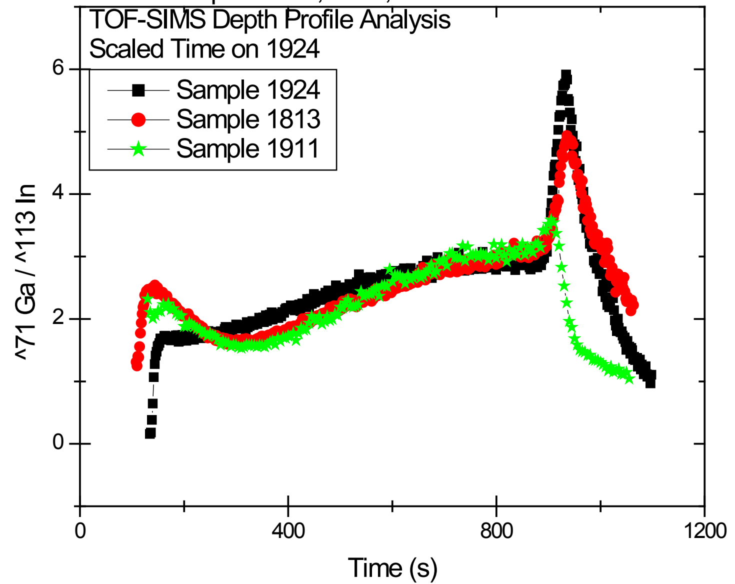

FIG. 7. SIMS determined spatial profiles of the Ga-to-In ratios for representative NREL CIGS sample devices from each of the three depositions. Note that these profiles for samples 1813 and 1911 appear nearly identical, but that the profile for sample 1924 indicates a slightly higher overall Ga fraction. These data were obtained using the TOF-SIMS instrument at the CAMCOR facility at the University of Oregon.

2.3.2 NREL SAMPLES TO STUDY VARIOUS TYPES OF COMPOSITIONAL GRADING

A series CIGS samples were grown by various vacuum co-evaporation methods at the National Renewable Energy Laboratory (NREL) and provided to Nanosolar Inc. for study. Nanosolar then provided us with a subset consisting of four samples in the summer 2008 for further study by our experimental methods. One device was deposited with a uniform Ga depth profile (x=0.3, with x=Ga/(In+Ga), η=15.1 %) to serve as a reference device; one device closely matched NREL's optimally bandgap grading scheme ("V-shaped" as shown in Fig. 8, with an efficiency η of 16.3 %), and two with the Ga fraction decreasing roughly linearly from x=0.9 at the Mo back contact to either x=0.15 (η=17.1 %) (Monotonic A), or x=0.25 (η=15.3 %) (Monotonic B) as also shown in Fig. 8. As listed in Table VIII the compositionally graded devices all had values of V_{OC} close to 0.66 V, while V_{OC} for the uniform control sample was

Table VIII. Cell performance parameters for devices fabricated at NREL with different Ga/(Ga+In) grading profiles. Those grading profiles are displayed in Fig. 8.

Grading Type (Cell #)	V_{OC} (volts)	J_{SC} (mA/cm^2)	FF (%)	Efficiency (%)
Uniform (C2226-12 #2)	0.636	31.7	74.8	15.1
Monotonic A (C2228-12 #4)	0.665	30.5	75.5	15.3
Monotonic B (C2230-12 #4)	0.656	35.2	74.0	17.1
V-shaped (C2233-12 #4)	0.655	34.0	73.4	16.3

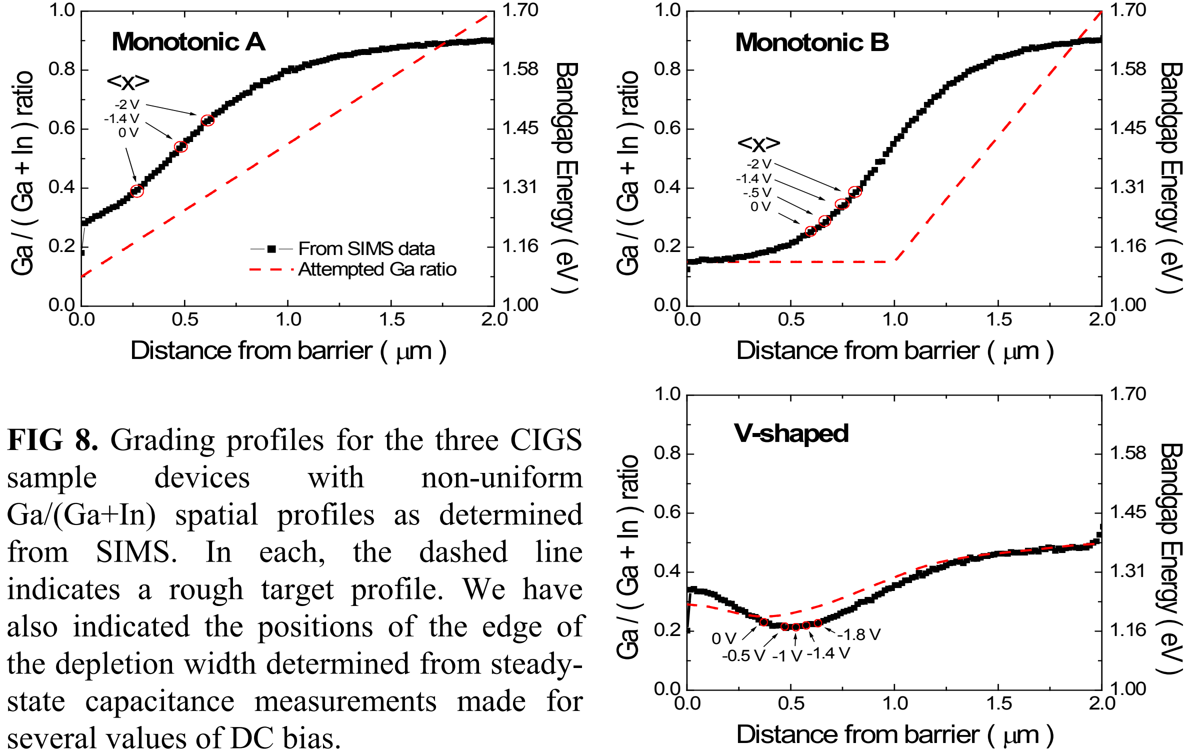

FIG 8. Grading profiles for the three CIGS sample devices with non-uniform Ga/(Ga+In) spatial profiles as determined from SIMS. In each, the dashed line indicates a rough target profile. We have also indicated the positions of the edge of the depletion width determined from steady-state capacitance measurements made for several values of DC bias.

slightly lower (0.64 V). Also note the significant increase in J_{SC} for the Monotonic B and V-Shaped compositionally graded samples.

2.3.3 IEC SAMPLE DEVICES: THE ROLE OF SODIUM ON CIGS SOLAR CELLS

The addition of Na to $Cu(InGa)Se_2$ based solar cell devices is a commonly followed procedure, boosting the efficiency by up to 50% primarily through a sizeable increase in the open-circuit voltage (V_{oc}) and the fill factor (FF). Although the positive role of Na is well known in the fabrication of CIGS devices, there is an ongoing debate as to the exact mechanism of the beneficial effect of Na, with much of the debate centering around where in the cell the Na has its effect. Possible sites are grain boundaries, in the bulk of the grains, or the CdS/CIGS

Table IX: Device performance parameters of two matched pairs of CIGS devices. Deposition A was carried out simultaneously onto 2 Soda lime substrates, where one of which had a SiO_2 barrier to inhibit Na diffusion into the CIGS layer. Deposition B was carried out simultaneously onto one soda lime substrate and onto a Ti foil substrate.

Deposition	Sample	V_{OC} (V)	J_{SC} (mA/cm^2)	FF (%)	Eff (%)
A	CIGS on Soda-lime Glass	0.624	32.9	74.0	15.2
	Reduced Na CIGS (SiO_2 barrier)	0.494	33.6	64.3	10.7
B	CIGS on Soda-lime Glass	0.651	29.9	77.1	15.0
	Na free CIGS (Ti substrate)	0.522	30.1	65.1	10.2

heterojunction. Recent experimental results appear quite contradictory, with one group finding no evidence of Na at the grain boundaries[4] and another group concluding that the Na is only found in significant amounts at the grain boundaries[5]. Another group hypothesized that the Na acts only during the growth of the sample to organize and passivate point defects[6]; however, this is disputed by similar benefits obtained through diffusion of Na into the sample in a post-deposition treatment[7].

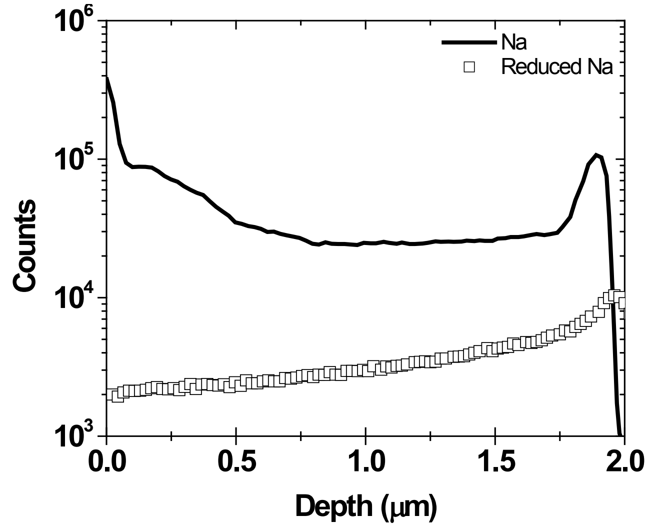

FIG. 9. SIMS depth profiles of a matched pair of higher and lower sodium $Cu(InGa)Se_2$ sample devices.

One pair of matched baseline and reduced Na samples were provided to us by the Institute of Energy Conversion in May, 2006. The CIGS films were deposited simultaneously onto soda lime glass substrates, but one of them was capped with an SiO_2 layer to inhibit Na diffusion into the CIGS absorber. The level of Na reduction compared to the baseline sample is displayed in the SIMS profiles shown in Fig. 9. We received a second matched pair of samples in May 2007. In this case one film was deposited onto Ti foil so that the Na level was virtually absent. All the samples were co-deposited at 550°C in a single deposition with a thickness of 2.0 μm. The baseline film was deposited on a Mo-coated soda lime glass substrate and the reduced Na film was deposited on a substrate provided by Shell Solar which had a SiO_2 diffusion barrier below the Mo. All devices were completed with standard CdS, ZnO and ITO depositions and a Ni/Al grid.

Ultimately, we found no substantial differences between the properties of the sample deposited on the SiO_2 coated glass substrate or the sample deposited on the Ti substrate. Table IX provides typical performance parameters for the cells studied, and illustrates the well known effects of Na on CIGS devices; namely, a ~130meV increase in V_{OC}, leading to a nearly 50 % increase in efficiency, with little effect on the short circuit current. Table IX also provides the device performance parameters of the cells analyzed and discussed below. These parameters were typical for all of the cells on these two pairs of samples.

3.0 EXPERIMENTAL CHARACTERIZATION METHODS

The measurements employed in our studies rely on a set of experimental techniques which have all been described previously in some detail. They consist of (1) admittance spectroscopy as a function of temperature and frequency, (2) drive-level capacitance profiling, and (3) transient photocapacitance taken together with transient junction photocurrent spectroscopy. Here we will summarize each method only very briefly.

3.1 ADMITTANCE SPECTROSCOPY

All of the sample devices studied contain a depletion region whose complex admittance is characterized as a function of temperature and frequency before we undertake the more sophisticated capacitance based measurements described in Sections 3.2 and 3.3 below. Such measurements provide us with an estimate of our film thickness (the temperature independent region at low T is simply related to the geometric thickness, d, by the formula $C = \varepsilon A/d$), and an Arrhenius plot of the frequency of the lowest temperature capacitance step (or conductance peak) *vs*. 1/T provides us with the activation energy of the ac conductivity, E_σ, which we sometimes identify with the Fermi energy position: $E_\sigma = E_C - E_F$.[8] These admittance measurements also give us an indication of the quality of our barrier junction which allow us to pre-screen our samples for further study.

3.2 DRIVE-LEVEL CAPACITANCE PROFILING

The drive-level capacitance profiling method has been described in detail in many publications [9,10,11,12]. It is similar to other kinds of capacitance profiling in that it provides us with a density *vs*. distance profile; however, this particular method was developed specifically to address the difficulties encountered in interpreting capacitance measurements in materials with defect densities comparable to carrier densities. In this method we determine the junction capacitance both as a function of DC bias, V_B, and as a function of the amplitude of the alternating exciting voltage, δV: $C(V_B,\delta V) = C_o(V_B) + C_1(V_B)\,\delta V + \dots$

An expression involving the coefficients C_0 and C_1 can then be used to deduce the free carrier density, n, plus an integral over the density of mobility gap defect states; specifically:

$$N_{DL} \equiv \frac{C_0^3}{2q_e \varepsilon A^2 C_1} = n + \int_{E_C - E_e}^{E_F^o} g(E)dE \quad \text{(n-type)} \quad \text{or} \quad = p + \int_{E_F^o}^{E_V + E_e} g(E)dE \quad \text{(p-type)} \qquad (1)$$

Here E_F^0 is the bulk Fermi level position in the sample and E_e depends on the frequency and temperature of measurement:

$$E_e(\omega,T) = k_B T \log(\nu/\omega) \qquad (2)$$

Thus, by altering the measurement temperature (or frequency) we obtain information about the energy distribution of the defects and, by altering the applied DC bias, we can vary the spatial region at which we detect the defects in the sample. That is, we can spatially profile the defects as a function of the position from the barrier interface.

3.3 TRANSIENT PHOTOCAPACITANCE AND PHOTOCURRENT

The methods of junction transient photocapacitance and photocurrent have been discussed by us in great detail over the years in the literature [13,14,15] and also in many previous NREL reports. They represent types of sub-band-gap optical spectroscopy and provide spectra quite similar in appearance to PDS derived sub-band-gap optical absorption spectra or to CPM spectra. Instead of detecting absorbed energy, however, our photocapacitance and photocurrent transient methods detect the optically induced change in defect charge within the depletion region.

In this method the space charge region of the semiconductor near the barrier junction is first subjected to a voltage "filling pulse". This pulse causes a non-equilibrium (filled) occupation of gap states to be established. As time progresses, the initial steady-state population is recovered through the excitation of trapped electrons to the conduction band where they can then move out of the depletion region under the influence of the electric field. In the dark this process proceeds entirely by the thermal excitation of trapped carriers. However, this process can be enhanced through optical excitation and this is the basis of the photocapacitance and junction photocurrent techniques.

The re-equilibration can be observed by the redistribution of trapped carriers, either as a change in the *junction capacitance* (which occurs because the depletion region will contract as negative charge is lost and the positive charge density increases) or by monitoring the *current* which results from the motion of this charge. However, the observation of capacitance transients has one significant difference compared to current transient measurements: The dominant type of emitted carrier (electron or hole) can be identified by the *sign* of the observed change in capacitance.

Figure 10 distinguishes four types of optical transitions involving gap states, illustrated here for an n-type material.[16] Type (a) is the removal of an electron from an occupied defect level into the conduction band with the subsequent escape of the electron. Type (b) represents the optical excitation between the valence band and an unoccupied defect states with the subsequent escape of the valence band hole. Such a transition results in a photocapacitance signal of negative sign. Generally, such negative photocapacitance signals occur only in very intrinsic material and are even fairly rare in those cases. However, they have been recently been observed

in some HWCVD a-Si,Ge:H samples discussed in Section 5, and in some of the nc-Si:H mixed phase material discussed in Section 4.

Transitions of type (c) are similar to type (a) except that, because the hole left in the gap state lies close to the valence band, it will be quickly thermally emitted into the valence band where it then also escapes the depletion region. Such a case results in no change in charge state within the depletion and, hence, no photocapacitance signal. Similarly, [Type (d)] for a transition from the valence band into an unoccupied gap state close to the conduction band, the electron will be quickly thermally emitted into the conduction band and leave the depletion region as well, with nearly zero photocapacitance signal. Transitions of types (c) and (d) will be dominant when the photon energy lies only slightly below the bandgap energy. In those cases, then, each photon effectively produces one valence band hole plus one conduction band electron with no net change in the gap state occupation. However, the photocapacitance signal in this energy regime does not vanish; rather, it is substantially *positive* in all cases. This thus indicates that photogenerated majority carriers are more likely to escape the depletion region than the photogenerated minority carriers. Moreover, while transitions of types (c) and (d) result in small changes in the junction capacitance, they result in a large junction photocurrent.

We can use such comparisons to estimate the relative collection fractions for minority *vs.* majority cases. If our sub-bandgap light results in n_e electrons and n_h holes leaving the depletion within the experimental time window, then the junction photocurrent signal will be proportional to their *sum* while the photocapacitance signal will be proportional to their *difference*. Thus, it is really only by measurements of *both* the transient photocapacitance (TPC) signal *as well as* the transient photocurrent (TPI) signal that we can truly distinguish the quantities of holes and electrons excited out of the depletion region due to the sub-bandgap light. This ability to distinguish electron from hole processes is unique among all the various types of sub-band-gap optical spectroscopies.

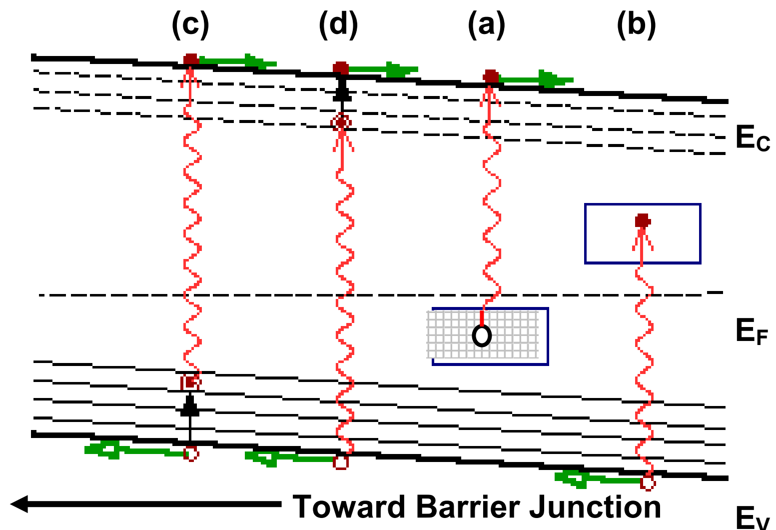

FIG. 10. Schematic of four different types of sub-bandgap optical transitions. Optical transitions are shown by the wavy lines, and thermal transitions are shown by the vertical solid arrows. Horizontal arrows indicate the subsequent motion of the released carriers.

4.0 PROPERTIES OF UNITED SOLAR NANOCRYSTALLINE SILICON

We began an effort to understand nanocrystalline silicon materials several years ago, and some of our most successful results have been obtained on sample devices obtained from United Solar Ovonic Corporation. Our first results on these materials were published in early 2006 [17] under funding by our previous NREL Subcontract. Those samples were not actual solar cells, but instead a special sandwich structure incorporating two a-Si:H cladding layers to prevent oxygen diffusion into the nc-Si:H layer. In 2006 we presented results on a newer series of nc-Si:H samples that were actual n-i-p working devices. These results appeared in the Conference Proceedings of the Materials Research Society [2006, Publ. 1] For that study we focused on samples with smaller crystalline fractions since those seemed to exhibit the best performance. Since then we have been examining a fairly extensive series of new sample devices that were deposition using different hydrogen profiling functions, and also which encompassed a wider range of crystalline fractions (see Section 2.1 above). The results on this newer sample series appeared in the Journal of Non-Crystalline Solids [2008, Publ. 7] and Conference Proceedings of the Materials Research Society [2008, Publ. 9].

4.1 DRIVE-LEVEL CAPACITANCE PROFILES *vs.* HYDROGEN PROFILES

In Fig. 11 we display the DLC profiles obtained for the deposition with constant hydrogen dilution at two locations corresponding to very different crystalline fractions (15125-74 and 15125-94). Results both in the annealed state (State A) and a light degraded state (State B) are shown. The light-soaked state was produced by exposing each sample to 610nm bandpass filtered light from a tungsten-halogen light source at $500mW/cm^2$ intensity for 100 hours. The 785nm Raman spectra are shown again for reference. The response in these drive-level profiles do not provide significant evidence that the functionally graded H_2 dilutions directly affected the variation of the defect densities over the film thickness. Rather, the deep defect response, which is manifested as an increase in DLCP density with temperature, was found to be highly dependent on the crystalline volume fractions in the neighborhood of the ITO contact where each profile was taken. Specifically, a significant deep defect response after light-soaking was *only* observed in the drive-level profiles for the most crystalline materials. Also, in agreement with our previously reported results, that light-soaking actually slightly decreased the deep defect response for the more amorphous sample. This, we believe, is due to a downward shift of the relative electrical potential of the amorphous phase relative to the nano-crystallite phase. [18] In contrast, however, the deep defect response for the more crystalline sample is substantially increased after light-soaking.

785nm Raman

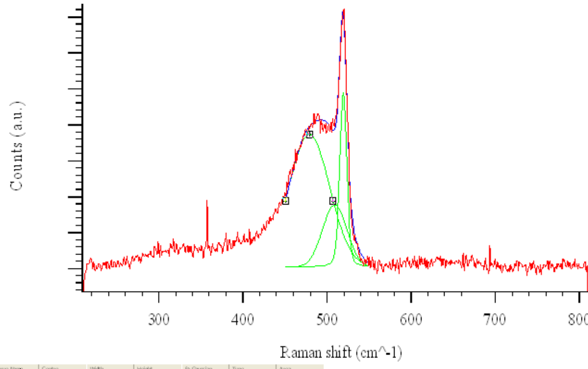

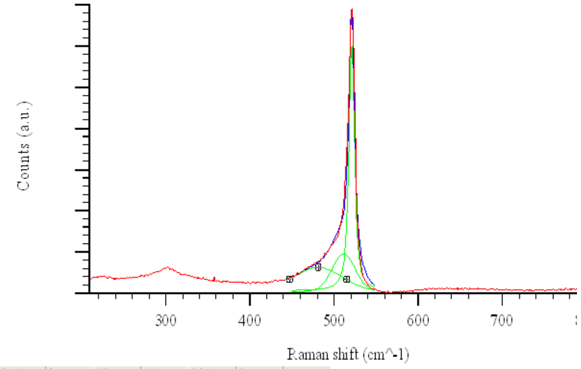

DLCP, State A

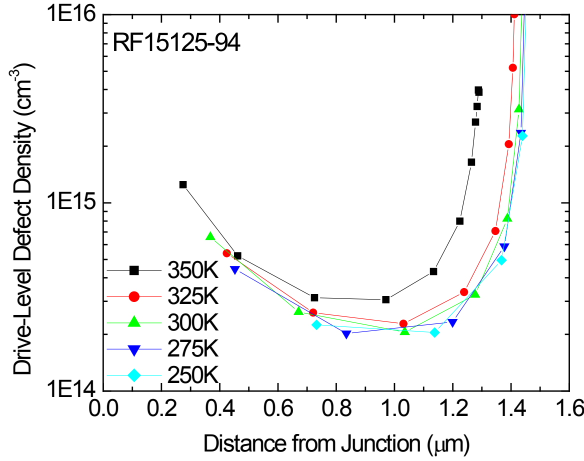

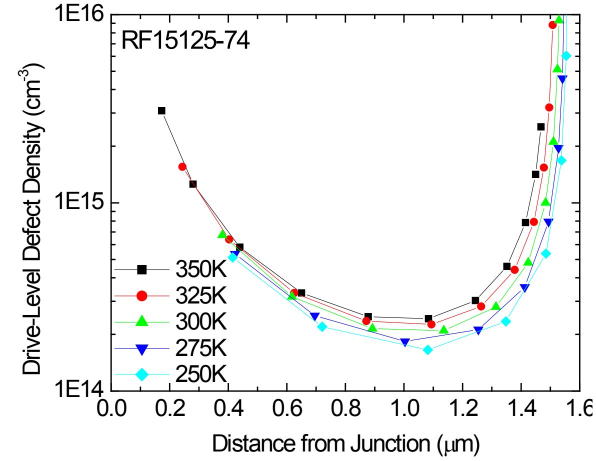

DLCP, State B

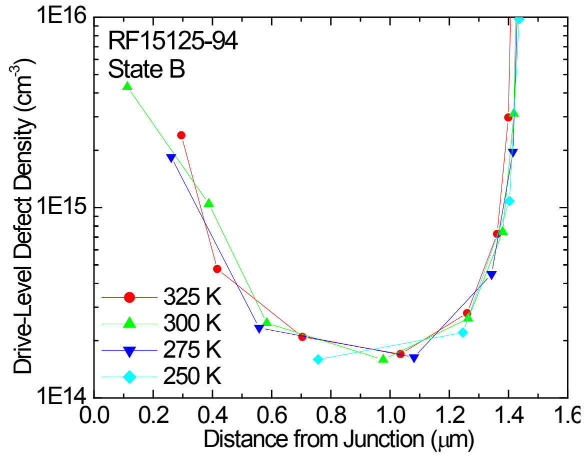

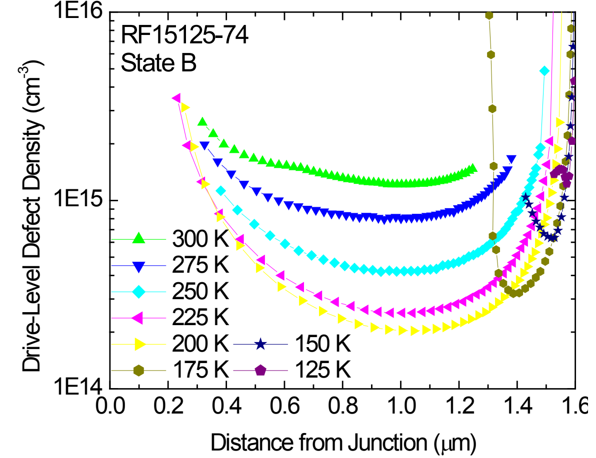

FIG. 11. Raman spectra and drive-level profiles for the least and most crystalline nc-Si:H samples from deposition 15125, before and after light-soaking. Consistent with our previous results on lower crystalline fraction samples [18], light-soaking actually appears to decrease the DLCP defect density for sample 15125-94. However, for the higher crystalline fraction sample 15125-74, light-soaking significantly increases the deep defect response.

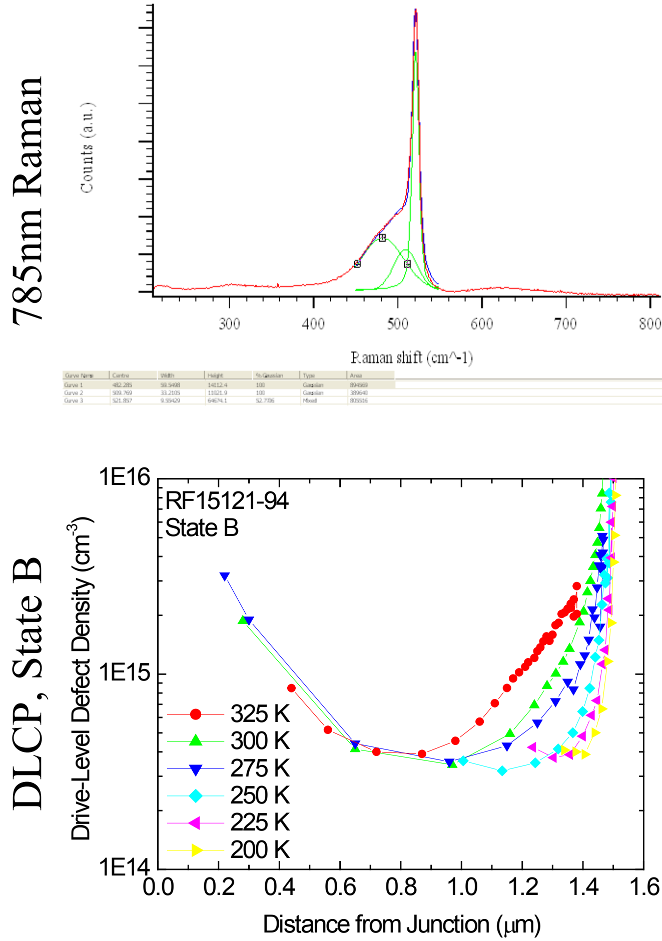

FIG. 12. Raman spectrum and State B drive-level profiles for deposition 15125 in a region with a crystalline fraction that is intermediate between those displayed in Fig. 11. Note that the light-induced degradation in this case results in an increase in the deep defect response in only one spatial region of the sample, and this likely corresponds to the region with the higher crystalline fraction.

In Fig. 12 we display the DLCP profiles in the light degraded states for a third sample from this deposition (15125-75) whose Raman spectrum indicated a degree of crystallinity intermediate between those of Fig. 11. Here we observe a variation in the electronic properties after light-soaking, presumably reflecting a region with higher crystalline fraction near the top region of this sample. This corresponds to later in the deposition and, indeed, using a constant level of hydrogen dilution we would expect the crystalline fraction to increase during film growth.

Even though the DLCP densities we determined were well correlated with the crystalline volume fractions, strong correlations were *not* seen between crystal volume fraction and the cell performance parameters such as FF. However, when a comparison was made between the open-circuit voltage and crystalline fraction (Fig. 8) a general trend of a monotonic decrease in V_{oc} with increasing crystalline fraction was observed. Strong deviations in this trend occurred only in the cases of the most disordered cells grown under the most strongly varying H_2 dilution conditions. We believe it likely that such deviations arise from a concentration of disorder in these cells in a relatively small volume of the intrinsic layer in the neighborhood of the $p+/i$ junction.

4.2 SUB-BAND-GAP PHOTOCAPACITANCE AND PHOTOCURRENT SPECTROSCOPY

For the early 2006 set of five samples obtained from USOC, two were deposited on specular stainless steel (SS) substrates, while three employed textured Ag/ZnO substrates. It is well known that substrate texturing enhances the spectral response of a device, especially for long wavelength photons. Although substrate texturing in these samples is clearly necessary to achieve the highest conversion efficiencies, texturing also significantly modifies the spectral response that we obtain in our sub-bandgap absorption spectra, and yields a somewhat distorted representation of the optical response of the nc-Si:H film itself. Figure 13 illustrates this point by comparing two transient photocurrent spectra for one textured substrate sample device (13993) with one without texturing (14036), both deposited in a similar manner with hydrogen profiling. The textured sample's flattened TPI response above roughly 1.3 eV, and its apparently broader Urbach energy below 1.1 eV are attributed to light-trapping effects. The specular sample is thus believed to show a much less distorted picture of the actual nc-Si:H optical absorption properties.

In order to obtain a more complete picture of the energy distribution of the defects, we also began to compile TPC and TPI spectra for a subset of these samples. As previously reported [17, Publ. 1,7,9] these defects appear in the sub-bandgap absorption spectra at energies of roughly half the *a*-Si:H bandgap (Fig. 14). In addition, these spectra indicated a strong temperature-dependence in the minority carrier collection, as determined from the ratio: TPC/TPI $\propto$ $(n - p)/(n + p)$. Generally, it has been observed that the devices having a stronger crystalline TPC nature (that is, those exhibiting a response characterized by an apparent band edge of ~1.2eV, such as in Fig 14a) also exhibit lower relative fractions of minority carrier collection above the crystalline Si bandgap energy. On the other hand, those materials exhibiting TPC

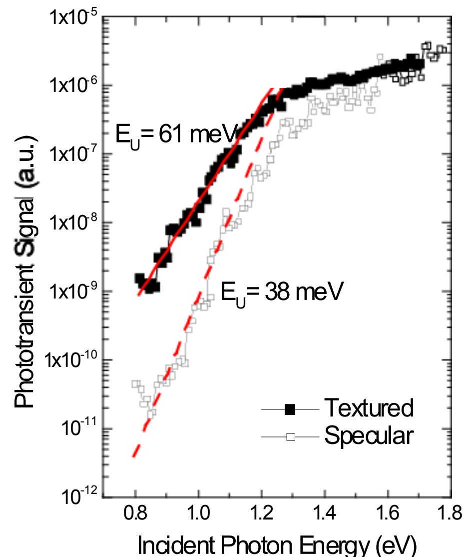

FIG 13. TPI spectra for nc-Si:H samples deposited on specular (solid symbols) and textured substrates (open symbols) are aligned at the higher optical energies for comparison purposes. The flatter optical response for the textured substrate sample above 1.2eV, as well as its apparently broader Urbach tail, are attributed to the light-trapping effect due to the textured substrate. Thus, the spectrum for the device deposited on the specular SS substrate is believed to more accurately represent the optical absorption properties of the intrinsic nc-Si:H layer itself.

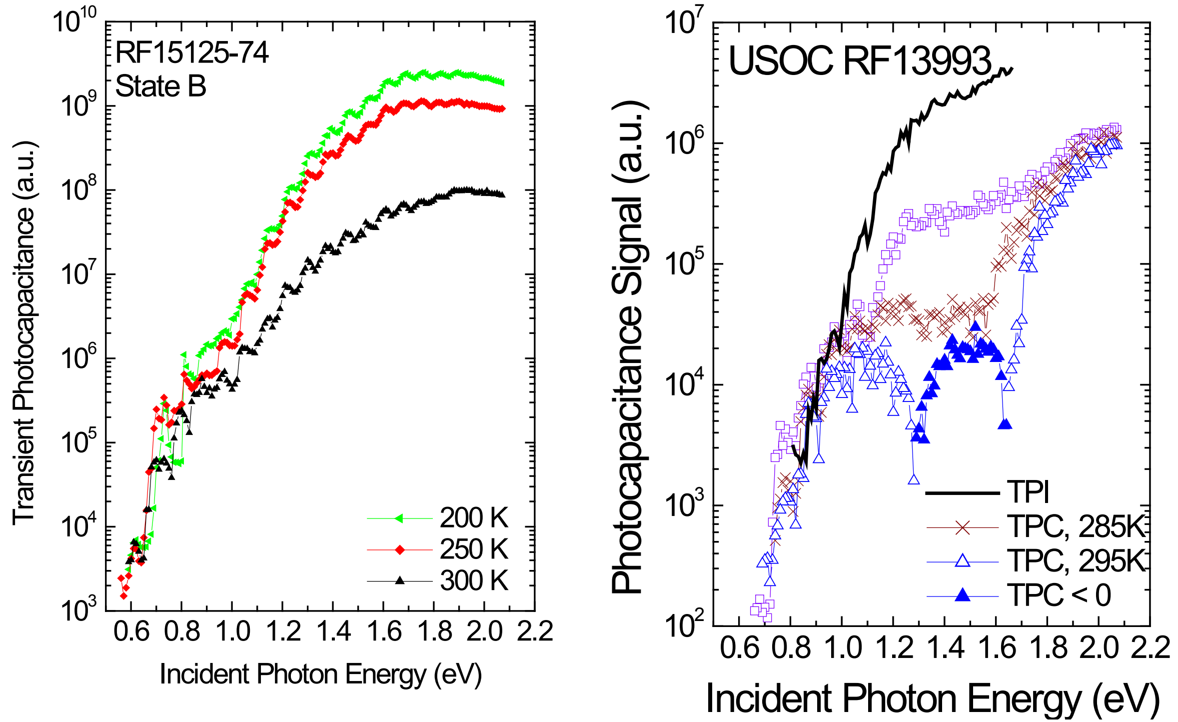

FIG 14. Transient photocapacitance (TPC) and transient photocurrent (TPI) spectra for a device with X_c=0.72±0.5 (Fig. 14a) and a previously measured device with X_c=0.53±0.5 (Fig. 14b) at different temperatures showing notably different degrees of minority carrier collection.

spectra with a visible *a*-Si:H bandtail below 1.8eV (Fig. 14b) seemed to exhibit much larger relative minority carrier collection fractions. Indeed, the TPC spectrum increases by more than a factor of 100 near 1.5 eV, indicating a corresponding decrease in the net hole collection at this photon energy. An even more dramatic change is observed when the temperature is raised to 295 K in this sample: the TPC signal actually becomes slightly *negative* near 1.5 eV.

The detailed temperature dependence of the photocapacitance signal at an optical energy of 1.5eV is displayed in Fig. 15. The absolute value of these negative data points are plotted as solid symbols. The negative signal indicates that *more* holes are being collected than electrons at these optical energies, probably because some of the photo-excited electrons become deep trapped and cannot escape during the 500 ms time window of our measurement. Therefore, the slight negative response in this region is not in itself so important; rather, it simply reflects that some electron trapping is occurring and that the hole collection is extremely good. Note that the signal again becomes positive at low optical energies since single-carrier excitation processes dominate in the deep defect region, and it is also positive at higher optical energies because the a-Si:H contribution with its lower hole collection fraction is larger in this region.

The data in Fig. 15 also suggest that the hole collection is thermally activated. At lower temperatures, when the hole collection was strongly suppressed, we obtained an activation

FIG 15. Variation of TPC signal with temperature at an optical energy near 1.5eV. A positive constant was added to the TPC signal to allow these data to be plotted on a logarithmic scale (the negative region is indicated by the solid symbols). We chose the constant which best extended the exponential dependence into the regime above 270K. This graph indicates thermally activated behavior for hole collection and, in contrast with previous results showing a single activation energy near 0.2eV, this sample reveals a second regime at higher temperatures with a significantly larger activation energy.

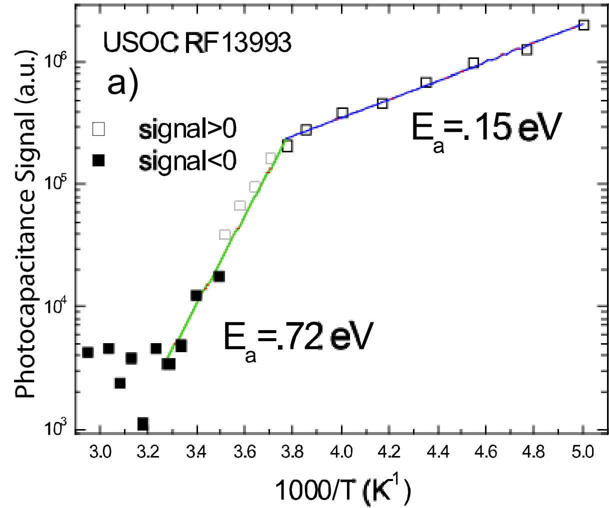

energy for hole collection near 0.15eV, very similar to that found previously [17]. However, in the temperature regime above 270K, a significantly larger activation energy near 0.72 eV was exhibited. We tentatively attribute this to hole trapping into deep defects, possibly Si dangling bonds in the amorphous component. The fact that this deeper hole trapping accounts for only about 10% of the total (by comparing the magnitudes of hole collection at 200K and 300K) seems consistent with the idea that these deeper defects reside in the phase with lesser volume fraction in these materials; that is, the amorphous phase.

As indicated in the comparison of the two samples in Fig. 14, the relative hole collection is strongly sample dependent. For the three textured samples: 13993, 14027, and 14037, we determined the relative hole collection fractions at 300 K by aligning TPC and TPI spectra in the defect regime at 0.9 eV and then determining the average TPC/TPI ratio near an incident optical energy of 1.5 eV. This provided an estimate of the ratio $(n-p)/(n+p)$, from which the ratio p/n of collected holes relative to electrons could be determined. As indicated in Fig. 16, this analysis

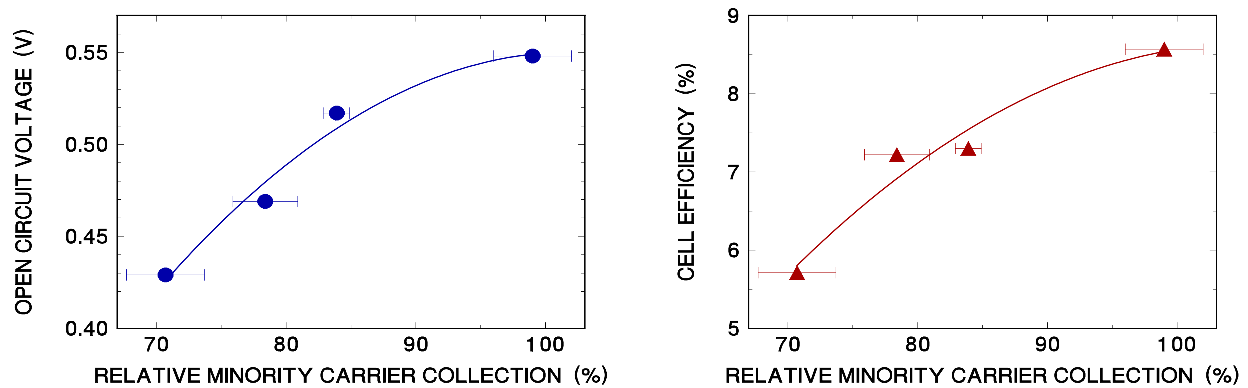

FIG. 16 Open circuit voltage and cell efficiency *vs.* minority carrier collection for four nc-Si:H devices deposited on Ag/ZnO textured substrates: 13993, 14027, and 14037, plus one from and older sample series. The minority carrier collection fractions were determined from TPI/TPC ratio at 300K near 1.5eV

for the three textured samples studied indicates a good correlation between the *n/p* collection ratios determined in this fashion and the cell conversion efficiencies. However, a much larger number of samples should be examined before taking this result too seriously.

In Section 2.1 we acknowledged that we had received a 2005 series of nc-Si:H sample devices from United Solar (see Table I). However, corresponding measurements on this series of samples were not very easy to carry out. We believe the reason was that these samples were too thin for our measurement methods; less than 0.9 microns based upon the capacitance freeze-out values. In contrast, the second series of samples appeared to be at least 1.3 microns thick based upon their capacitance freeze-out values. Moreover, the defect densities in these both current series of United Solar samples were much lower than those provided to us previously. This meant that many of our measurements had to be extended into forward bias to avoid depleting the entire i-layer of these devices.

In Fig. 17 we present our best set of TPC spectra obtained from the earlier set of nc-Si:H samples. These were obtained for MVHF device 2B10514, which was deposited onto specular stainless steel. As with our reported TPC spectra on the previous series of nc-Si:H devices, we observe a decrease in TPC signal above the Si bandgap as the measurement temperature is increased. This is due to an increasing fraction of hole collection with increasing temperature. Indeed, at 325K it appears that only the defect portion of the spectrum remains visible. We also observed that the hole collection fraction was significantly better for the annealed state spectra (not shown) compared to those taken after prolonged light exposure. However, in contrast to

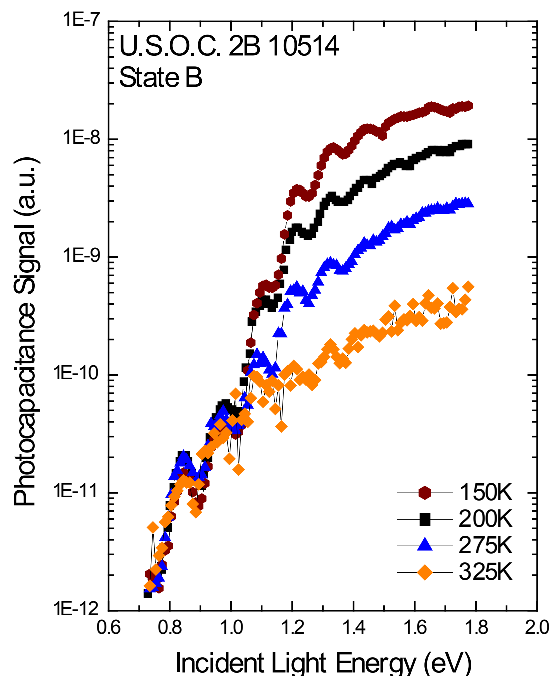

FIG. 17. Photocapacitance spectra for nc-Si:H sample device 2B10514 in its light degraded state. Spectra were taken at 1.1kHz with the ambient reverse bias at –0.2volts and filling pulse height of 0.3volts (to +0.1volts). The signal magnitude decreases above the Si bandgap with increasing temperature due to the increasing fraction of holes collected. The defect band signal is nearly temperature independent and much larger in magnitude than for the previous series of United Solar nc-Si:H samples studied. This is probably due to an insufficient thickness of the i-layer in these sample devices, so that the spectra are dominated by the properties of the material near the back contact; that is, in the n^+ region of the sample device.

those earlier reported spectra we did not observe an a-Si:H component to these spectra at higher measurement temperatures. Also, the defect portion of the spectrum is nearly 100 times larger than for those observed in the previous series of samples.

We believe that these differences arise from the insufficient thickness of the i-layer since, during the capacitance transient, the edge of the depletion region actually will expand beyond its position under ambient reverse bias. Because these i-layers are already nearly completely depleted under small values of reverse bias, this means that the edge of the depletion region extends into the n^+ layer near the back contact after the filling pulse and during the transient. Moreover, the region near the edge of the depletion region contributes more strongly to TPC signals than the interior region. This means that the spectra shown in Fig. 17 may be dominated by the n^+ nc-Si:H layer near the substrate contact. This would account both for the larger defect magnitude and the absence of visible a-Si:H component.

4.3 LIGHT-INDUCED DEGRADATION IN NANOCRYSTALLINE SILICON

Although nc-Si:H does not suffer as severely from light exposure as amorphous silicon, prolonged light soaking typically reduces the conversion efficiency by several percent [19]. Several of our samples were examined both in "State A", after a sample had been annealed for one hour at 450 K, as well as in "State B", a degraded state which we obtained by exposing the sample to 20 hours of red-filtered light (>620 nm) from a tungsten-halogen source at an intensity of 400 mW/cm^2. Effects of such light soaking could be observed both in the photo-transient spectra as well as in drive-level capacitance profiles (DLCP). The effect of light soaking on the TPC spectra of sample 13993 is shown if Fig. 18. We see that the TPC signal changes significantly. In particular, the negative signals near 1.5 eV become significantly positive in State B. This corresponds to a loss of hole collection, even more than was achieved by reducing the measurement temperature from 295 K to 275 K in State A (see Fig. 14).

In numerous previous studies of light-induced degradation in a-Si:H, DLCP measurements always clearly revealed a systematic increase in the density of deep defects, by factors varying from roughly 2 to almost 50.[20,21] However, our previous DLCP studies for nanocrystalline materials indicated almost no change.[22] and, moreover, very little evidence for a deep defect thermal response at all. In contrast, for some of the current series of nc-Si:H devices, particularly for samples 13993 and 14036, the DLCP measurements have revealed a significant deep defect response, as is illustrated in Fig. 11. This may partly be due to the smaller effective doping levels in these samples which allow us to more clearly observe the contribution from the deep defects. What is even more surprising, however, is that when such a deep defect response is apparent, we consistently find that it *decreases* after prolonged light exposure (see Fig. 11).

To explain the observed effects of light-soaking on the DLCP and TPC measurements, we tentatively propose a microscopic degradation model. First, we note that that DLCP density represents the integral over the density of states in the gap between the Fermi level and a thermal response energy. Thus, the observed decrease in drive level density may result from defects effectively "shifting out" of the energy region defined by our DLCP measurement parameters. At the same time, the observed reduced hole-collection implies an impediment to hole transport. Both of these effects could result from of a shift in the potential distribution between the nanocrystalline and amorphous phases of these materials, as shown in Fig. 19. Such a shift in the relative potentials of the two phases might occur during light-soaking by a separation of the photo-generated charges, with positive charge accumulating at the amorphous-nanocrystalline phase boundary, and compensating negative charge being added to the dangling bond defects within the amorphous regions. Future studies will hopefully test some of the other possible implications of such a microscopic model.

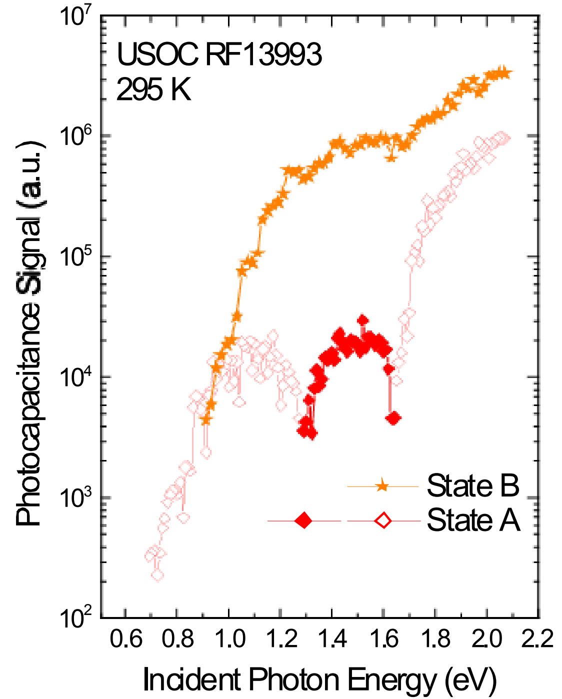

FIG 18. Comparison of the 295K TPC spectra for nc-Si:H sample 13993 before & after light-soaking. We see a dramatic increase in the magnitude of the TPC spectrum, especially in the regime where the annealed state had exhibited a negative TPC signal. This is due to a substantial reduction in the minority carrier collection.

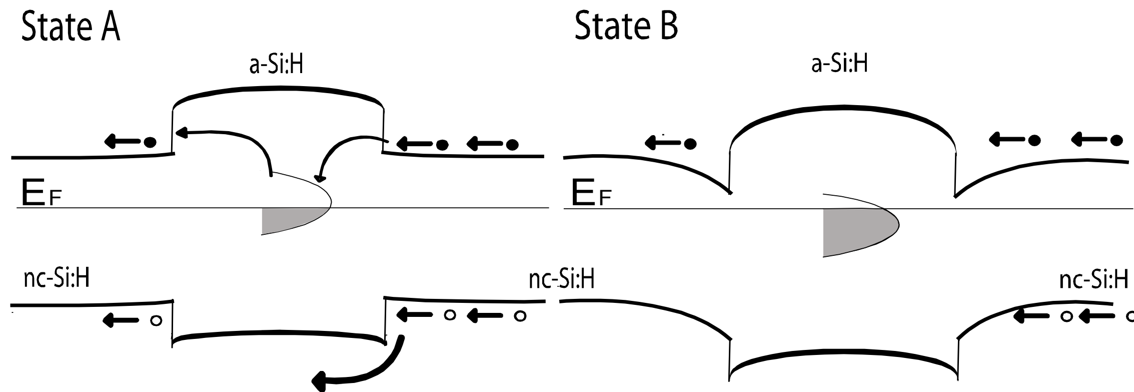

FIG 19. Schematic of a possible model to explain light-induced changes observed in the drive-level profiles and the photocapacitance spectra of nc-Si:H. In State B, defects have shifted down in energy with respect to the bulk conduction band and holes see a larger potential barrier at the phase boundary. In the scenario illustrated, positive charge has collected at the a-Si:H/crystallite interfaces, and is compensated by negative charge in the a-Si:H region, as well as in the crystallite nearby.

5.0 NREL HOT-WIRE AMORPHOUS SILICON-GERMANIUM ALLOYS

5.1 REVIEW OF PREVIOUS WORK

A few years ago we reported that a-Si,Ge:H alloys grown by the hot-wire chemical vapor deposition (HWCVD) method could exhibit electronic properties as good as the best glow discharge (PECVD) a-Si,Ge:H alloy films.[23,24] This resulted from replacing the usual tungsten filament with tantalum and using a filament temperature of ~1800°C instead of ~2000°C. In 2005, however, a new series of such a-Si,Ge:H films were found to have substantially inferior properties. Comparisons between the TPC spectra of these later sample properties with those of the early superior sample properties are shown in Figs. 20 and 21. Here we clearly observe significantly higher defect densities and broader bandtail distributions for the 2005 samples. Subsequent SIMS analysis determined that these more recent samples contained significantly higher oxygen levels due to a contaminated GeH_4 gas line. This apparent sensitivity to oxygen impurities was, however, very surprising because similar levels of oxygen have not been found to appreciably affect the properties of a-Si:H. [25]

5.2 STUDIES OF THE EFFECTS OF OXYGEN ON HWCVD a-Si,Ge:H ALLOYS

The source of oxygen contamination during the HWCVD growth process was identified and eliminated in the Fall, 2005. We then decided to investigate the effect of a controlled change in

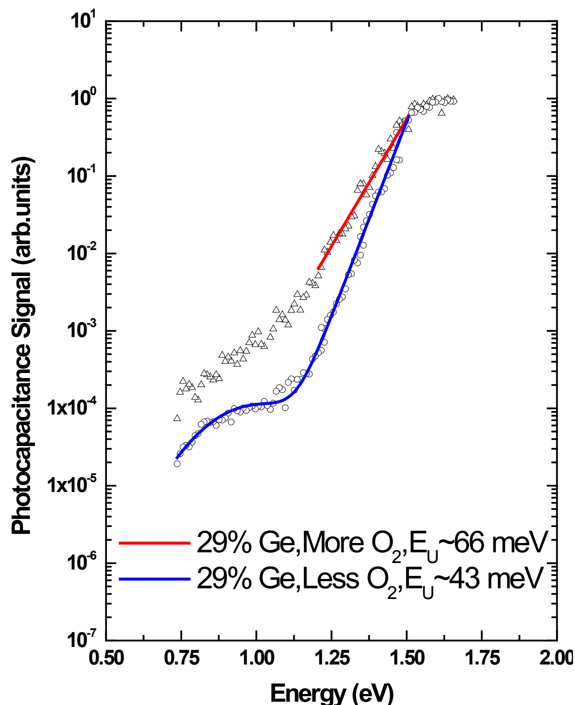

FIG. 20. Comparison of TPC spectra on two 29at.% Ge films, with the later film exhibiting poorer electronic properties evidence by broader bandtail and larger defect band.

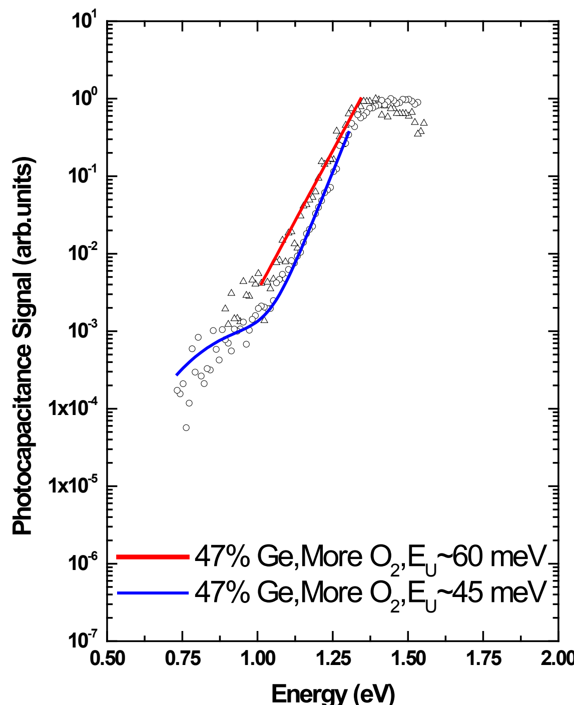

FIG. 21. Comparison of TPC spectra on two 47at.% Ge films, with the later deposited film again exhibiting poorer electronic properties.

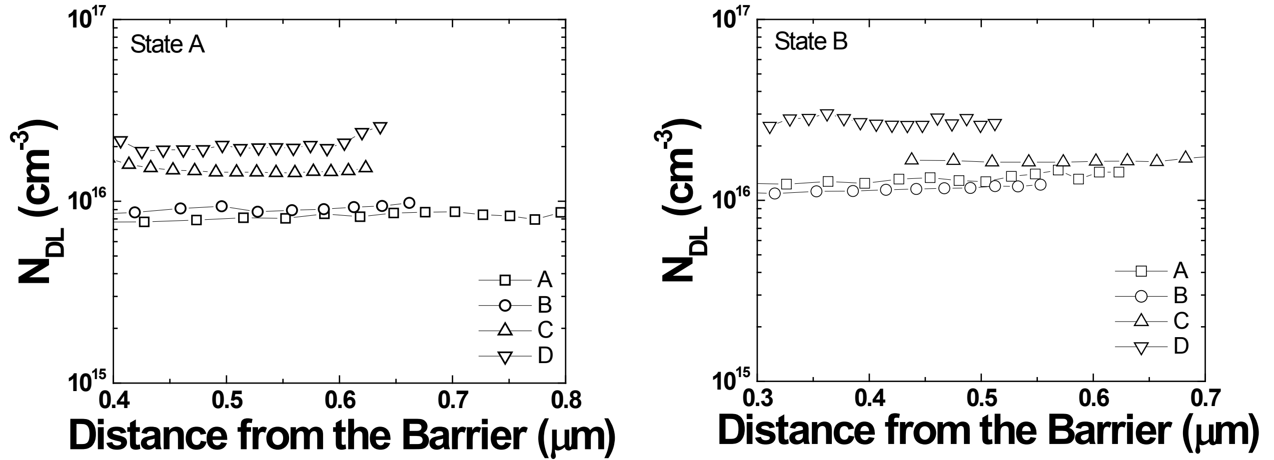

FIG. 22. Spatial profiles of HWCVD a-$Si_{0.70}Ge_{0.30}$:H deep defect densities with different oxygen levels in **(a)** the annealed State A and **(b)** in a light-soaked State B. The oxygen levels for samples A, B, C, and D were determined by SIMS measurements to be 8×10^{18}, 3×10^{19}, 1×10^{20}, and $5\text{x}10^{20}$ cm^{-3}, respectively. These DLC profiles were obtained at 1.1 kHz and 370K.

the level of oxygen contamination to directly find out how it was affecting the electronic properties of these samples. Therefore, series of a-Si,Ge:H alloy samples were deposited using a controlled leak valve to introduce a systematic variation in oxygen level during the HWCVD process. Oxygen levels varied from less than 1 x 10^{19} cm^{-3}, with no intentional air leak, to about 5 x 10^{20} cm^{-3}, when the air-leak was at 0.2 sccm (see Fig. 4 in Section 2.2). All of these a-Si,Ge:H films were deposited simultaneously on stainless steel and p^+ c-Si substrates. More of the details of these samples are described in Section 2.2.

In Fig. 22 we plot the observed spatial profile of deep defect densities as measured by DLCP technique for the four a-Si,Ge:H alloy samples with 30at.% Ge. We see that the deep defect density in the annealed State A increases from a value ~8×10^{15}/cm^3 in sample A (lowest oxygen) to ~2×10^{16}/cm^3 in sample D (highest oxygen). These samples were also examined in a degraded State B produced by light soaking for 100 hours at roughly 1W/cm^2 intensity using a ELH source with a 610nm long pass filter. The deep defect densities of the samples with different oxygen contents, did increase somewhat, although less than a factor of 2 in all cases.

In Fig. 23 we display the TPC spectra in State A of the same series of 30at.% Ge sample grown with no intentional air-leak, the one with the 0.06 sccm air flow, and the one with the 0.2 sccm air flow, all on stainless steel substrates. It appears that the increased oxygen content actually results in films with narrower bandtails. While this was our initial conclusion, further study has indicated that it was not correct. Instead, we have now determined that the oxygen

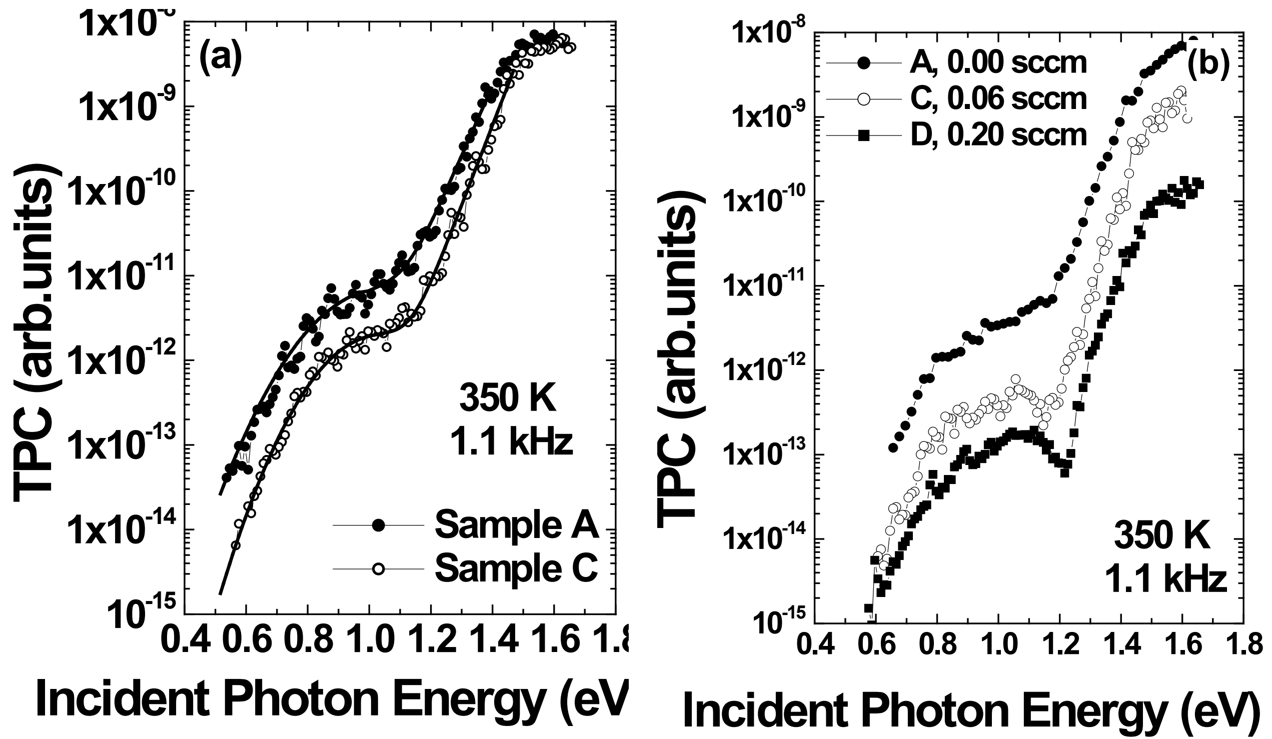

FIG 23. **(a)** TPC spectra for 2 of the HWCVD a-$Si_{0.70}Ge_{0.30}$:H films with different oxygen levels deposited onto stainless steel substrates, and **(b)** Three of the HWCVD a-$Si_{0.70}Ge_{0.30}$:H films deposited onto p^+ c-Si substrates. The latter curves have been vertically offset for display purposes. The Urbach energies for these samples seem to decrease with increasing oxygen levels. However, this is not correct; rather, the apparent narrowing of the bandtails arises from a second defect transition that produces a negative TPC signal centered between 1.3eV and 1.4eV.

contamination is responsible for an additional transition between the valence band and a deep defect level. This results in a negative TPC signal that overlaps the bandtail region thus making it appear to be more narrow. The details of what we have been able to learn about this oxygen related defect then became a primary focus of our work on the HWCVD a-Si,Ge:H alloys carried out for this Subcontract.

5.2 THE OXYGEN RELATED DEFECT IN HWCVD a-Si,Ge:H

In Fig. 24 we display the TPC spectra for the 0 and 0.06 sccm leak rate samples along with transient photocurrent (TPI) spectra taken under the same temperature and rate window. As discussed in Section 3.3., the TPC spectra correspond to the *difference* of electron and hole carriers collected at each photon energy, while the TPI spectra correspond to the *sum* of these. Thus, by examining both types of spectra together one can deduce the fractions of each. The thin solid lines appearing along with these spectra indicate detailed fits that we have carried out to reproduce their salient features.

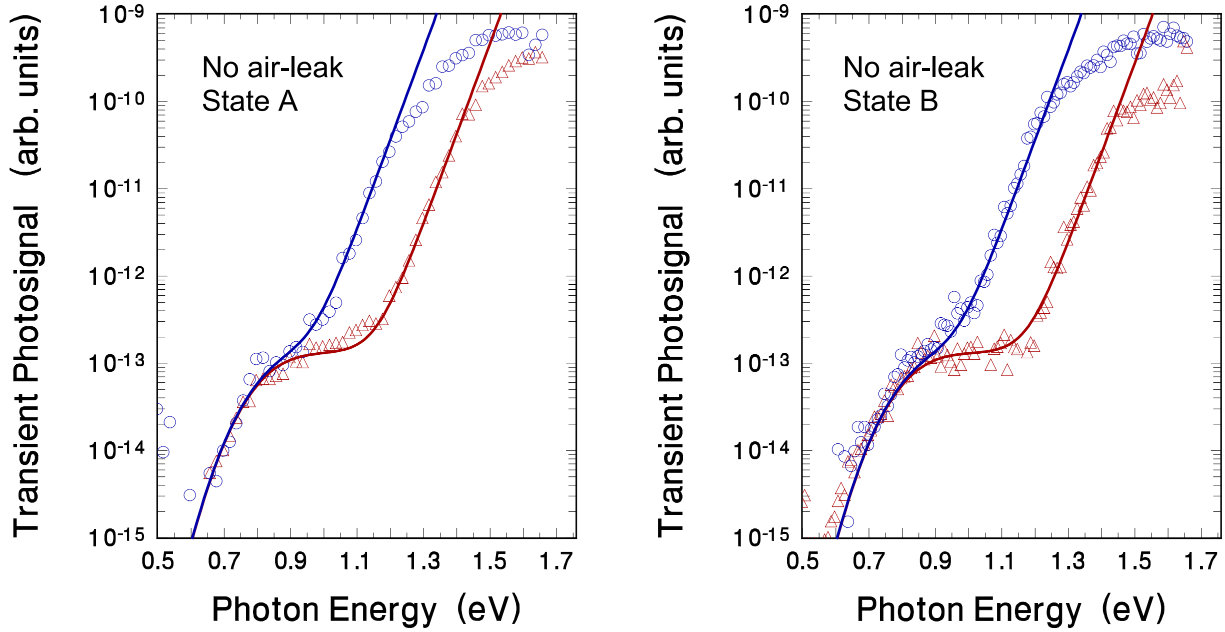

FIG. 24. TPC and TPI spectra before and after light-soaking for the a-$Si_{0.70}Ge_{0.30}$:H film deposited without an intentional air leak. The solid lines represent a fit to these spectra indicating a defect band 0.82 E_V below E_C with a FWHM of 0.17eV, plus an Urbach energy of 45meV.

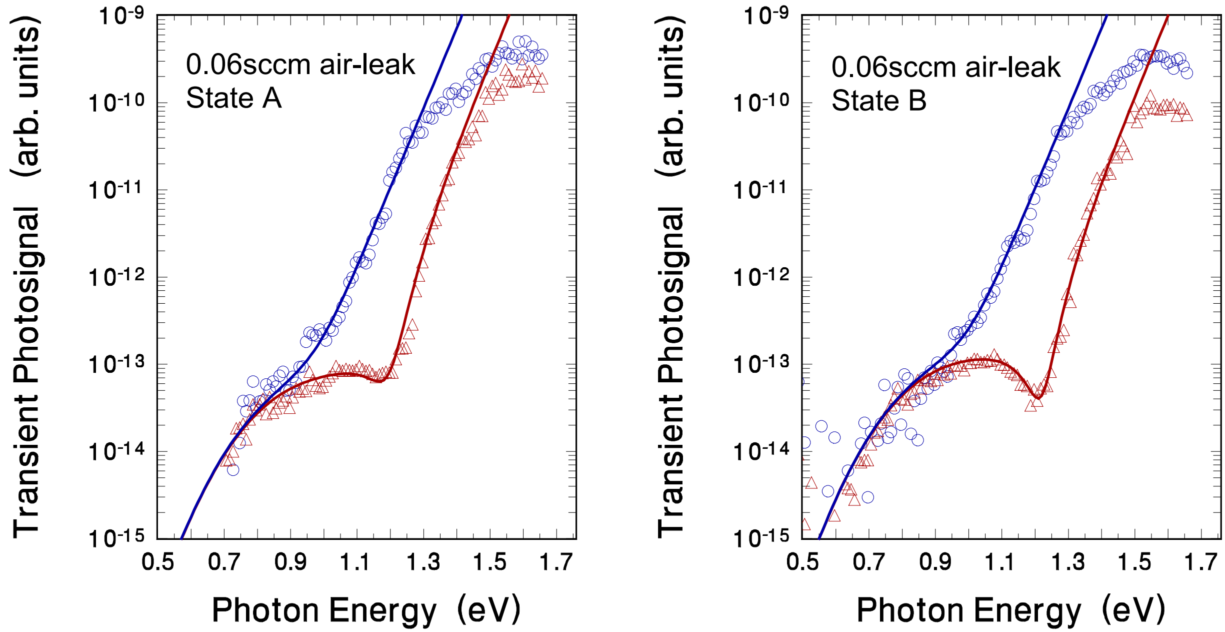

FIG. 25. TPC and TPI spectra before and after light-soaking for the a-$Si_{0.70}Ge_{0.30}$:H film deposited with the 0.06sccm air leak. The fits in this case indicate a defect band 0.85eV below E_C (FWHM = 0.24eV) *plus a second band of defect transitions* at 1.4 eV above E_V.(also with FWHM = 0.24eV). The deduced Urbach energy required to fit *both* the TPC and TPI spectra is now 47meV.

For the sample deposited without an intentional air leak the spectra indicate two specific features: electronic excitation from a gaussian shaped defect band to the conduction band with

an optical energy threshold of 0.82eV (FWHM of 0.17eV), plus a exponential bandtail with an Urbach energy of 45 meV. The ratio of the TPI to TPC signals in the bandtail region indicates the relative collection fractions of holes to electrons to holes. It is 99% for this sample, among the highest ever deduced by this method.

The TPC spectra for the sample with the 0.06sccm air leak appears to exhibit an even narrower bandtail; however, when taken together with the TPI spectrum in Fig. 25 we have now discovered this is *not* the case. Instead, to obtain a good fit to both types of spectra together we must include the effects of an additional defect band that has an optical threshold centered at 1.4eV *from the valence band*. Taken together with an Urbach energy of 47meV as well as a defect band centered 0.85eV below the conduction band, a good fit is obtained to both the TPC and TPI spectra as indicated. In this case the relative collection fraction of holes/electrons is found to be 95%. This is quite consistent with the 47meV value of Urbach energy that we have deduced in our detailed fitting of these spectra.

A light-soaked state of both samples was examined after exposure to 610nm filtered light from an ELH source for 100hours at an intensity of 400mW/cm^2. The role of the additional defect band is even more apparent in the spectra of the light soaked state of the 0.06sccm air-leak sample that is displayed in Fig. 25(b). Here we find that it has a similar or perhaps even a slightly smaller magnitude than for State A. The defect band at $E_C - 0.85$eV, on the other hand, was found to increase, but only by a factor of about 1.5. The same factor increase was found for DLCP data obtained before and after light-soaking this sample. (The Urbach energy used to obtain the fits to the spectra in the light-soaked state was again 47meV.) Somewhat surprisingly the hole/electron collection fraction appears to have *increased* (to above 98%).

For the sample without intentional oxygen contamination we also observed an increase in the hole/electron collection fraction (to 99.4%). We found nearly *no change* in the magnitude of the $E_C - 0.82$eV defect band. The DLCP data also indicated very little change in the midgap defect density after light-soaking for this sample (see Fig. 22).

Figure 26 exhibits a comparison of the TPC spectra for three samples with increasing oxygen levels. We see that the 1.4eV transition is basically absent from the spectrum of the sample with no intentional oxygen incorporation during the HWCVD growth, and increases with as the oxygen level increases. We thus attribute this 2nd defect band with the oxygen impurities present in these a-$Si_{0.7}Ge_{0.3}$:H alloy films. However, this increased oxygen level appears to have only a very minor effect upon the minority carrier collection fraction. For the lowest oxygen sample we deduce an Urbach energy of 45meV, among the lowest ever measured for a a-Si,Ge:H sample in this alloy range. Correspondingly, the relative collection fraction of hole-to electron

was found to be around 97% for that sample. Moreover, as indicated in Figs. 24 and 25, these HWCVD deposited a-Si,Ge:H films appear to be much more stable with respect to light-induced degradation than the highest quality PECVD a-Si,Ge:H samples studied [26] previously by these methods. However, this may partially be because their initial deep defect densities are close to 10^{16} cm^{-3}, compared to the mid 10^{15} cm^{-3} level of those previous PECVD samples.

One interesting remaining issue concerns why the transition into an empty defect band at ~1.4eV from the valence band should be so predominantly negative for the sample with the highest oxygen level. This can only be possible if the electron that is inserted from the valence band remains strongly trapped for the duration of the measurement time window (of roughly 0.4s). We attempted to study the subsequent thermal emission of this trapped electron by recording the TPC spectra for the highest oxygen doped sample over a wider range of temperatures. Three such spectra are shown in Fig. 27 for the 30at.% Ge sample.

In Fig. 28 we display one example photocapacitance spectrum obtained for the 15at.% Ge sample. This sample also exhibits a negative deep defect signal with an optical transition energy that is nearly the same as that of the 30at.% Ge sample. In Fig. 29, we plot the temperature

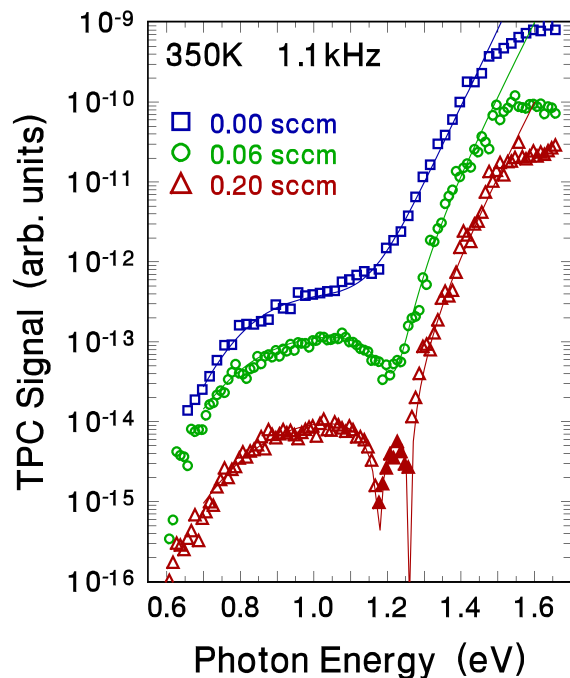

FIG. 26. Photocapacitance spectra for three a-$Si_{0.7}Ge_{0.3}$:H samples with different oxygen levels. The thin solid lines indicate fits obtained in the same manner as those in Figs. 24 and 25. For the sample with highest oxygen content, the TPC signal actually became *negative* (filled triangles) for the region between 1.1 and 1.4eV.

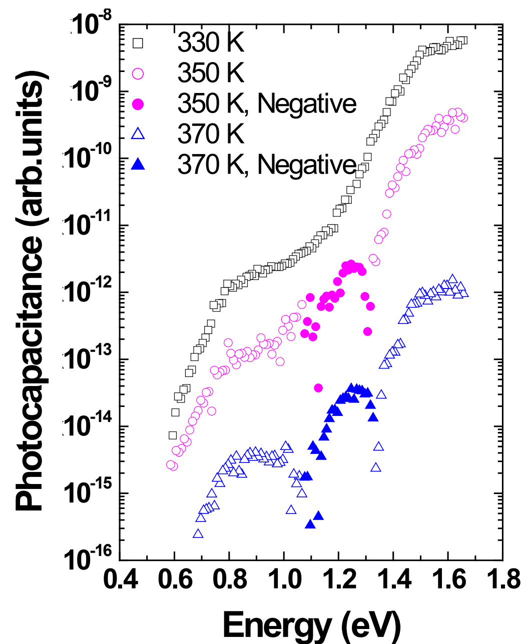

FIG. 27. TPC spectra of 0.2sccm oxygen leak a-$Si_{0.7}Ge_{0.3}$:H sample at 3 temperatures. These spectra were been vertically shifted from each other for greater visibility. Note the relative increase of the negative feature (filled symbols) near 1.2eV at higher temperatures, and the relative decrease in the bandtail signal.

FIG. 28. Photocapacitance (TPC) spectra for a 15at.% Ge sample deposited at NREL using their HWCVD process. This sample was deposited using a 0.2sccm intentional air-leak. The TPC signals in the region near 1.3eV optical energy was again negative for temperatures above about 350K indicating a transition that caused empty defect levels to be filled via an optical transition from the valence band.

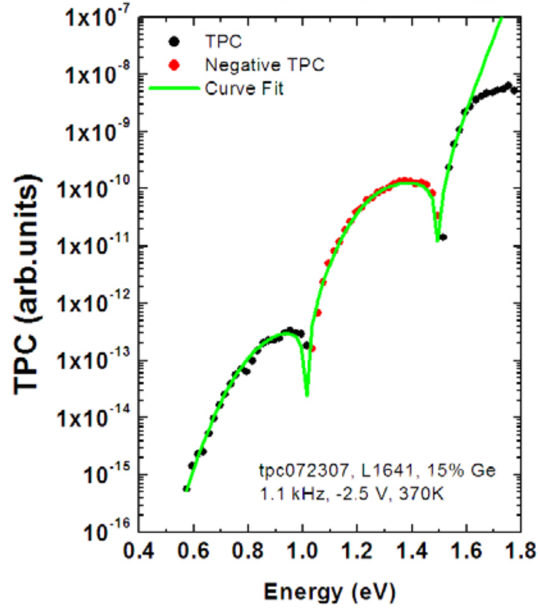

dependence of the TPC signal at a photon energy of 1.2eV for both these samples (to avoid the region where the 1.4eV transition is less obscured by the bandtail signal). Figure 29 indicates a switch in sign near 340K in both cases and that the (negative) contribution due to the oxygen impurity peaks near 365-370K. We believe that, above ~380K, the photocapacitance signal is reduced in magnitude due to the subsequent thermal emission of this optically trapped electron from this defect. Below about 345K the TPC signal for the 30at.% Ge sample increases monotonically to a large positive value. This is due to an increasingly positive contribution from the bandtail due to increasingly poorer hole collection at lower temperatures (see also Fig. 27).

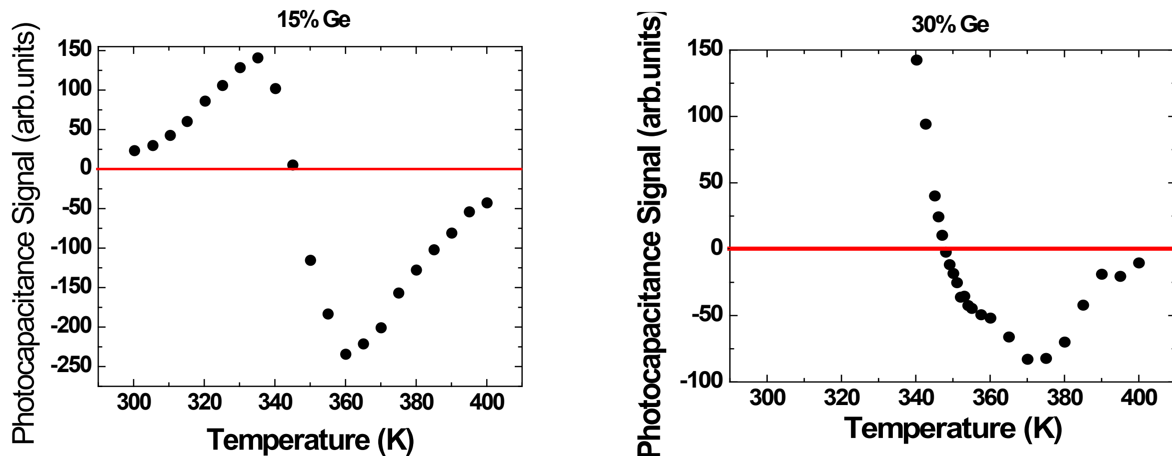

FIG. 29. Detailed temperature dependence of the photocapacitance (TPC) signals near 1.2eV for the highest oxygen contaminated a-Si,Ge:H samples with 15at.% and 30at.% Ge. In both cases the TPC signal in this temperature regime changes sign from positive to negative as the temperature is raised above about 345K. The rapidly increasing positive signal for the 30at. % Ge sample at lower temperatures is mostly due to the increasing contribution of the bandtail signal at lower temperature (due to the decreasing degree of minority carrier collection).

FIG. 30. Photocapacitance signal *vs.* energy at 370K for the 30at.% Ge sample with the 0.2sccm oxygen contamination level on a linear scale at different light intensities. In each case the capacitance signal has been normalized to the photon flux. Therefore the differences in the curves represent a non-linear response to the optical excitation.

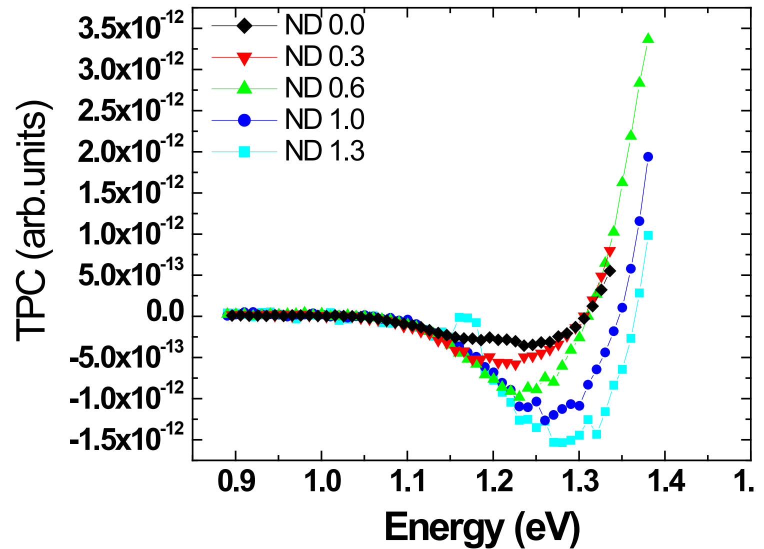

The issue of the bandtail signal obscuring the observation of the 1.4eV transition is less important in the lower Ge sample due to its wider bandgap. Thus, the temperature dependence shown for the 15at.% sample probably gives a better picture of the behavior of the defect response itself for temperatures below 340K.

Based on these experimental results, we hypothesize that the observed oxygen impurity related defect state is associated with a positively charged oxygen donor level, possibly that previously suggested three fold coordinated (O_3^+) type centers in a-Si:H [27- 28, 29,30]. The 1.4eV transition energy from the valence band indicates a center close to the conduction band; however, to account for the observed behavior, it is also necessary that in the O_3^0 state, the trapped electron cannot be thermally emitted into the conduction band very quickly. This clearly requires the presence of a significant thermal barrier to inhibit this.

5.3 DETAILED DYNAMICAL PROPERTIES OF THE OXYGEN RELATED TRANSITION

In Fig. 30 we display the TPC spectra (on a linear scale) at different light intensities for the 30at.% Ge sample at 370K. Since the TPC signals represent a capacitance signal already normalized to the photon flux, any deviations of the curves from each other in Fig. 30 represents a non-linear dependence of the rate of optical induced charge emission with intensity. Therefore, we conclude that optical rate is linear for optical energies near 1.2eV (and below) for neutral density filters of 0.6 and higher, but definitely nonlinear for higher intensity light.

Insight into the nature of this non-linear behavior is obtained by examining the raw capacitance transients themselves following excitation at 1.2eV. These are displayed in Fig. 31 and, indeed, we see a marked change in the nature of the transients when the light intensity is increased beyond a certain level. The nature of the transients at higher intensity shows two

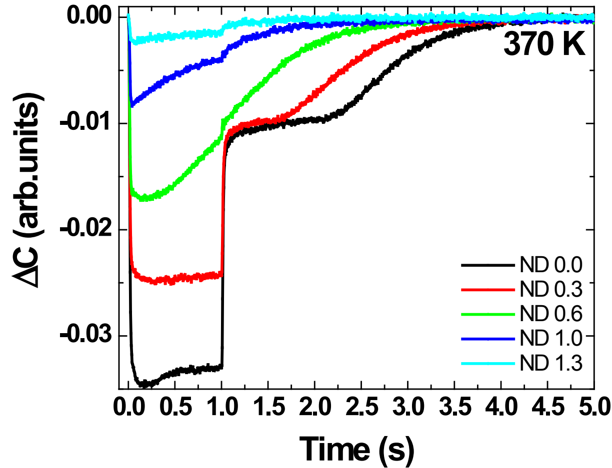

FIG. 31. Capacitance difference signal *vs.* time during (0s to 1s) and after (1s to 5s) excitation using a 1.2eV light pulse at different intensities, all at a temperature of 370K. For higher intensities (neutral density filter below 0.6) a two-stage recovery transient is evident.

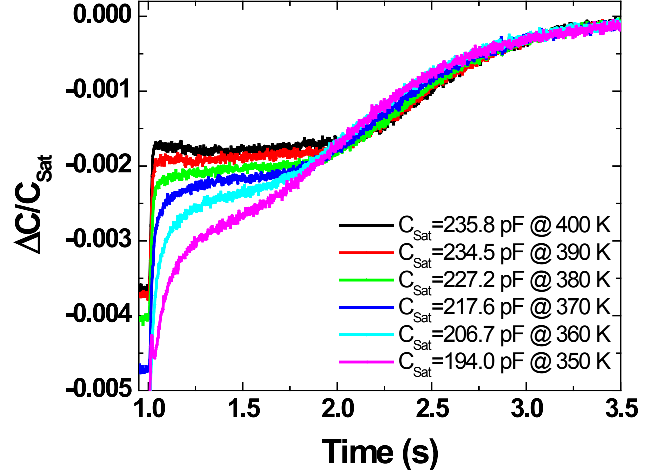

FIG. 32. Transients for the 30at.% Ge sample following a 1s duration 1.2eV light pulse at full intensity (i.e., ND = 0) for six different temperatures. All the transients have been normalized to their asymptotic values at long delay times (C_{sat}) which are listed in the legend.

distinct regimes: An initial fast transient followed by a plateau, then a slower transient. Moreover, it appears that the slower transient was actually present at all light levels but that, as the light intensity was increased beyond a certain level, the duration of the intermediate plateau region simply increased so that the onset of the second transient becomes delayed. The presence of such a plateau region is quite unusual since it seems to indicate that no net charge is leaving the depletion region for quite a considerable time but, after that delay, the remainder of the charge is finally able to leave.

In Fig. 32 we examine the transient behavior at the highest light intensity as a function of temperature. Because the steady-state capacitance itself has a strong temperature dependence, we present these as normalized capacitance transient data, $\Delta C(t)/C_{sat}$. Such normalized capacitance transients are more directly proportional to the change in the charge density within the depletion region. Thus, Fig. 32 indicates that nearly the same amount of charge is being released at each temperature, and that roughly the first half of it comes out in a strongly temperature dependent fashion, while the second half of it comes out (after roughly a 2s delay) in a nearly temperature independent fashion. In Fig. 33(a) we replot the early time dependence from Fig. 32, determine a time constant for each temperature and then, in Fig. 33(b), put these time constants into an Arrhenius plot. This early part of each transient does indeed indicate a thermally activated process with a characteristic energy near 0.56eV.

This is already substantially larger than the 0.3 eV difference between 1.2eV optical excitation energy and the 1.5eV optical gap of the material. However, the Arrhenius plot of Fig.

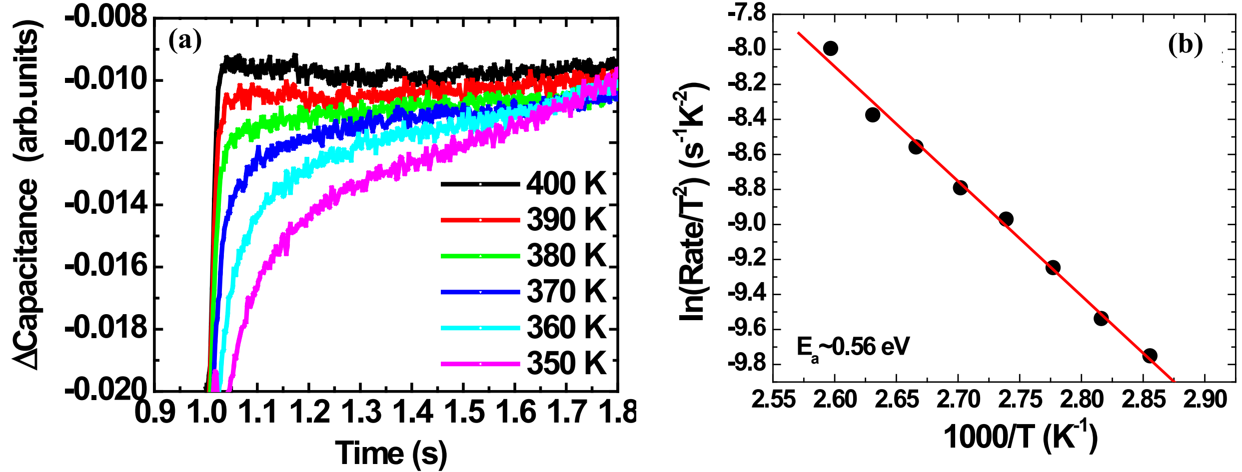

FIG. 33. (a) The early part of the temperature dependence of capacitance recovery following the 1.2eV light exposure for the a-$Si_{0.7}Ge_{0.3}$:H alloy taken from Fig. 32. (b) Arrhenius plot of the emission rates determined from the transients in (a).

33(b) also indicates an anomalously low (~10^9 s^{-1} at 370K) thermal emission prefactor. Therefore, we believe one should estimate the total free energy barrier (ΔF) of the thermal recovery by expressing the emission rate as:

$$\mathrm{R} = \frac{1}{\tau} = \nu \exp\left(-\frac{\Delta F}{k_B T}\right) = \nu \exp\left(\frac{\Delta S}{k_B}\right) \exp\left(-\frac{\Delta H}{k_B T}\right) \qquad (3)$$

Here ΔF=ΔH - TΔS, ΔH is the change of enthalpy (corresponding to the activation energy obtained in an Arrhenius plot) and ΔS is the change of entropy during this electron emission. The factor ν is the usual thermal prefactor which typically varies quadratically with T. If we then assume a more typical thermal emission prefactor of 10^{12} to10^{13} s^{-1} in this temperature regime, then the 1.02×10^9 s^{-1} prefactor at 370K obtained from Fig. 3(b) should be equated with $[10^{12}$ to $10^{13}]\times\exp(\Delta S/k_B)$ s^{-1}. In that case we infer a net change of entropy due to electron emission from this oxygen impurity defect, lying in the range: $\Delta S = -6.9k_B$ to $-9.2k_B$. Therefore, the total free energy barrier at 370K encountered during the thermal emission of captured electron, ΔF = ΔH - TΔS, will lie in the range: 0.78 to 0.85 eV. This is very large compared to the 0.3 eV difference between the optical excitation threshold and the optical band gap.

As a result of this analysis, we conclude that this defect state must experience quite a large energy relaxation after the insertion of photoexcited electrons from the valence band. Indeed, this may be the best documented observation to date of such a substantial relaxation of configurational energy following the change of charged state for a defect level in amorphous silicon or related materials.

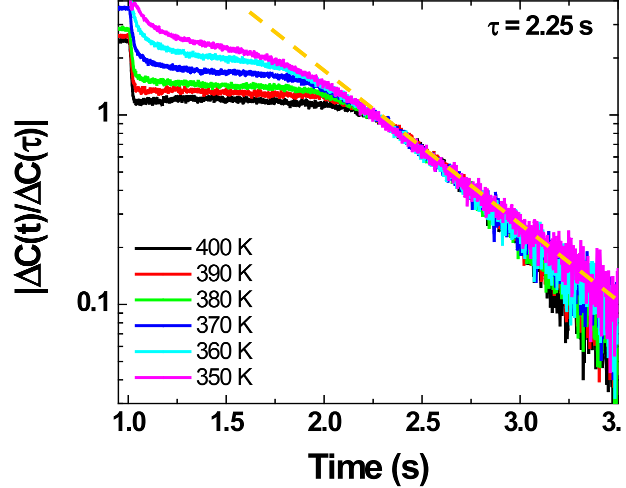

FIG. 34. The second part of the transient recovery following the 1.2eV optical excitation at 370K taken from Fig. 32, but now made into a semilog plot to deduce the (nearly temperature independent) time constant of the second transient. The dotted line indicates that it is roughly 0.65s.

We next turn to an analysis of the second part of the transient shown in Fig. 31. In Fig. 34 we replot these data using logarithmic vertical axis. This seems to indicate that the second electron emission process is also exponential, but with a nearly temperature independent time constant (near 0.6s).

This second emission process with its time delay is quite unusual; thus, we felt it was necessary to verify that its origin was from a bulk rather than a barrier interface related defect. To do this we repeated the 370K measurement of Fig. 35 for a series of different values of reverse bias. These data are displayed in Fig. 35(a). Such detailed data of the bias dependence make it possible to distinguish a bulk from an interfacial defect. That is, the difference in the square of the capacitance before and after the thermal emission of charge from a bulk defect, N_D, should be roughly

$$C^2(\text{before}) - C^2(\text{after}) = \left(\frac{\varepsilon A}{W_{before}}\right)^2 - \left(\frac{\varepsilon A}{W_{after}}\right)^2 \approx (\varepsilon A)^2\left[\frac{q(N+N_D)}{2\varepsilon(-V_A+V_{bi})} - \frac{qN}{2\varepsilon(-V_A+V_{bi})}\right] = \frac{\varepsilon A^2 q}{2} N_D(-V_A+V_{bi})^{-1} \tag{4}$$

where W is the depletion width, V_A is the applied bias, V_{bi} is the built-in potential across the junction, and N represents the other charges in the depletion width that are constant during the emission from the defect. That is, for the emission from a bulk defect the difference in the square of capacitance should be linear in the quantity $(-V_A+V_{bi})^{-1}$ and should go to zero at infinite reverse bias. Figure 35(b) indicates this is in fact the case, also indicating quite a reasonable value for V_{bi}, near 0.7volts.

We verified that the two step transient was present in the 15at.% Ge sample. Data comparing the behavior of the 15at.% and 30at.% Ge samples are displayed in Fig. 36. Clearly, then, this defect seems to be a present as quite a general characteristic of oxygen containing

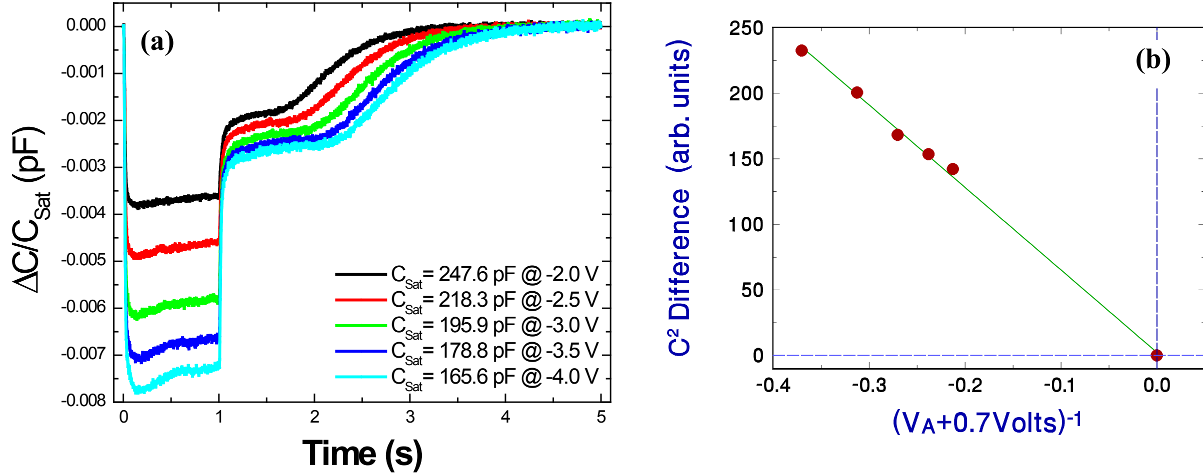

FIG. 35. (a) Capacitance recovery transients for different values of applied bias at 370K following the 1 second 1.2eV light pulse. (b) Linear dependence of the squared capacitance difference predicted by Eq. (2) indicating that the transient originates from a bulk defect level.

a-Si,Ge:H alloys produced by the hot-wire CVD process.

The detailed interpretation of these unusual electron emission transients from the oxygen related defect is still unresolved. Since the onset of the second delayed transient occurs only above a specific photon flux at a given temperature, it seems likely that the optical excitation is able to create a doubly occupied defect state at higher intensities. This second electron is then emitted in a thermally activated fashion in the earlier time regime. The delay before the onset of the emission process for the remaining electron is more difficult to understand. It might indicate a complex configurational rearrangement of the defect's environment, or it might indicate that there is a transport pathway (hopping through neighboring defects?) that takes some time to re-establish itself after the first emission process. There may also be some (as yet unknown) manner in which the edge of the depletion region becomes pinned while charges deeper in the depletion region are being rearranged.

The above results obtained from our studies of these HWCVD a-Si,Ge:H films with controlled oxygen levels supported by this Subcontract have appeared in a series of publications [Pubs. 2,3,4,8,10].

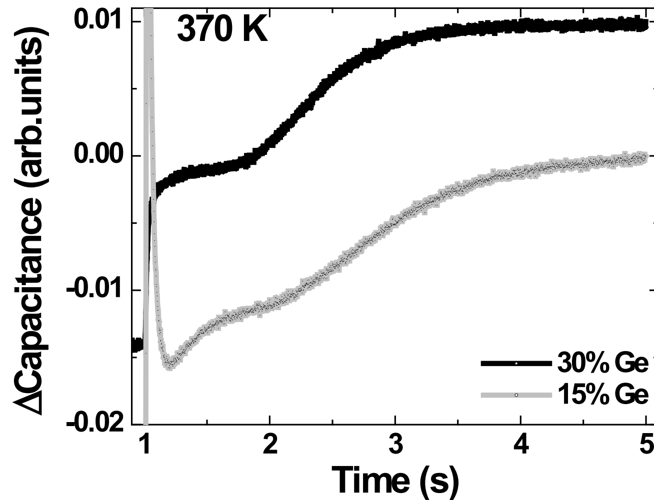

FIG. 36. Dark capacitance recovery after light exposure for 1 sec for both the 15at.% and 30at.% Ge highest oxygen samples. The two stage capacitance recovery is clearly present in both samples. Plots are vertically shifted from each other for clarity.

6.0 STUDIES OF COPPER INDIUM-GALLIUM DISELENIDE SOLAR CELLS

For the CIGS portion of work supported this Subcontract we were to apply our measurement techniques to try to understand differences between the best laboratory cells, and those fabricated using processes better suited for manufacturing. We first present some general background on some reference IEC sample devices to illustrate the types of information we can obtain using our methods on CIGS devices. We then report the results of our studies obtained for three sets of CIGS samples during this Subcontract. First, we will discuss what we learned from studies on a set of high performance NREL CIGS devices obtained in 2005 from Miguel Contreras (see Table VII, Section 2.3.1). Second, what we learned from a later set of NREL CIGS devices that incorporated different types of compositional grading (see Table VIII, Section 2.3.2). Finally we examined two pairs of CIGS cells, each pair simultaneously deposited on two different substrates, yielding matched samples with normal sodium levels and greatly reduced levels (see Table IX, Section 2.3.3).

6.1 BACKGROUND

Some of earliest studies used to examine the electronic properties of the CIGS absorber within a solar cell device employed admittance spectroscopy, typically displayed in the form of capacitance *vs.* temperature and frequency. Quite typical results are shown for a sample from the

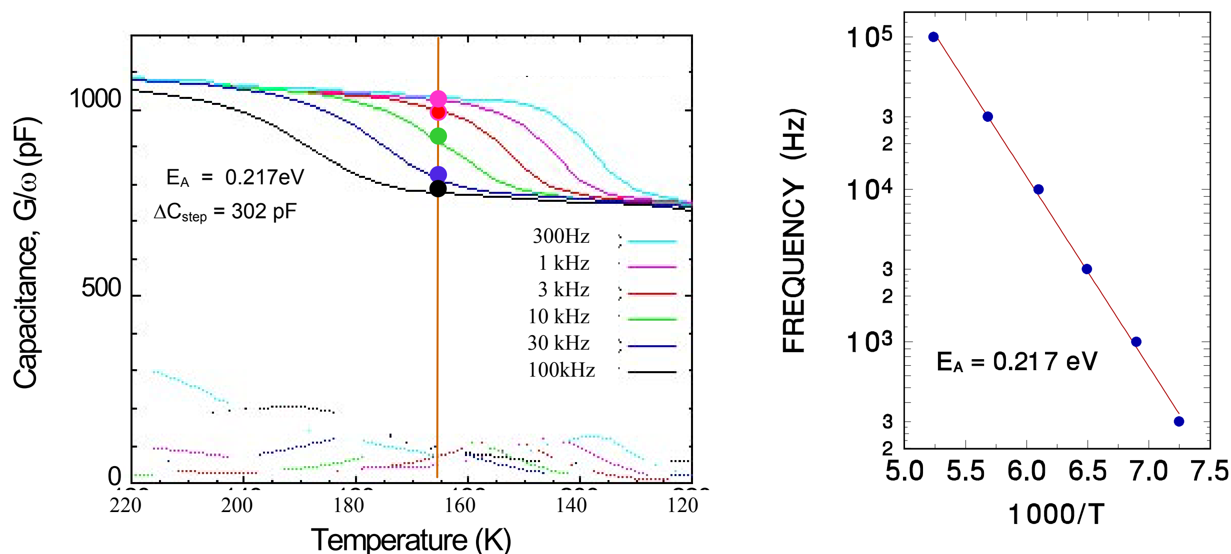

FIG. 37(a). Capacitance *vs.* temperature at 6 measurement frequencies for an IEC CIGS device at zero bias. The distinct temperature step corresponds to a bulk "deep acceptor" defect. The vertical line at 165K and solid circles indicate the conditions under which drive-level capacitance profiling measurements were carried out. These are displayed in Fig. 38.

(b). Arrhenius plot of inflection points at center of step obtained from the capacitance *vs.* temperature curves of Fig. 37(a). The activation energy indicates a majority carrier (hole) trap lying roughly 0.22eV above E_V.

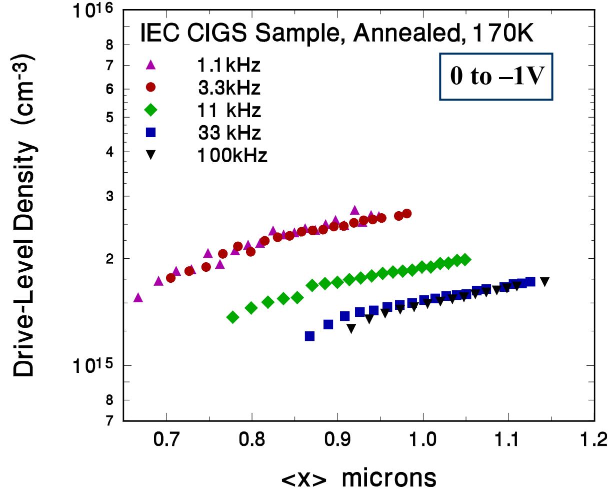

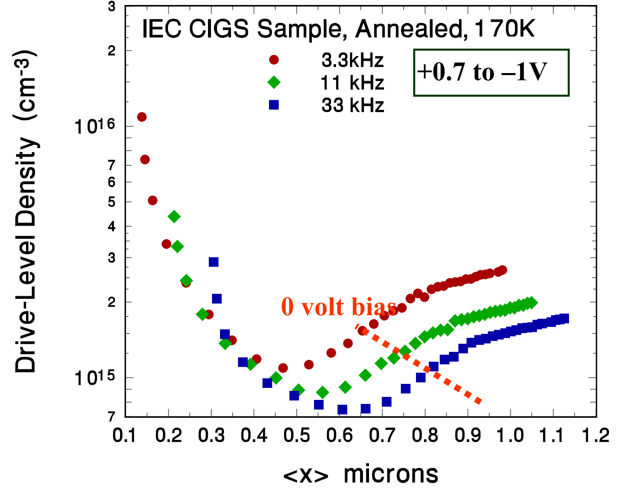

FIG. 38(a). Drive-level capacitance profiles taken near 165K at 5 measurement frequencies. The limiting value at the highest frequencies, near 1.5 x 10^{15} cm^{-3}, indicates the free (hole) carrier density, while the limiting value at the lowest frequencies indicates the *sum* of free carriers plus deep acceptors. This implies a deep acceptor density of roughly 1.2 x $10^{15}$$cm^{-3}$.

(b). Extended DLCP curves obtained by extending the range of DC bias to 0.7volts forward. This allows a region much closer to the barrier interface to be examined compared to Fig. 38(a); specifically, the region to the left of the red dashed line. Clearly, the electronic properties of the CIGS layer vary substantially close to the barrier.

Institute of Energy Conversion, University of Delaware in Fig. 37. These capacitance curves are plotted *vs. descending* temperature to allow a more direct comparison with the capacitance *vs.* log(frequency) plots on the NREL devices shown in the following Section. These curves merge at the lowest temperatures to the depletion width capacitance (εA/W), and then exhibit a step increase before reaching another plateau at the highest temperatures displayed. This step increase arises from the well-known “deep acceptor” band, which usually is the dominant majority carrier trap in the CIGS absorber layer. The step shows a thermally activated signature in an Arrhenius plot. Such behavior has been observed in CIGS devices fabricated from a large number of sources.[31]

Initially there had been some uncertainty whether this admittance step was due to a “bulk” defect distributed throughout the CIGS layer or whether it existed only in the vicinity of the barrier interface.[12] In Fig. 38 we have employed DLCP measurement to spatially profile “energy slices” of the states that are able to respond at the different measurement frequencies at a temperature of 165K. The profiles shown in Fig. 38(a) clearly indicate that the capacitance step in Fig. 37(a) is due to a bulk defect fairly uniformly distributed throughout most of the CIGS layer. In Fig. 38(b) we have extended these DLCP profiles considerably into forward bias to examine the electronic properties much closer to the barrier interface. Here we observe a much more pronounced spatial variation which seems to indicate very different electronic properties in this region of the CIGS layer. Since this is the spatial region that dominates the collection of

photo-generated carriers in the working device, understanding the electronic properties in this region are probably much more important than those in the normally undepleted portion of the CIGS layer.

A multi-investigator collaboration of the NREL Thin-Film Partnership CIGS Team was recently published [31] which concluded in part that there was a strong inverse correlation between the CIGS cell performance and the magnitude of this deep acceptor capacitance step. This conclusion was based upon admittance measurements CIGS devices from six different laboratories. However, these measurements, performed under zero applied bias, probably did not probe the defect properties closest to the barrier interface, such as those revealed at profiling distances smaller than about 0.6μm in Fig. 38(b).

6.2 RESULTS ON NREL CIGS CELLS FROM ADMITTANCE

The results of admittance measurements on the NREL sample devices we examined are generally consistent with the finding that CIGS devices with the highest efficiencies generally do

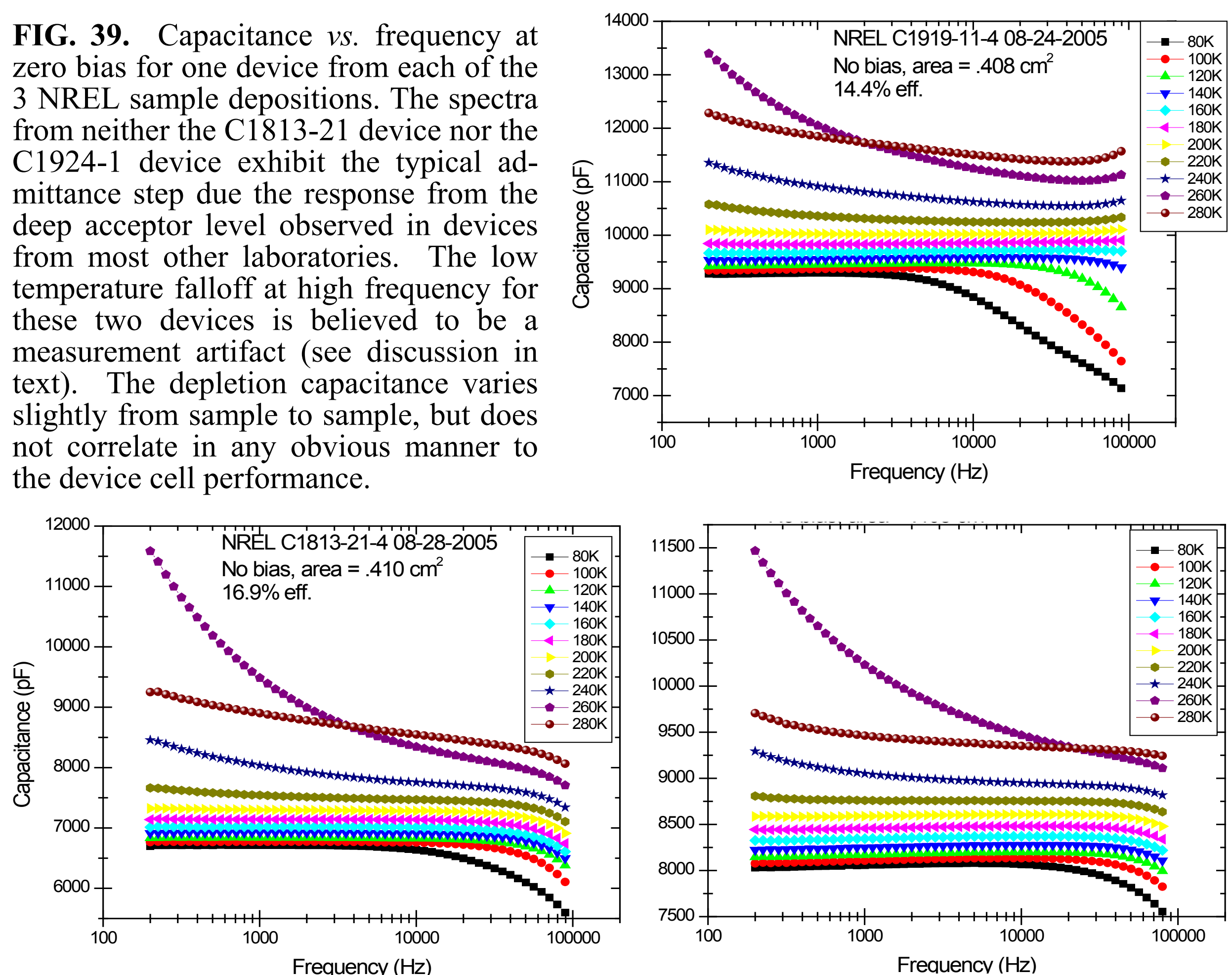

FIG. 39. Capacitance *vs.* frequency at zero bias for one device from each of the 3 NREL sample depositions. The spectra from neither the C1813-21 device nor the C1924-1 device exhibit the typical admittance step due the response from the deep acceptor level observed in devices from most other laboratories. The low temperature falloff at high frequency for these two devices is believed to be a measurement artifact (see discussion in text). The depletion capacitance varies slightly from sample to sample, but does not correlate in any obvious manner to the device cell performance.

not show a deep acceptor step-like feature like those in Fig. 37(a). Representative examples of capacitance *vs.* frequency data for on sample device from each of the three depositions are displayed in Fig. 39. Except possibly for the C1919-11 device, these devices show very little evidence for the admittance step typical of devices from other laboratories. There does appear to be a roll-off at the very highest frequencies for the other 2 devices; however, this does not correspond to the deep acceptor admittance feature that is normally seen. Rather, this roll-off is more likely due either to impedance problems with our current preamplifier or, possibly, due to the limited conductance of the window layer. Both issues arise because these devices have much larger areas than those we have measured in the past. For example, a limited sheet conductance would reduce the effective area of the sample at higher frequencies and low temperatures and produce the type of decrease in capacitance that is observed.

In spite of the lack of such a deep acceptor feature in the admittance spectra of these NREL CIGS devices, and the lack of even any major differences in the junction capacitances, the efficiencies of the devices do vary considerably, as seen in Table VII in Section 2.3.1. However, much more pronounced differences are revealed from our DLCP profiling measurements discussed below.

6.3 RESULTS ON NREL CIGS CELLS FROM CAPACITANCE PROFILING

In Figure 40 we display results of both DLCP and standard CV profiling for these same 3 representative sample devices. The sample bias was varied from 1 volt reverse to +0.4 volts forward and, in all cases, we observe quite a pronounced spatial variation in these profiles. The temperature dependence is quite interesting: For temperatures below about 160K the profiles are nearly temperature independent, and the differences between the DLCP and CV curves are very minor. This changes for the profiles obtained at 200K and above. Indeed, for the 280K profiles, the differences between the DLCP and CV profiles become quite pronounced, with the latter showing a dramatic peak in some cases.

Because of the observed large spatial variations in these profiles, the usual simple interpretation of DLCP in terms of the expression given by Eq. (1) in Section 3.2 may not be very accurate. However, we enhanced some of our numerical modeling programs so that we can extract more detailed information from the types of DLCP and CV profiles shown. This analysis was applied to deduce details of such profiles obtained for the IEC CIGS samples, with and without normal Na levels, discussed in Section 6.4 below.

Although we did not apply this detailed analysis to the profiles displayed in Fig. 40, we can make some general conclusions. First of all, the large CV profile densities at high temperature

are almost certainly due to very deep defects near the barrier interface even though they seem to at profile "distances" that are at a considerable distance from the barrier junction. (This aspect

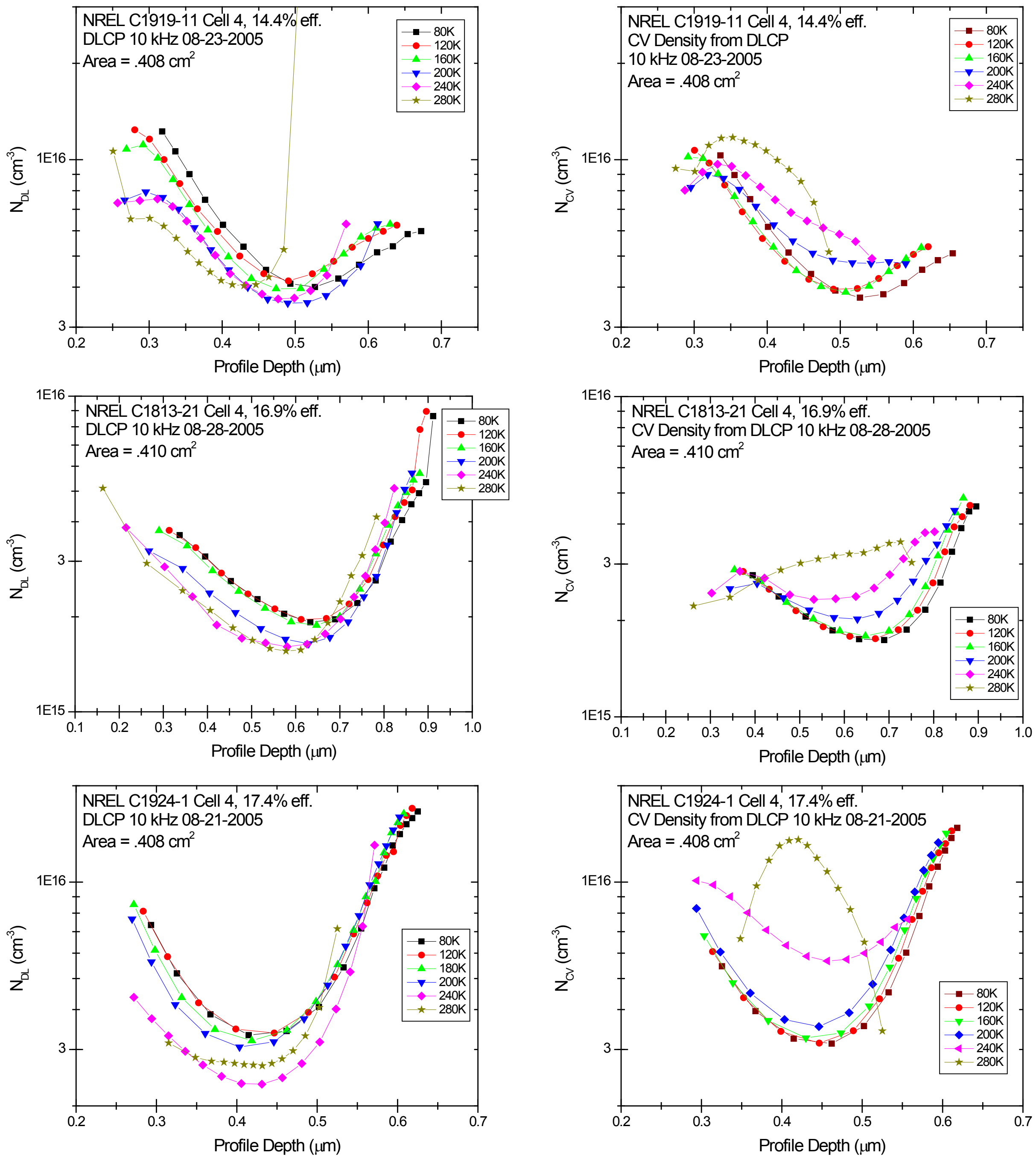

FIG. 40. Drive-level capacitance profiles (DLCP) and CV profiles for representative NREL devices over a broad range of temperatures. These data were taken using DC biases that varied from –1V to +0.4V, in 0.1V increments. Note the strong spatial variation in these profiles in all cases. Also note the similarity between the DLCP and CV profiles for temperatures of 160K and below, but the marked differences for the highest temperatures employed.

of such CV profiles is discussed in detail in Section 6.4.) A clearer picture of the distribution of these deep, near interface states could be deduced from more detailed numerical modeling analysis. Since this is very time consuming and has not been carried out for these samples, we will restrict our remaining discussion to the DLCP results.

Clearly, the appearance of the DLCP profiles is qualitatively different for the different representative samples. For the C1919 (lowest performance) device, the DLCP profile is high in the region near the barrier interface (obtained under forward bias so that this region lies in the high field region under normal operation), and relatively low at larger distances from the barrier (this is the region that lies outside the depletion region in nearly zero field). For the other two, higher performance devices the DLCP density is relatively lower in the normally depleted region close to the barrier, and relatively higher in the zero-field region at larger distances.

To get a better idea of how our DLCP results might be correlated with the device performance, we have plotted in Figure 41 how the device efficiencies vary with the DLCP densities in the normally depleted region of the device closer to the barrier interface [Fig. 41(a)] and also with the DLCP density in the normally zero-field region of the absorber farther away from the barrier interface [Fig. 41(b)]. From Fig. 41(a) we see that, for the 5 devices from two of the depositions, there appears to be quite a good inverse correlation between the cell efficiencies and the DLCP densities close to the barrier interface. It is thus tempting to connect the larger DLCP densities in the depletion region of these devices with a larger concentration of recombination centers that lower the fill factor, and hence the efficiencies. On the other hand, the cells from the third, C1924-1, deposition do not follow this trend. However, we believe that

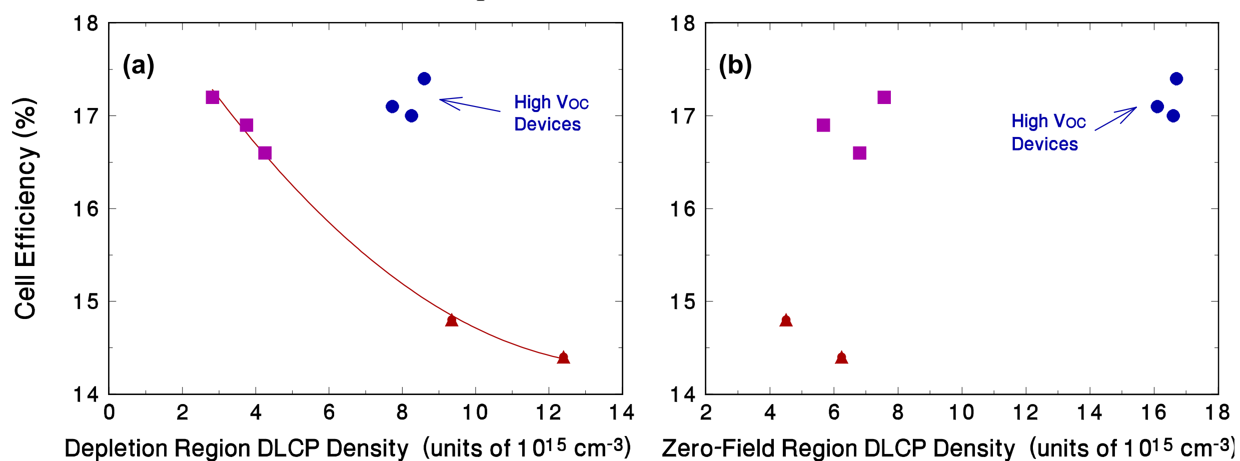

FIG. 41. Correlation of NREL device efficiencies with the DLCP determined densities in the: **(a)** depletion region near the barrier interface, and **(b)** the zero field region of the absorber farther from the barrier interface. The symbols are used in the same manner as in Figs. 5 and 6; namely: ▲ for the C1919 devices, ■ for the C1813 devices, and ● for the C1924 devices. These latter devices were found to have significantly higher values of V_{OC} than the others, and are so labeled.

this might be the result of our inaccurate interpretation of these DLCP profiles since, for the C1924 devices (see Fig. 40), they exhibit the largest spatial variations and thus may be less likely to reflect the true spatial distributions in the electronic properties. Indeed, we note that some of our recent modeling has indicated that the type of large upturn in the DLCP profiles that are exhibited for the C1924 devices at forward bias probably reflect characteristics of the barrier interface itself, rather than defects within the absorber. In contrast, the DLCP curves for the C1919 and C1813 devices appear show signs of flattening out at small profile distances. In some of our attempts to model similar kinds profiles in more detail, we have found that they usually reflect the actual defect densities within the absorber layer close to the barrier interface.

Fig. 41(b) indicates that the high V_{OC} devices are also distinctive in displaying much higher DLCP densities in the zero-field region outside the depleted part of the absorber. This is undoubtedly beneficial for the device performance for two reasons: (1) It means that the hole carrier density is higher in this region, leading to a lower resistivity within the part of the absorber less active in power generation, and (2) The higher DLCP density reflects a hole carrier density that is higher by a factor of 2.5 to 4 times that of the five less efficient devices. This means that the hole Fermi level near the back contact is probably 25-35 meV closer to E_V, and this will be reflected in a higher value of V_{OC}. We believe that this could account for about half of the difference in V_{OC} for the C1924-1 devices compared to the other devices. The remainder of the difference in V_{OC}, we believe, likely comes from differences in the composition profiles of the C1924-1 devices.

6.4 STUDY OF NREL CIGS CELLS WITH VARYING COMPOSITIONAL PROFILING

More recently we began to apply our junction capacitance methods to investigate the effects of Ga grading on a set of four $CuIn_{1-x}Ga_xSe_2$ (CIGS) sample devices fabricated by Miguel Contreras at the National Renewable Energy Laboratory (NREL). These samples were provided to Nanosolar as a reference set of devices. Jeroen van Duren at Nanosolar forwarded a portion of each one to my laboratory by for detailed study using our techniques.

One device was deposited with a uniform Ga depth profile (x=0.30), two were deposited so that the Ga fraction varied monotonically from near x=0.9 at the Mo back contact to either x=0.15 or x=0.25 at the junction interface, and the last device utilized a compositional variation close to NREL's optimal “v-shaped” bandgap grading scheme. Following deposition, SIMS measurements were carried out at NREL to provide a detailed spatial map of the Ga/(Ga+In) ratios in the CIGS absorbers. These profiles for the three compositionally graded devices were displayed in Fig. 8 in Section 2.3.2 and the device performance parameters were listed in Table VIII.

Perhaps the most revealing effects of Ga grading were obtained from our transient photocapacitance (TPC) and photocurrent (TPI) spectra. These measurements provided a spectral map of the optically induced release of carriers for photon energies from 0.6eV to 2eV. Comparing the two types of spectra enables one to distinguish majority from minority carrier processes. We also attempted to obtain additional spatial information by varying the applied DC bias to weight the spectral response to different regions relative to the barrier junction. The edge of the depletion region under different (steady-state) DC biases were estimated by the high frequency junction capacitance values and are indicated on the spatial profile maps shown in Fig. 8 in Section 2.3.2. However, the TPC and TPI measurements also involve the periodic application of voltage filling pulses (of 0.5 volts in the forward direction in each case). This causes the depletion widths to actually extend somewhat farther from the barrier junction than under constant DC bias. Thus, we are really sampling regions farther from the junction than the positions indicated in Fig. 8.

In Figs. 42, 43, and 44 we display pairs of TPI and TPC spectra for 3 of the samples: the one with the uniform spatial profile, one of the monotonically profiled samples (A), and the v-shaped compositionally profiled sample, respectively. In all cases these spectra clearly identified the gap energy of the alloy composition nearest the barrier junction for each sample (1.0eV to 1.2eV depending on the sample). Very narrow bandtails (varying from 13 to 23meV) were observed indicating very low structural disorder.

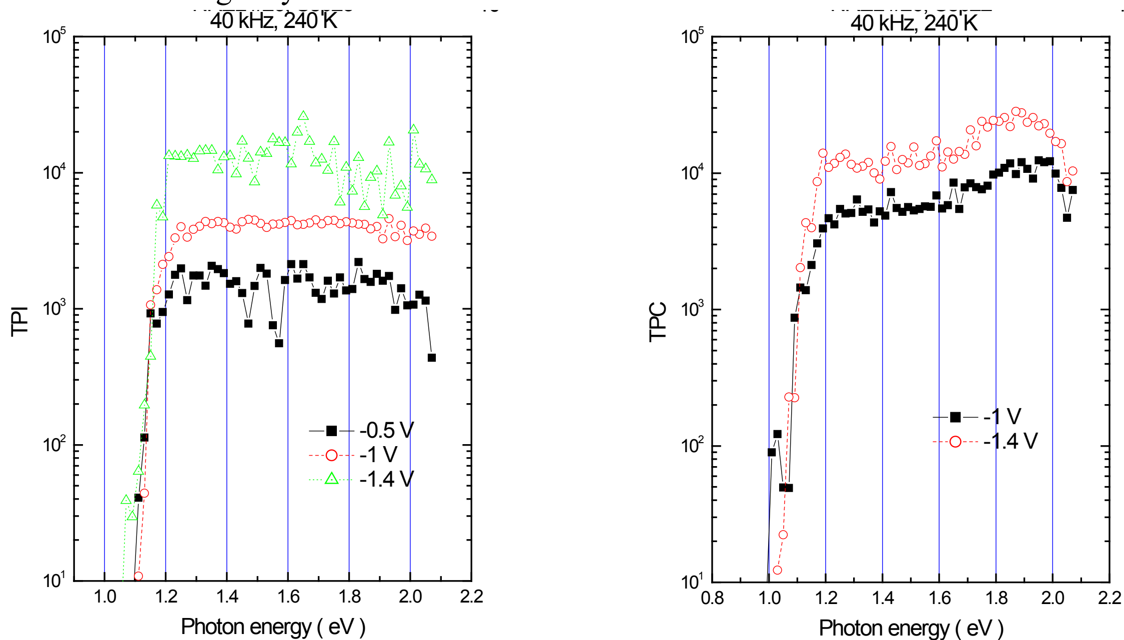

FIG. 42. Transient photocurrent (TPI) and transient photocapacitance (TPC) spectra obtained for the CIGS sample device with uniform compositional grading at 240K at several values of reverse bias. Above the 1.2eV bandgap these spectra exhibit a fairly constant spectral response.

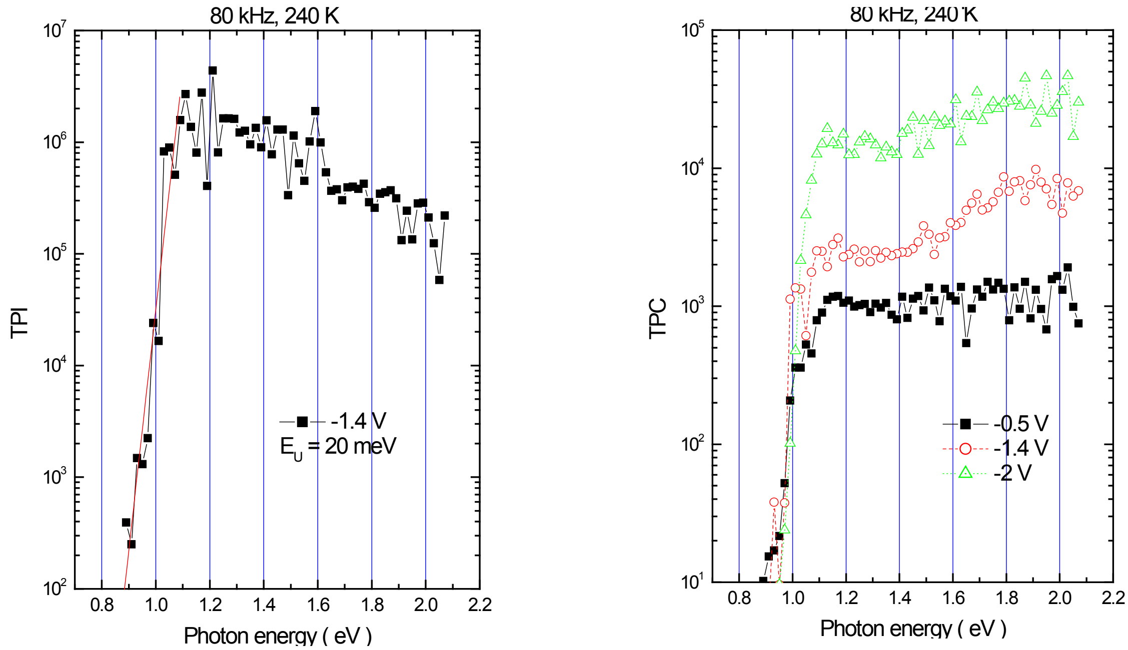

FIG. 43. Transient photocurrent (TPI) and transient photocapacitance (TPC) spectra obtained for the CIGS sample device with an increasing gallium fraction moving away from the junction (monotonic B). Measurements were again made at 240K for several values of reverse bias. Note the larger variation with photon energy of the spectral response compared to the uniform case.

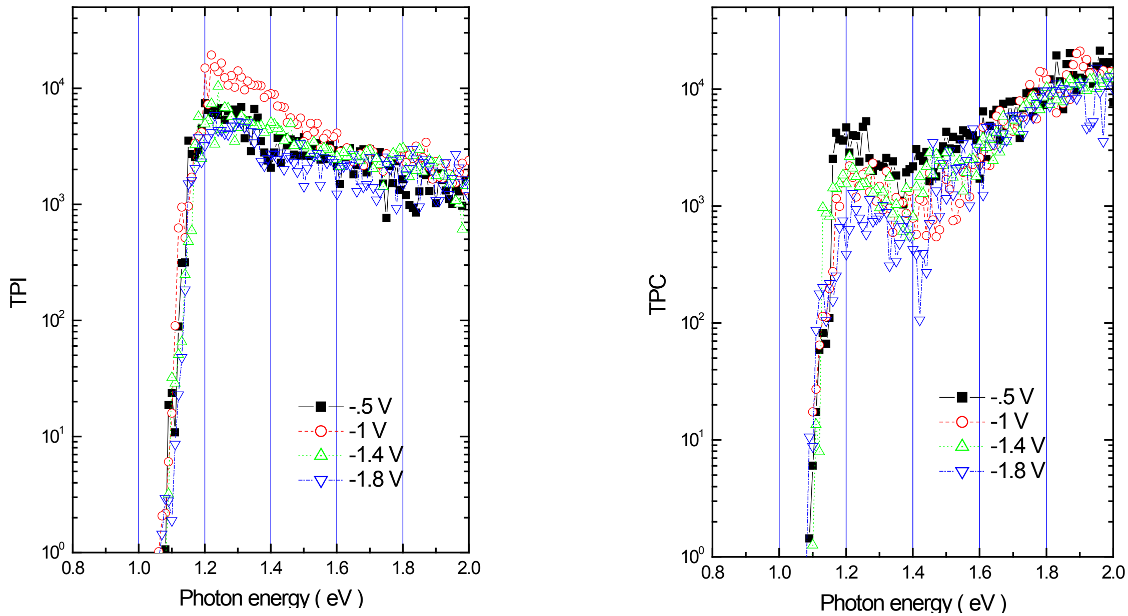

FIG. 44. TPI and TPC spectra for the sample device with a "V-shaped" Ga grading profile at 240K and different DC bias. Here the variation with photon energy above the bandgap is even more pronounced and reflects a substantial increase in minority carrier collection.

The TPI spectra for photon energies in Fig. 42(a) above the bandgap energy of 1.2eV is nearly constant in energy. This indeed reflects the spatial uniformity of the composition for that sample. The TPC spectra in Fig. 42(b) are also reasonably constant above 1.2eV, although they do increase by roughly a factor of 2 between 1.6eV and 1.9eV. The reason for this small increase is not yet clear. The fact that the TPI and TPC spectra exhibit slightly different spectral dependences can arise either because of varying degrees of minority *vs.* majority carrier collection *vs*. optical energy, or because the two measurements methods have different spatial sensitivities (majority carrier collection makes its largest contribution to the TPI signal near the barrier junction, but for TPC this contributes more strongly near the edge of the depletion region). In any case, the spectral variation above 1.2eV is not large.

The TPI spectra for both the samples with monotonically increasing bandgaps *vs.* distance from the junction are quite different, as illustrated in Fig. 43(a). Here we observe a maximum response at the bandgap corresponding to the alloy at the junction, following by a monotonically decreasing signal as the optical energy is increased further. This coincides with a slightly *increasing* TPC response for photon energies above 1.5eV as shown in Fig. 43(b). The latter partly reflects the increasing bandgap; however, the variation in the TPC/TPI ratio with photon energy probably also reflects the increased minority carrier (electron) collection in these samples. This agrees with the general understanding of how compositional grading improves overall cell performance.

Evidence for increased minority carrier collection is even stronger in the sample device incorporating the v-shaped Ga-grading, whose TPI and TPC spectra are displayed in Fig. 44. The types of variations of these signals with photon energy exhibited in Fig. 43 are now significantly enhanced, particularly for photon energies 1.2 to 1.4eV. These spectra also exhibit a quite complex temperature dependent behavior whose details are still being analyzed. However, we believe that they can potentially provide a very complete picture of how compositional grading affects the minority collection in CIGS devices.

We also examined the spatial profiles of the free hole carrier densities and deep acceptor concentrations using drive-level capacitance profiling (DLCP). Results for the sample with the uniform compositional profile, a monotonically profiled sample, and the v-shaped compositionally profiled sample are displayed in Fig. 45. The lower temperature profiles reflect a free carrier density that is indeed uniform in the first case. However, the latter two instances display a marked *decrease* with distance from the barrier junction; that is, as the Ga fraction is increased. At the same time, the higher temperature profiles *increase* with distance. For the compositionally uniform sample this increase was unexpected since previously studied CIGS sample devices with uniform Ga fractions from IEC Delaware displayed more uniform DLCP

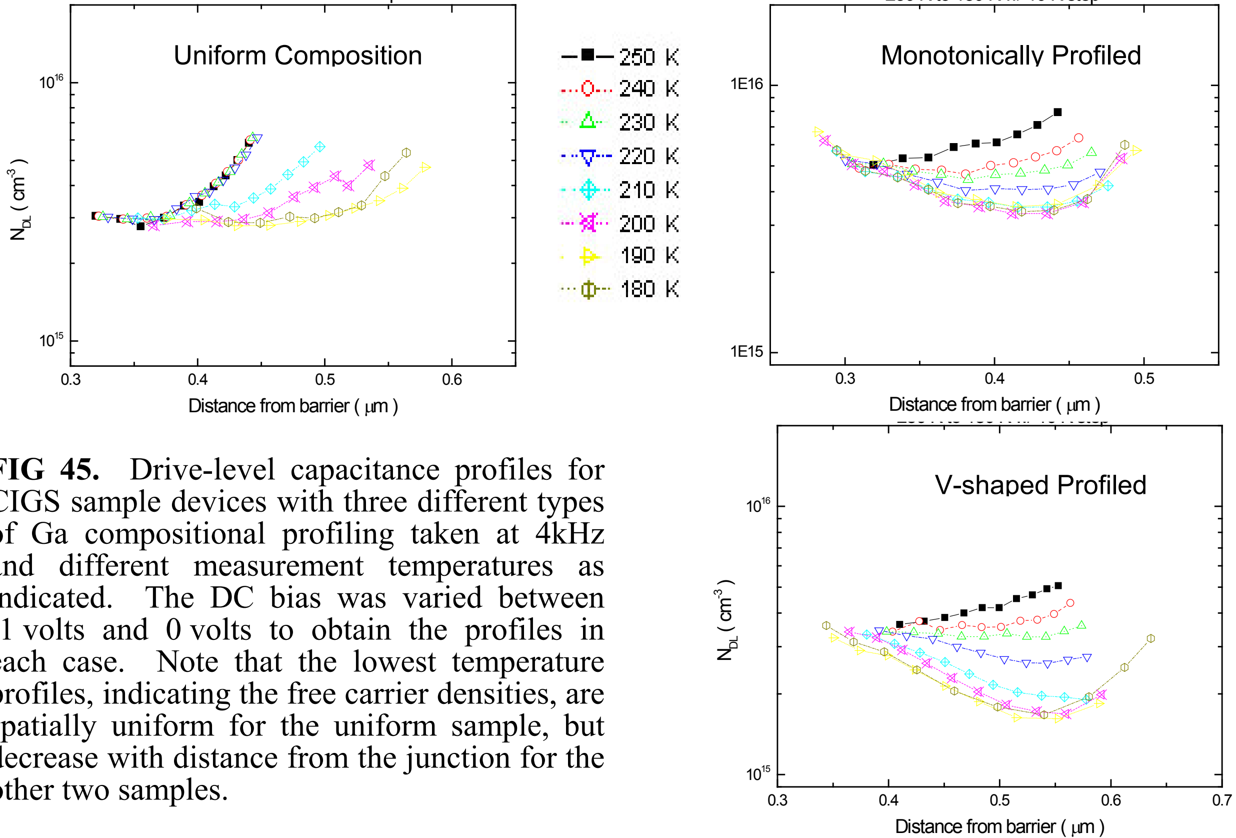

FIG 45. Drive-level capacitance profiles for CIGS sample devices with three different types of Ga compositional profiling taken at 4kHz and different measurement temperatures as indicated. The DC bias was varied between -1 volts and 0 volts to obtain the profiles in each case. Note that the lowest temperature profiles, indicating the free carrier densities, are spatially uniform for the uniform sample, but decrease with distance from the junction for the other two samples.

profiles at higher temperature. However, in the compositionally varying samples this behavior may indicate an actual trend of decreasing free carriers and increasing deep acceptors with increasing Ga alloying. An alternate but intriguing second possibility is that it may be related to the behavior my laboratory has documented in the CIGS alloys under bias stress; namely, that there appears to be a metastable conversion of shallow acceptors into deep acceptors. In the case of compositionally profiled samples an effect similar to bias stressing may be occurring due to the variation in the energy gap which acts as an applied electric pseudo-field. Further studies will hopefully be able to examine this possibility in detail.

The above work on these compositional profiled CGIS films was recently presented at the 2009 Materials Research Society Spring Meeting [Publication 12].

6.5 THE ROLE OF SODIUM IN CIGS SOLAR CELLS

The addition of Na to the CIGS absorber layer is a commonly followed procedure, boosting the efficiency by up to 50% primarily through a sizeable increase in the open-circuit voltage (V_{oc}) and the fill factor (FF). Although the positive role of Na is well known, there is an ongoing debate as to the exact mechanism of the beneficial effect of Na, with much of the debate centering around where in the cell the Na has its effect, as discussed in Section 2.3.3. To gain

some new insights into the role of Na in CIGS films, two pairs of matched baseline and reduced Na samples were provided to us by the Institute of Energy Conversion. In each case one sample utilized the usual soda-lime glass substrate while the companion sample was deposited simultaneously on a substrate which substantially eliminated sodium from the resultant CIGS film. The presence of Na resulted in the well known beneficial effects on the solar cells: An increase of 130mV (or roughly 25%) in V_{oc}, with corresponding increases in fill factor and efficiency (by more than 40%). However, there was virtually no effect on the short circuit current (see Table IX in Section 2.3.3).

6.5.1. COMPARISON OF ELECTRONIC PROPERTIES

Drive-level capacitance profiles are displayed for both pairs of the CIGS samples with and

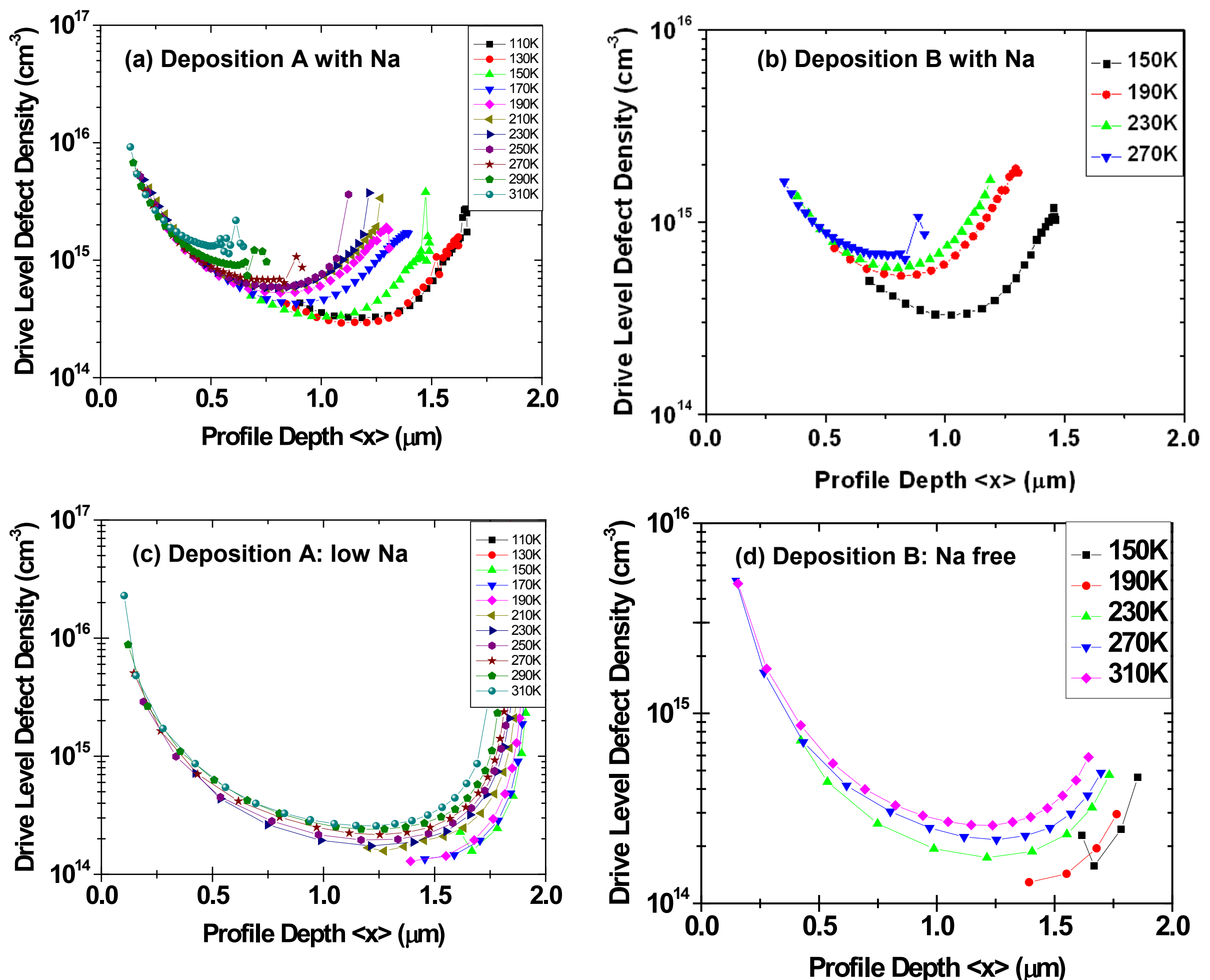

FIG. 46. DLC Profiles for (a) and (b) normal Na containing CIGS cells, (c) a reduced Na sample resulting from deposition onto a glass substrate with an SiO_2 Na diffusion barrier, and (d) a Na free cell resulting from deposition onto a Ti foil substrate. These profiles were obtained at 10 kHz at the temperatures indicated with an applied dc biases from 1.0 V reverse to 0.3 V forward. Note that while the higher Na samples appear to exhibit a larger deep defect response, those cells are 50% more efficient than the reduced Na cells.

without Na in Fig. 46. These profiles show similar overall shapes but more spatial variation in the samples containing Na. The samples with Na exhibit a defect response activating between 130 K and 190 K that is absent in the reduced Na samples. Note that the corresponding profiles are nearly identical for the two depositions (as are the cell performance parameters listed in Table IX). Without any prior knowledge of cell performance, one would predict that the more spatially uniform, reduced Na samples would be more efficient. Exactly the opposite is the case. Thus, this indicates that something not visible in the DLC profiles is having a dramatically harmful effect on the performance of the low Na cells.

These profiles indicate free carrier densities of 3×10^{14} cm^{-3} for the Na containing samples and less than 2×10^{14} cm^{-3} for the samples with little or no Na. From the higher temperature profiles we infer a deep acceptor density of ~1×10^{15} cm^{-3} in the normal Na samples. The reduced Na samples do not show this type of defect, instead it increases only slightly with temperature to a maximum value of ~3×10^{14} cm^{-3}. The abrupt increase in the DLC profiles near the junction ($\langle x \rangle = 0$) may reflect a significant defect density near the junction, however we are not certain whether the DLCP can provide an accurate measurement of the defect density in this region. We thus generally choose to use the more spatially uniform region of the profiles to estimate the free carrier and defect densities.

In Fig. 47 we compare the TPC spectra for the Na and reduced Na samples from deposition A. The spectra have been aligned above the 1.2 eV gap energy to enable a better comparison. The spectra are generally quite similar, and the thin solid lines indicate fits in which we have assumed a gaussian defect band and an exponential band tail. The sample containing Na exhibits an Urbach energy of 17 meV plus a gaussian defect band centered at 0.75 eV above E_V with a FWHM near 120 meV. The Urbach energy for the low Na sample is larger, 23 meV, and the gaussian defect band appears centered at 0.70 eV with a much smaller width, about 50 meV. The narrower bandtail for the sample containing Na suggests a higher degree of crystalline order within the CIGS absorber[32].

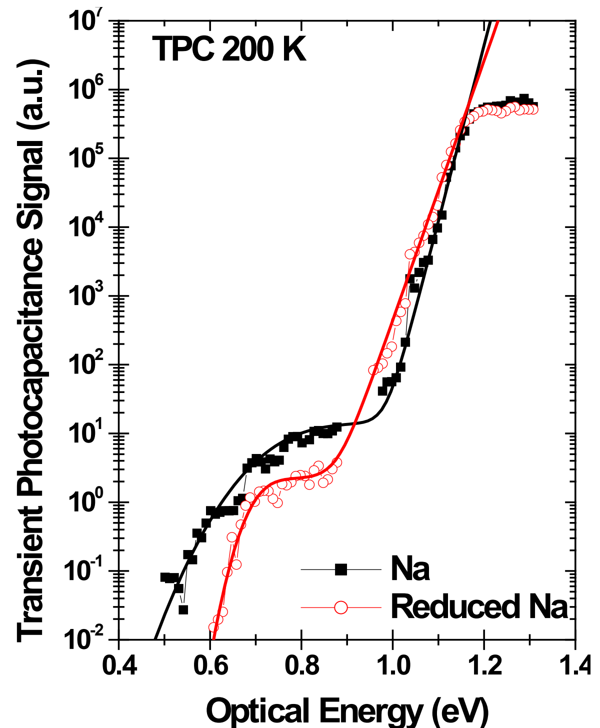

FIG. 47. TPC Spectra of the two CIGS samples from deposition A with normal and reduced Na. The reduced Na sample spectrum exhibits a broader bandtail, indicating a higher level of disorder.

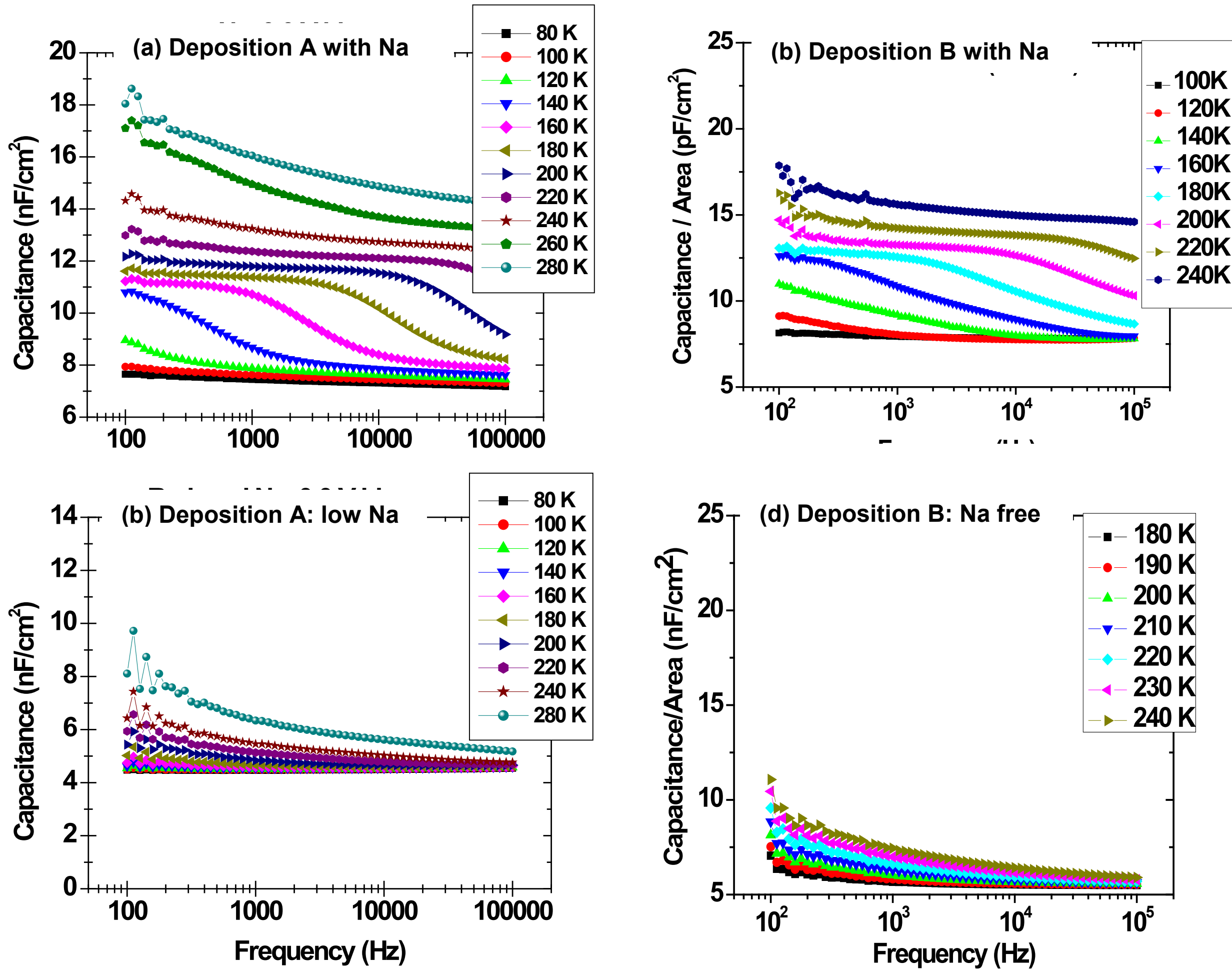

FIG. 48. Admittance spectra under 0 volt applied bias for (a) & (b) the Na containing samples, and (c) & (d) the reduced Na samples. The latter only show a step under an applied forward bias (see Fig. 50) or after light soaking (see Fig. 49).

Admittance spectra are displayed in Fig. 48 for all four of these samples under 0V applied bias, for frequencies between 100 Hz and 100 kHz and a wide temperature range. The behavior for both depositions is nearly identical: there is a very distinct activated step in the samples with Na, but no such clear feature in the reduced Na samples. These results are consistent with the DLCP data of Fig. 46, also indicating a very low deep acceptor response for the samples with little or no Na. The step in the Na containing samples has an activation energy near 270 meV as determined by an Arrhenius plot, consistent with many previous admittance measurements of CIGS materials. It is worth pointing out that many researchers have associated such a larger step in admittance with poorer device performance. However, in this case, the exact opposite appears to be true.

Admittance spectra were then obtained over the same frequency ranges, but with an applied bias. Under reverse bias of 0.5 V, there were no changes in the spectra. The reduced Na

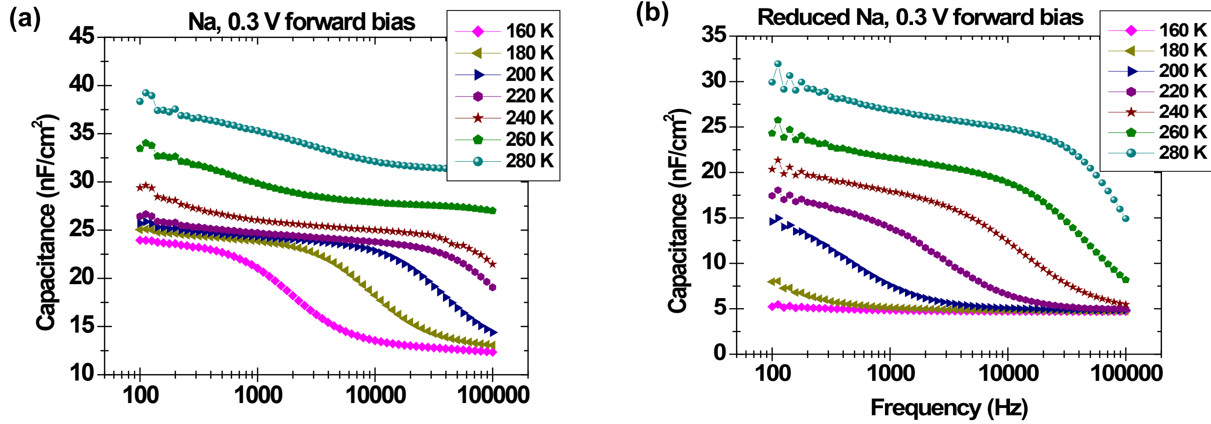

FIG. 49. Admittance spectra for various temperatures under 0.3 volt forward bias for (a) the CIGS sample from deposition A with normal Na levels, and (b) the companion sample with reduced Na. The step in admittance is now present in both samples.

samples spectra looked the same, and the magnitude of the step in the Na sample spectra changed under bias in the manner expected for a bulk defect. The surprise came when the admittance spectra were obtained under forward bias as shown in Figs. 49(a) and (b). The sample with normal Na again changed in the manner expected; however, the reduced Na sample then showed a clear activated step between 180 K and 300 K, with an activation energy of 380 meV.

Next, as shown in Figs. 50(a) and (b), we varied the forward bias while keeping the temperature constant. Here one obtains important insight into the nature of the capacitance step in the low Na sample; namely, that it clearly indicates the presence of large density of states near

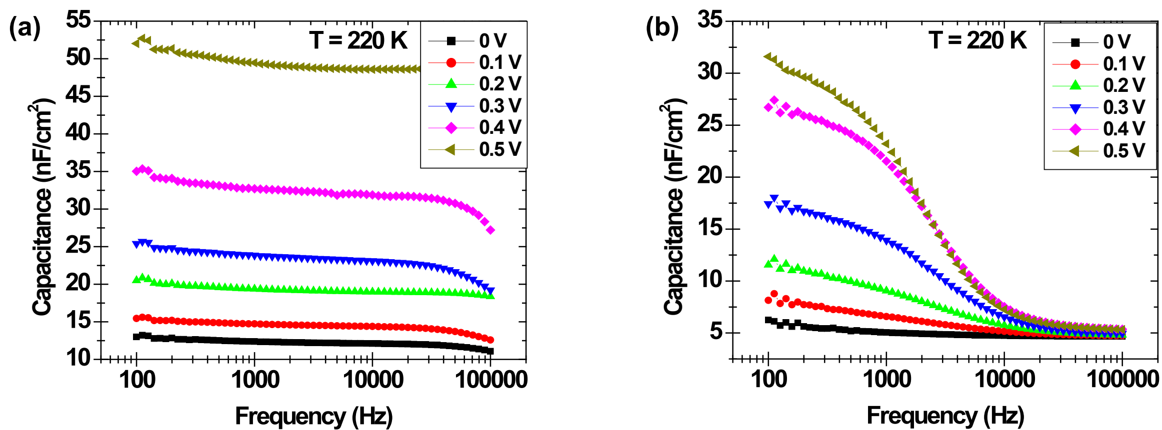

FIG. 50. Admittance spectra at 220K for various values of applied voltage for (a) the normal Na level and (b) the reduced Na sample. Whereas in the former case the appearance of the capacitive step behaves in a manner consistent for a bulk defect, in the latter case its appearance only under forward bias and the limit in the capacitance magnitude as the forward bias is increased are both characteristic responses of a significant interface state.

the interface for the reduced Na samples compared to the sample with normal levels of Na. Specifically, the capacitance of the Na sample increases without any apparent bound as the forward bias is increased whereas, for the reduced Na sample, one appears to reach a limit near 35 nF/cm^2. This limit is indicative of a defect near the barrier interface that becomes more and more charged with increasing forward bias, thus limiting the collapse of the depletion region under forward bias. The fact that the step only appears under a limited range of bias also indicates that this defect is located in the interface.

6.5.2. ORIGIN OF LOWER VOLTAGES IN CIGS CELLS WITHOUT SODIUM

The differing behavior under forward bias is by far the most profound difference between the Na and reduced Na samples, and so seems the strongest clue for the differences in performance. Indeed, a sufficient large defect density in close proximity to the CdS/CIGS interface could easily affect the band bending and result in the 130mV observed difference in V_{oc}. Further insight into this comes from a comparison of the DLCP and CV profiles for the sample without Na from deposition B, as shown in Fig. 51(a) for the measurement at 10kHz and 310K. Because the CV profile is so much higher than the highest temperature DLCP profiles as displayed in Fig. 46(d), this indicates that the difference cannot simply be attributed to deep defects in the bulk region of the CIGS absorber. (In contrast, the DLCP and CV profiles are nearly identical in many cases at higher temperatures for CIGS samples with standard levels of Na.)

To be able to accurately interpret the types of results shown in Fig. 51(a) we extended our computer modeling capabilities to include the effects from both the usual deep acceptors and also from a much deeper band of midgap defects. We also added the ability to examine a wider range of possible spatial variations. The deduced defect distributions are shown in Fig. 51(b) and these resulted in the very good fits to the profiling data shown by the solid lines in Fig. 51(a). These fits indicate that the substantially larger CV profile value actually arises from a large concentration of defects (roughly 10^{17} cm^{-3}) located within about 700Å of the barrier interface.

Such a large defect density in close proximity to the CdS/CIGS interface could easily result in the 130mV observed reduction in V_{OC} compared to the samples with normal Na levels. Indeed, by integrating Poisson's equation we can estimate the loss in V_{OC} due to charged defects in the vicinity of the barrier interface; specifically,

$$\Delta V_{OC} = \frac{1}{\varepsilon}\int_0^\infty x\rho(x)dx \approx \frac{qN_{\text{int}}d}{\varepsilon} \ , \tag{5}$$

where qN_{int} is the total sheet charge density present near the open circuit voltage condition, and d is the width of its spatial distribution from the barrier interface. The inferred defect distribution from the fits in Fig. 51 is of just the correct magnitude to account for the observed V_{OC} deficit. Simulated DLCP profiles were also been obtained for the standard (with Na) CIGS

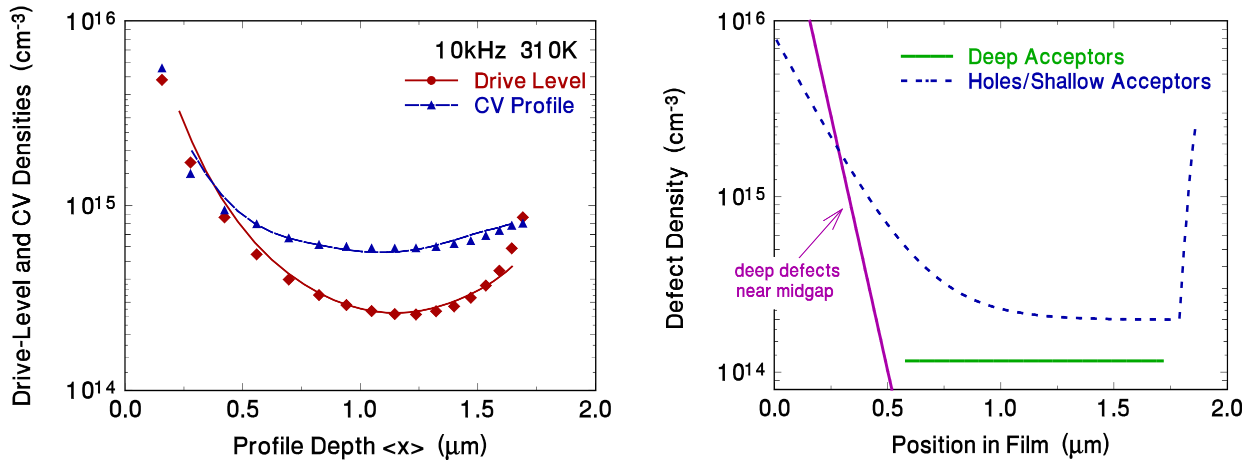

FIG. 51. (a) Simulated fits are shown (solid lines) to the DLCP and CV profiles (symbols) taken at 310K for the Na free sample from deposition B. **(b)** Defect distributions used to simulate the data in 51(a). To account for the large difference between the two types of profiles, we deduced the presence of a large exponentially varying distribution of mid-gap deep defects was located near the barrier interface as shown. The fits also incorporated a low (~10^{14} cm^{-3}) density of bulk deep of acceptors near E_V + 0.35eV indicated by the horizontal dashed line; however, its affect on the profiles was too low to deduce an accurate spatial profile. The distribution of holes/shallow acceptors is shown by the dashed line. We inserted a rapid increase in the shallow acceptor density near 1.8 µm to simulate the effect of the back conducting contact.

profiles of Fig. 46(b). These simulations indicate a significantly larger density of bulk deep defects. They also show some response from defects near the interface; however, that number is lower by nearly two orders of magnitude compared to the sample with reduced Na.

6.5.3. INFLUENCE OF SODIUM ON METASTABLE BEHAVIOR OF CIGS

During our final Subcontract year we studied the effects of light-soaking on the electronic properties of the CIGS samples with and without Na. One of the most dramatic results is that, after even a few minutes of light soaking with white light, a step in the admittance spectra appears in the sample without Na even under reverse bias, as is illustrated in Fig. 52(c). This step has a nearly equal activation energy to that which appeared only under forward bias for the fully annealed sample. Moreover, DLCP measurements confirm that the admittance step that appears after light soaking in the sample without Na does indeed correspond to a bulk deep-acceptor like feature.

We then used these DLCP measurements to examine the details of the creation and annealing kinetics of the deep acceptor and hole carrier densities for sample set B, with and without sodium present. The samples were exposed to white light with one sun intensity at 250K, then the temperature was lowered to measure the free carrier and deep defect densities. In the Na-free sample both the free carrier density and deep defect density were measured at 210 K at different frequencies (200 Hz and 80 kHz) positioned above and below the capacitive step to distinguish the two contributions. For the standard CIGS sample the free carrier density was obtained from 80 kHz profiles at 80 K and the deep defect density from 200 Hz profiles at 160K.

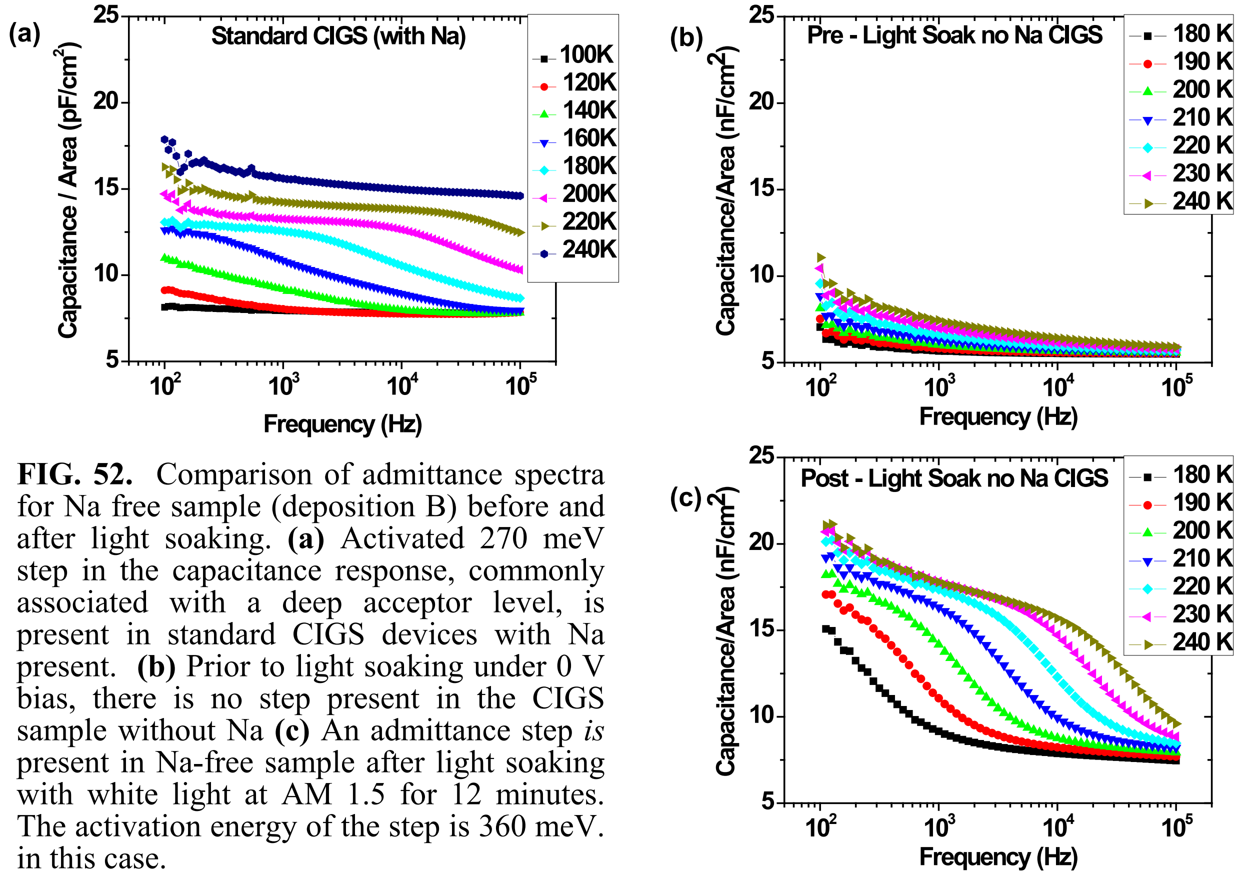

FIG. 52. Comparison of admittance spectra for Na free sample (deposition B) before and after light soaking. **(a)** Activated 270 meV step in the capacitance response, commonly associated with a deep acceptor level, is present in standard CIGS devices with Na present. **(b)** Prior to light soaking under 0 V bias, there is no step present in the CIGS sample without Na **(c)** An admittance step *is* present in Na-free sample after light soaking with white light at AM 1.5 for 12 minutes. The activation energy of the step is 360 meV. in this case.

Figure 53 summarizes the dramatic difference in creation kinetics between the standard CIGS sample and the sample without Na. The deep acceptor and free carrier densities have been normalized to their annealed state values for both samples. Each series started with exposure to light for 1 second and ended with each sample being light soaked for more than 5 hours (or 19683 seconds). The sample containing sodium exhibits the nearly 1:1 relationship between the increases in deep acceptor and hole carrier densities as previously reported by Lee, *et al*, under a variety of light soaking and current injection conditions.[33] Equipment limitations required that we measured the free carrier and deep defect densities at different temperatures for this sample, which we believe accounts for the minor deviation from the 1:1 relationship observed in the sample with Na. Thus these data indicate that for every deep acceptor that is created in the sodium sample, there is a corresponding increase in free holes. In stark contrast to this behavior, the sample without sodium shows only a very modest increase in the free carrier density compared to the much larger increase in the deep acceptor density (the rate of increase of ΔN_A compared to Δp exceeds a factor of 3 in this case).

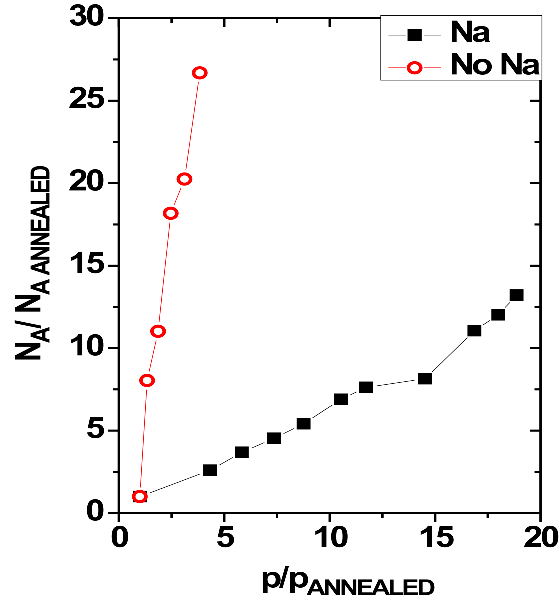

FIG. 53. During light soaking the sample without sodium (deposition B) exhibited a much larger increase in the number of deep acceptors compared to the increase in the free carrier density than the sample containing sodium.

For both cases the deep acceptor density, N_A, and free carrier density, p_A, have been normalized to their values in the annealed state; specifically to $N_A = 5.7\times10^{13}$ cm^{-3} and $p_A = 1.6\times10^{14}$ cm^{-3} for the sample without sodium, and to $N_A = 7.9\times10^{14}$ cm^{-3} and $p_A = 3.0\times10^{14}$ cm^{-3} for the sample with sodium.

In addition, the activation of the deep acceptor versus light-soaking time decreased monotonically from about 275meV to 60meV with a corresponding change in the exponential prefactor that follows a Meyer-Neldel rule behavior. However, the activation energy and prefactor for the deep acceptor in the sample without sodium remained constant within experimental error. This might be taken as evidence that the nature of the deep defects in the samples with and without Na was fundamentally different. However, we doubt this is the case since the points for the Na-free sample shown in Fig. 54 lie very close to the same trend line as the sample containing Na. Moreover, the annealing kinetics of the light-induced increase in deep acceptors is exactly the same for both samples as shown in Fig. 55.

These annealing kinetics were investigated using an isochronal annealing sequence. The samples were held at each anneal temperature for 10 minutes, then the temperature was lowered and the free carrier and deep acceptor densities were measured as described above. Although the magnitudes of the densities are different by an order of magnitude (note the different scales on either side of the graph) the relative annealing behavior is absolutely identical. The identical annealing behavior indicates an identical atomic origin for the metastable behavior in both the standard and Na-free CIGS materials in spite of their different creation kinetics.

The very different behaviors indicated in the creation kinetics (Fig. 53) might suggest that a very different defect complex must be responsible for the metastable behavior in the 2 types of samples. However, it is generally agreed that the creation kinetics of the light-induced effect depends on the minority carrier concentration which, in turn, depends on the electron recombination rate. Because that recombination rate also depends directly on the hole

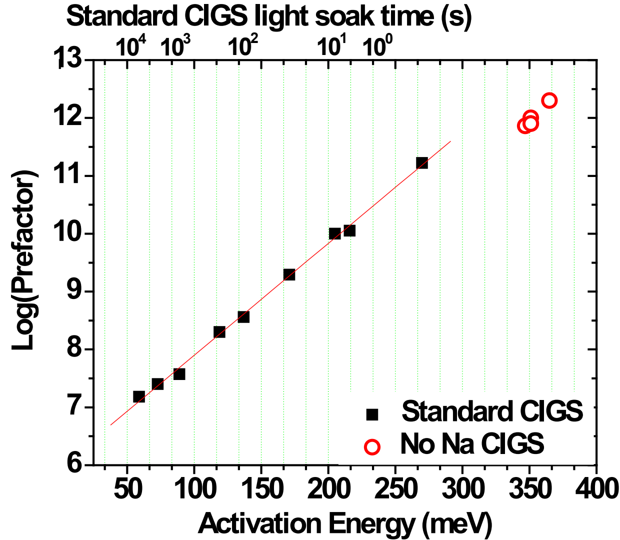

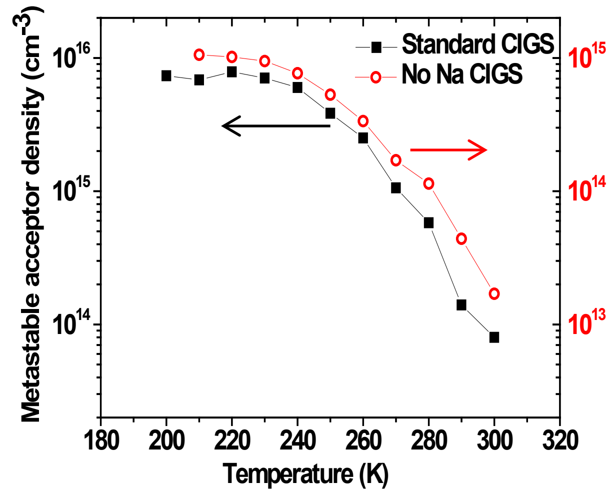

FIG. 54. For the sample with Na, the activation energy of the deep acceptor varies with light soaking in a manner that is consistent with the Meyer-Neldel rule. In contrast, the deep acceptor in the sample without Na (red circles) exhibits the same activation energy and prefactor for all of its metastable states.

FIG. 55. For the companion samples with or without Na, the metastable deep acceptor densities annealed at the exactly the same rate states for each pair of samples, in spite of the differences in absolute magnitude, the different relative increases for the free hole densities displayed in Fig. 53, and the different behavior of the activation and prefactor shown in Fig. 54

concentration, which increases very differently in the two types of samples, this could easily account for any differences in *creation kinetics*. In contrast, the *annealing kinetics* for the two types of samples is nearly identical which suggests that the center responsible for the metastable changes must actually be the same for both types of samples.

The very different way in how the activation energy changes with light soaking in the samples containing Na, but not in the sample without Na (Fig. 54) is also striking and is as yet unexplained. It may suggest the light induced migration of Na ions such that they reside closer to the defect site after light soaking in the former case, thus decreasing the thermal emission energy through a Coulomb repulsion mechanism. Alternate candidate defect models that might be able to account for these metastable behaviors observed in CIGS with and without sodium are still under investigation.

7.0 SUMMARY AND CONCLUSIONS

During the period of our NREL Subcontract period we focused on the three primary areas of study. First, we have continued our work to characterize the electronic properties of nc-Si:H materials obtained from United Solar. Second, we carried out extensive studies on the a-Si,Ge:H alloys deposited using a hot-wire CVD process that was developed at NREL. In particular, we studied the detailed effects of oxygen on the electronic properties of these materials. Finally, we

carried out measurements to characterize the electronic properties of $Cu(In,Ga)Se_2$ (CIGS) films and relate them to the cell performance parameters.

In the first area, the study of nc-Si:H materials, we focused most of our measurements on set of sample devices which were actual working n-i-p solar cell devices. These were all deposited on specular stainless-steel under four different types of hydrogen profiling, and each deposition contained samples with widely varying crystalline fractions. Our results suggest that the degree of crystallinity in these nc-Si:H samples, rather than the hydrogen profiling function itself, was the strongest factor determining the defect response in our junction capacitance measurements. We also found that the samples that contained a higher fraction of amorphous component, as determined from Raman spectroscopy, appeared to exhibit a slight *decrease* after light soaking in the defect response as shown by DLCP measurements. On the other hand, the samples with estimated crystalline fractions above 60vol.% exhibited quite a pronounced increase of deep defects after light soaking. We now tend to believe, however, that light-induced deep defect creation actually occurs in all cases but that the time-scale of the defect response is too slow to be visible in admittance or DLCP measurements for the more amorphous samples.

This minority carrier collection fraction determined by a comparison of the transient photo-capacitance and photocurrent (TPC and TPI) appeared to be reasonably well correlated to the device performance. For the sample with the highest amorphous fraction, the TPC measurements also indicated a photon energy regime centered near 1.4eV where the hole collection fraction actually exceeded the electron collection. We believe that this indicates an optical transition in the amorphous phase regions from the valence band into an empty defect level such that the electron remains deep trapped for the 1s timeframe of our measurement time window.

Regardless of the crystalline fraction, all of the sample devices exhibited a decrease in performance after light soaking with 610nm filtered ELH light. Our TPC and TPI analysis indicated a large decrease in the minority carrier collection after prolonged light exposure. To account for this behavior we put forward a tentative model that proposes a light-induced increase in an energetic barrier between the crystalline and amorphous components of these materials as perhaps a more important factor in limiting the device performance of such mixed phase materials than the increase in the defect density itself. This would account for the marked reduction in minority carrier collection that we have also observed in these materials.

The second area of study involves sets of HWCVD a-Si,Ge:H alloys deposited at NREL by Yueqin Xu. We initially determined that such samples exhibited some of the narrowest bandtails (as low as 43meV) for a-Si,Ge:H alloys deposited at 2 to 3Å/s rates. Initially it was believed that higher oxygen levels in these materials caused a significant decrease in the electronic quality.

This motivated us to examine a series of HWCVD a-Si,Ge:H samples in which controlled levels of oxygen impurities were introduced, ranging from below 10^{19}cm^{-3} to roughly 5×10^{20}cm^{-3}. This led to the discovery that the oxygen was responsible for a distinct deep defect, with an optical transition lying roughly 1.3 to 1.4 eV above the valence band, but with only a very modest increase in Urbach energy. Indeed, our TPC and TPI studies indicated a very high degree of hole collection for these samples. Moreover, unlike all the previous a-Si,Ge:H alloys we have studied, this collection fraction did not decrease after prolonged light-soaking.

The oxygen related defect transition was easily observable at oxygen levels at or below 10^{20} cm^{-3}, and in samples containing Ge fractions of both 15at.% and 30at.%. Moreover, because the electrons excited into this defect remain trapped for roughly 0.5s at temperatures up to 370K, this strongly implies that there must exist a large barrier to their subsequent thermal emission into the conduction band. We hypothesized that the observed oxygen impurity related defect state may be associated with a positively charged oxygen donor level, possibly the previously suggested three fold coordinated oxygen center (O_3^+).

This oxygen related center also exhibited very usual electron thermal emission behavior after the electrons were optically inserted into it from the valence; namely, a two-step thermal emission process in which the first electron was released in a thermally activated manner, and the second was released in a temperature independent manner with a characteristic time constant of 2.2 seconds. This unusual behavior was only observed for higher intensities of light tuned to the defect transition. It has not yet been satisfactorily explained. However, we are considering the idea that the higher intensity light leads to the insertion of two electrons into the defect and, after the thermal emission of the first electron, a long delay occurs while the configurational degrees of freedom are explored, before the second electron ultimately comes out by some sort of tunneling process. We also are considering microscopic models where an oxygen germanium complex may be responsible for the appearance of this defect.

In our third area of study, we applied our junction capacitance methods to study CIGS thin film solar cells in hopes of identifying some of the reasons for higher performance in laboratory cells *vs*. those produce in a commercial process. We illustrated that, by extending our drive-level capacitance profiles slightly into forward bias, we could examine the region as close as 0.2 microns from the barrier junction. This region is likely to be more closely correlated with device performance. We then examined a set of NREL CIGS devices of varying efficiencies (14.4% to 17.2%) and, indeed, found a good correlation between performance and the DLCP defect density in the region closer to the junction interface while, at the same time, seeing essentially no correlation with the defect density farther into the absorber. The good correlation with defect density close to the junction was not present for the 3 highest voltage devices from one

deposition. We believe this can be explained by the fact that these samples exhibited a distinctly different SIMS compositional profile than the those from the other two depositions.

Next, we tried to address the effects of the compositional profiling of the In/Ga ratio to improve CIGS device performance. Samples with four different types of profiling were fabricated at NREL (constant, two types of monotonically increasing Ga fractions away from the junction, plus one example of the v-shaped profiling that has been used to achieve the best CIGS cell efficiencies). We examined these devices using DLCP, TPC and TPI. The most revealing results were obtained from the comparison of TPC and TPI in the photon energy regime above the bandgap. Whereas the devices with a constant Ga fraction exhibited nearly constant and uniform TPI/TPC ratios up to photon energies of 2eV, the profiled samples exhibited an enhanced TPI/TPC ratio for photon energies near 1.2eV indicating an enhanced minority carrier collection in this regime. This supports the idea that the compositional grading increases the collection of electrons generated at longer wavelengths in the absorber region beyond the edge of the depletion region. In addition, the sample devices with the v-shaped profile exhibited TPC spectra with a complex photon energy and temperature dependence. The interpretation of these spectra for those v-shaped profiled samples is still under investigation.

Finally, we also carried out measurements to address the beneficial role of sodium incorporation in CIGS devices. Our admittance and DLCP measurements indicated an increased free carrier density with the addition of Na along with the presence of a bulk defect in the CIGS absorber that captured and emitted free carriers in a thermally activated manner (the so-called "deep acceptor"). That is, the sample devices without Na exhibited a substantially lower free carrier density and the lack of the deep acceptor feature. However, neither of these differences could account for the >40% increase in efficiency with the addition of Na. The sub-band-gap TPC spectra showed a broader defect band and a steeper Urbach energy with the addition of Na which implies an increase in the carrier mobilities, but this again was not expected to lead to the observed 130mV difference in V_{OC} between the samples with and without Na.

However, under forward bias our admittance measurements revealed the existence of a large defect density at the CdS/CIGS heterojunction for the lower Na sample. Moreover, by comparing the DLCP and CV profiles for the samples with and without sodium there appeared to be substantially higher values for the latter that did not simply indicate the presence of a deep bulk defect. Instead, through detailed numerical modeling, we were able to demonstrate that the difference in DLCP *vs.* CV profiles could be reproduced by introducing a large density of defects near the barrier junction (roughly 10^{17} cm^{-3}) lying close to mid-gap, and exponentially decreasing with distance away from the junction. Such a distribution of deep defects near the barrier interface readily explains the loss in V_{OC} in the sample with reduced Na. Thus, it appears

that it is the passivation of these interfacial defects that primarily accounts for the beneficial effects of Na in increasing the performance of the CIGS solar cells fabricated at IEC.

Our final set of measurements to investigate the effects of Na on CIGS involved the comparison of the metastable properties on the matched sets of samples following light exposure. Here a number of very interesting, but not well understood, observations were made: (1) Following light exposure the samples without sodium developed a significant deep acceptor density throughout the bulk region of the absorber that had been absent in the fully annealed samples; (2) Whereas in the standard Na-level CIGS samples exhibit a nearly 1-to-1 metastable increase in both the free carrier density and deep acceptor density with increasing light exposure, the samples without Na show a substantial increase in deep acceptors with a much smaller relative increase in free carriers; and (3) The activation energy revealed by admittance for the deep acceptors varies with light soaking (from 275meV to roughly 60meV) for the standard sample with variations in the thermal emission prefactor obeying a Meyer-Neldel rule while, for the Na-free samples, this activation energy and prefactor remain nearly constant (close to 350meV and 10^{12} s^{-1}). While the last observation might indicate that the deep acceptor response in the two types of samples are fundamentally different, the annealing behavior with increasing temperature appears identical.

Thus, we believe the deep acceptor in the two types of samples has the same origin. Since the 1-to-1 increase in deep acceptor and free carrier density has been taken as strong evidence for a model of metastable behavior in CIGS materials involving the (V_{Se}-V_{Cu}) complex as proposed by Lany and Zunger.[34], the lack of such a 1-to-1 correspondence in the samples without Na may have important consequences. Rather, it appears that, in samples without Na, light soaking results in an energy shift of the defect in the gap without any change in its electronic occupation (in the neutral bulk region).

We do not yet have a plausible microscopic model that accounts for all of our observations. It has been argued [35] that the presence of Na in CIGS inhibits the formation of In_{Cu} antisite defects, and those defects are indeed likely to reduce free carrier densities through the formation of In_{Cu}-V_{Cu} complexes. This may then imply a predominance of a different type of defect complex involving the Se vacancies and altering the details of their metastable behavior in the manner we have observed. Or it may indicate that an entirely different type of defect, such as the In_{Cu} antisites, are at the root of the observed metastable properties of CIGS materials. We are currently preparing a manuscript which will explore some of these possibilities in more detail [Publ. 13].

8.0 SUBCONTRACT SUPPORTED PUBLICATIONS

1. P.G. Hugger, S. Datta, P.T. Erslev, Guozhen Yue, Gautam Ganguly, Baojie Yan, Jeffrey Yang, Subhendu Guha, and J.D. Cohen, “Electronic characterization and light-induced degradation in nc-Si:H solar cells”, Mat. Res. Soc. Symp. Proc. **910**, 21 (2006).

2. Shouvik Datta, J. David Cohen, Steve Golledge, Yueqin Xu, A. H. Mahan, James R. Doyle and Howard M. Branz, “The effect of oxygen contamination on the electronic properties of hot-wire cvd amorphous silicon germanium alloys”, Mat. Res. Soc. Symp. Proc. **910**, 47 (2006).

3. Shouvik Datta, Yueqin Xu, A. H. Mahan, Howard M. Branz, and J. David Cohen, “Superior structural and electronic properties for amorphous silicon-germanium alloys deposited by a low temperature hot wire chemical vapor deposition process”, J. Non-Cryst. Solids **352**, 1250 (2006).

4. Shouvik Datta, J. David Cohen, Yueqin Xu, A.H. Mahan, and Howard M. Branz, “Dependence of the electronic properties of hot-wire CVD amorphous silicon-germanium alloys on oxygen impurity levels”, Mat. Res. Soc. Symp. Proc. Vol **989**, 55 (2007).

5. Peter T. Erslev, Adam F. Halverson, J. David Cohen, and William N. Shafarman, “Study of the electronic properties of matched Na-containing and Na-free CIGS samples using junction capacitance methods”, Mat. Res. Soc. Symp. Proc. Vol **1012,** 445 (2007).

6. J. David Cohen, Shouvik Datta, Kimon Palinginis, A. H. Mahan , Eugene Iwaniczko, Yueqin Xu, and Howard M. Branz, “Defect analysis of thin film Si-based alloys deposited by hot-wire CVD using junction capacitance methods”, Thin Solid Films **516**, 663 (2008).

7. P.G. Hugger, J.D. Cohen, B. Yan, J. Yang, and S. Guha, “Properties of light-induced degradation and the electronic properties of nanocrystalline silicon solar cells grown under functionally graded hydrogen dilutions”, J. Non-Cryst. Solids **354**, 2460 (2008).

8. Shouvik Datta, J. David Cohen, Yueqin Xu, A.H. Mahan, and Howard M. Branz, “Junction capacitance study of an oxygen impurity defect exhibiting configuration relaxation in amorphous silicon-germanium alloys deposited by hot-wire CVD”, J. Non-Cryst. Solids **354**, 2126 (2008).

9. P.G. Hugger, J.D. Cohen, B. Yan, G. Yue, X. Xu, J. Yang, and S. Guha, “Electronic properties of nanocrystalline silicon deposited with different crystallite fractions and growth rates”, Mat. Res. Soc. Symp. Proc. **1066**, 149 (2008).

10. Shouvik Datta, J. David Cohen, Yueqin Xu, and Howard M. Branz, “Two-step capacitance transients from an oxygen impurity defect”, Mat. Res. Soc. Symp. Proc. **1066**, 259 (2008).

11. Peter T. Erslev, JinWoo Lee, J. David Cohen, and William N. Shafarman, “The influence of Na on metastable defect kinetics in CIGS materials”, Thin Solid Films **517**, 2277 (2009)..

12. JinWoo Lee, Jeroen K.J. van Duren, Alex Pudov, Miguel A. Contreras, and J. David Cohen, “Effects of Ga compositional variations on CIGS solar cell device performance”, Mat . Res. Soc. Symp. Proc. **1165**, M01-09 (2009).

13. Peter T. Erslev, JinWoo Lee, J. David Cohen, and William N. Shafarman, “Comparison of CIGS films with and without sodium: Insights into the fundamental properties of deep defects”, in preparation.

9.0 REFERENCES

1. K. Wang, D. Han, D.L. Williamson, B. Huie, J.R. Weinberg-Wolf, b. Yan, J. Yang, and S. Guha, Mater. Res. Soc. Symp. Proc. Vol. **862**, 117 (2005).
2. E. Bustarret, M.A. Hachicha, and M. Brunel, Appl. Phys. Lett. 52, 1675 (1988).
3. J.D. Cohen, NREL Report SR-520-32535 (2002).
4. C. Lei, C.M. Li, A. Rockett and I.M. Robertson, J. Appl. Phys. **101**, 024909 (2007).
5. V. Lyahovitskaya, Y. Feldman, K. Gartsman, H. Cohen, C. Cytermann, and David Cahen, J. Appl. Phys., **91**, 4205 (2002).
6. A. Rockett, *Thin Solid Films* **480-1,** 2 (2005).
7. D. Rudmann, D. Bremaud, H. Zogg and A. N. Tiwari, J. Appl. Phys. **97**, 084903 (2005).
8. D.V. Lang, J.D.Cohen, and J.P. Harbison, Phys. Rev. B**25**, 5285 (1982).
9. C.E. Michelson, A.V. Gelatos, and J.D. Cohen, Appl. Phys. Lett. **47**, 412 (1985).
10. K.K. Mahavadi, K. Zellama, J.D. Cohen, and J.P. Harbison, Phys. Rev. B**35**, 7776 (1987).
11. T. Unold, J. Hautala, and J.D. Cohen, Phys. Rev. B50, 16985 (1994).
12. J.T. Heath, J.D. Cohen, and W.N. Shafarman, J. Appl. Phys. **95**, 1000 (2004).
13. J.D. Cohen and A.V. Gelatos, in *Advances in Disordered Semiconductors Vol I: Amorphous Silicon and Related Materials*, ed. by H. Fritzsche (World Scientific, Singapore, 1988), pp. 475-512.
14. J. David Cohen, Thomas Unold, A.V. Gelatos, and C.M. Fortmann, J. Non-Cryst. Solids **141**, 142 (1992).
15. T. Unold, J.D. Cohen, and C.M. Fortmann, Mat. Res. Soc. Symp. Proc. **258**, 499 (1992).
16. A.V. Gelatos, K.K. Mahavadi, and J.D. Cohen, Appl. Phys. Lett. **53**, 403 (1988).
17. A.F. Halverson, J.J. Gutierrez, J.D. Cohen, B. Yan, J. Yang, and S. Guha, Appl. Phys. Lett. 88, 071920 (2006).
18. P.G. Hugger, S. Datta, P.T. Erslev, G. Yue, G. Ganguly, B. Yan J. Yang, S. Guha, and J.D. Cohen, Mat. Res. Soc. Symp. Proc. **910**, 21 (2006).
19. B. Yan, G. Yue, J.M. Owens, J. Yang, and S. Guha, Appl. Phys. Lett. **85**, 1925 (2004).
20. T. Unold, J. Hautala, and J.D. Cohen, Phys. Rev. B**50**, 16985 (1994).
21. Y. Lubianiker, J.D. Cohen, H.-C. Jin, and J.R. Abelson, Phys. Rev. B**60**, 4434 (1999).
22. A.F. Halverson, J.J. Gutierrez, J.D. Cohen, B. Yan, J. Yang, and S. Guha,, Mat. Res. Soc. Symp. Proc.**862**, 481 (2005).
23. A.H. Mahan, Y. Xu, L.M. Gedvilas, R.C. Reedy, H.M. Branz, D.L. Williamson, S. Datta, J.D. Cohen, and B. Yan, Proc. 31st IEEE PV Specialists Conference-2005 (Buena Vista)
24. S. Datta, J. D. Cohen, Y.Xu, and A. H. Mahan, Mat. Res. Soc. Symp. Proc. **862**, A7.2 (2005).

25. C. E. Michelson and J.D. Cohen, Phys. Rev. B**41**, 1529 (1990).

26. Chih-Chiang Chen, Fan Zhong, J.D. Cohen, Jeffrey C. Yang, and Subhendu Guha, Phys. Rev. B**57**, R4210 (1998).

27. R. A. Street and N. F. Mott, Phys. Rev. Lett. **35**, 1293 (1975).

28. David Adler, Solar cells. **9**, 133 (1983).

29. Tatsuo Shimizu, Minoru Matsumoto, Masahiro Yoshita, Masahiko Iwami, Akiharu Morimoto, and Minoru Kumeda, J. Non-Cryst. Solids. **137&138**, 391 (1991).

30. H. Fritzsche, J. Non-Cryst. Solids. **190**, 180 (1995).

31. I.L. Repins, B.J. Stanbery, D.L. Young, S.S. Li, W.K. Metzger, C.L. Perkins, W.N. Shafarman, M.E. Beck, L.Chen, V.K. Kapur, D. Tarrant, M.D. Gonzalez, D.G. Jensen, T.J. Anderson, X. Wang, L.L. Kerr, B. Keyes, S. Asher, A. Delahoy, and B. von Roedern, Prog. Photovolt: Res. Appl. **14**, 25 (2006).

32. S.M. Wasim, C. Rincon, G. Marin, P. Bocaranda, E. Hernandez, I. Bonalde and E. Medina, Phys. Rev. B., **64**, 195101 (2001).

33. J. Lee, J. T. Heath, J. D. Cohen, and W. N. Shafarman, Mater. Res. Soc. Symp. Proc. **865,** 373 (2005).

34. S. Lany and A. Zunger, J. Appl. Phys. **100**, 113725 (2006).

35. Su-Huai Wei, S. B. Zhang, and Alex Zunger, J. Appl. Phys. **85**, 7214 (1999).

REPORT DOCUMENTATION PAGE	*Form Approved* *OMB No. 0704-0188*

The public reporting burden for this collection of information is estimated to average 1 hour per response, including the time for reviewing instructions, searching existing data sources, gathering and maintaining the data needed, and completing and reviewing the collection of information. Send comments regarding this burden estimate or any other aspect of this collection of information, including suggestions for reducing the burden, to Department of Defense, Executive Services and Communications Directorate (0704-0188). Respondents should be aware that notwithstanding any other provision of law, no person shall be subject to any penalty for failing to comply with a collection of information if it does not display a currently valid OMB control number.

PLEASE DO NOT RETURN YOUR FORM TO THE ABOVE ORGANIZATION.

1. REPORT DATE *(DD-MM-YYYY)*	2. REPORT TYPE	3. DATES COVERED *(From - To)*
December 2009	Subcontractor Report	4/28/2005 to 9/15/2008

4. TITLE AND SUBTITLE
Innovative Characterization of Amorphous and Thin-Film Silicon for Improved Module Performance: 28 April 2005 - 15 September 2008

5a. CONTRACT NUMBER
DE-AC36-08-GO28308

5b. GRANT NUMBER

5c. PROGRAM ELEMENT NUMBER

6. AUTHOR(S)
J.D. Cohen

5d. PROJECT NUMBER
NREL/SR-520-47195

5e. TASK NUMBER
PVB75201

5f. WORK UNIT NUMBER

7. PERFORMING ORGANIZATION NAME(S) AND ADDRESS(ES)
Dept. of Physics and Materials Science Institute
University of Oregon
Eugene, Oregon

8. PERFORMING ORGANIZATION REPORT NUMBER
ZXL-5-44205-11

9. SPONSORING/MONITORING AGENCY NAME(S) AND ADDRESS(ES)
National Renewable Energy Laboratory
1617 Cole Blvd.
Golden, CO 80401-3393

10. SPONSOR/MONITOR'S ACRONYM(S)
NREL

11. SPONSORING/MONITORING AGENCY REPORT NUMBER
NREL/SR-520-47195

12. DISTRIBUTION AVAILABILITY STATEMENT
National Technical Information Service
U.S. Department of Commerce
5285 Port Royal Road
Springfield, VA 22161

13. SUPPLEMENTARY NOTES
NREL Technical Monitor: Bolko von Roedern

14. ABSTRACT *(Maximum 200 Words)*
The report focuses on the three primary areas of study. First, we have continued our work to characterize the electronic properties of nc Si:H materials obtained from United Solar. Second, we carried out extensive studies on the a Si,Ge:H alloys deposited using a hot-wire CVD process that was developed at NREL. In particular, we studied the detailed effects of oxygen on the electronic properties of these materials. Finally, we carried out measurements to characterize the electronic properties of Cu(In,Ga)Se2 (CIGS) films and relate them to the cell performance parameters.

15. SUBJECT TERMS
PV; characterization; amorphous silicon; thin film; module performance; hot-wire chemical vapor deposition; electronic properties; CIGS; cell performance

16. SECURITY CLASSIFICATION OF:			17. LIMITATION OF ABSTRACT	18. NUMBER OF PAGES	19a. NAME OF RESPONSIBLE PERSON
a. REPORT	b. ABSTRACT	c. THIS PAGE			
Unclassified	Unclassified	Unclassified	UL		19b. TELEPHONE NUMBER (*Include area code*)

Standard Form 298 (Rev. 8/98)
Prescribed by ANSI Std. Z39.18

F1146-E(10/2008)